DEVELOPING MODELS OF AEROSOL REPRESENTATION TO INVESTIGATE COMPOSITION, EVOLUTION, OPTICAL PROPERTIES, AND CCN SPECTRA USING MEASUREMENTS OF SIZE-RESOLVED HYGROSCOPICITY

A Dissertation

by

ROBERTO GASPARINI

Submitted to the Office of Graduate Studies of
Texas A&M University
in partial fulfillment of the requirements for the degree of

DOCTOR OF PHILOSOPHY

May 2005

Major Subject: Atmospheric Sciences

DEVELOPING MODELS OF AEROSOL REPRESENTATION TO INVESTIGATE COMPOSITION, EVOLUTION, OPTICAL PROPERTIES, AND CCN SPECTRA USING MEASUREMENTS OF SIZE-RESOLVED HYGROSCOPICITY

A Dissertation

by

ROBERTO GASPARINI

Submitted to Texas A&M University
in partial fulfillment of the requirements
for the degree of

DOCTOR OF PHILOSOPHY

Approved as to style and content by:

Donald R. Collins (Chair of Committee)	Robert A. Duce (Member)
William H. Marlow (Member)	Renyi Zhang (Member)
Richard E. Orville (Head of Department)	

May 2005

Major Subject: Atmospheric Sciences

ABSTRACT

Developing Models of Aerosol Representation to Investigate
Composition, Evolution, Optical Properties, and CCN Spectra
Using Measurements of Size-Resolved Hygroscopicity. (May 2005)
Roberto Gasparini, B.S., Texas A&M University;
M.S., Texas A&M University
Chair of Advisory Committee: Dr. Donald R. Collins

A Differential Mobility Analyzer/Tandem Differential Mobility Analyzer (DMA/TDMA) was used to measure size distributions, hygroscopicity, and volatility during the May 2003 Aerosol Intensive Operational Period at the Central Facility of the Atmospheric Radiation Measurement Southern Great Plains site. Hygroscopic growth factor distributions for particles at eight dry diameters ranging from 0.012 μm to 0.600 μm were measured. These measurements, along with backtrajectory clustering, were used to infer aerosol composition and evolution. The hygroscopic growth of the smallest and largest particles analyzed was typically less than that of particles with dry diameters of about 0.100 μm. Condensation of secondary organic aerosol on nucleation mode particles may be responsible for the minimal growth observed at the smallest sizes. Growth factor distributions of the largest particles typically contained a non-hygroscopic mode believed to be composed of dust. A model was developed to characterize the hygroscopic properties of particles within a size distribution mode through analysis of

the fixed-size hygroscopic growth measurements. This model was used to examine three cases in which the sampled aerosol evolved over a period of hours or days.

Additionally, size and hygroscopicity information were combined to model the aerosol as a population of multi-component particles. With this model, the aerosol hygroscopic growth factor f(RH), relating the submicron scattering at high RH to that at low RH, is predicted. The f(RH) values predicted when the hygroscopic fraction of the aerosol is assumed to be metastable agree better with measurements than do those predicted under the assumption of crystalline aerosol. Agreement decreases at RH greater than 65%. This multi-component aerosol model is used to derive cloud condensation nuclei (CCN) spectra for comparison with spectra measured directly with two Desert Research Institute (DRI) CCN spectrometers. Among the 1490 pairs of DMA/TDMA-predicted and DRI-measured CCN concentrations at various critical supersaturations from 0.02-1.05%, the sample number-weighted mean R^2 value is 0.74. CCN concentrations are slightly overpredicted at both the lowest (0.02-0.04%) and highest (0.80-1.05%) supersaturations measured. Overall, this multi-component aerosol model based on size distributions and size-resolved hygroscopicity yields reasonable predictions of the humidity-dependent optical properties and CCN spectra of the aerosol.

DEDICATION

To all those who have had a hand

in the development of this work

and in the development of the author

ACKNOWLEDGMENTS

So many people deserve acknowledgment for all that they have done for me. First off, God created me and this Earth, so I certainly owe a tremendous amount to Him. I also thank my family: Mom, Dad, Cristina, Raymond, Tori, Marco, Katrina, Miranda, and Matteo, for providing a moral foundation for me and for their constant love, encouragement, and support. I thank the many school teachers along the way, each of whom took personal interest in my development and growth. During my undergraduate years, great friends like Keith O'Connor and Josh Cernosek helped me grow as a person. I also thank the many professors who have watchfully guided me during my nine years at Texas A&M. My growth as a scientist was really given a boost by Dr. Don Collins, who took me on as a project and selflessly worked with me. In learning an entirely new field in aerosol science, I am grateful for the assistance offered by my committee: Drs. Bob Duce, Bill Marlow, and Renyi Zhang. I also owe a great deal to my colleagues in the Aerosol Research Group, notably Yong Seob Lee, Runjun Li, Josh Santarpia, Chance Spencer, and Jason Tomlinson. Doug Ames, Ed Amrhein, Dan Huckaby, and Kerry Meyer are some of the best friends a person can have, and I love them as I do family. Additionally, numerous non-aerosol colleagues deserve recognition: Casey Anderson, Andy Brown, Dan Jamieson, Jason Jordan, Dave Mitnick, Steve Phillips, Scott Steiger, and Tim Thomas, to name a few.

I especially want to acknowledge my loving, caring, and selfless wife Virginia. Her constant support serves as a daily inspiration for me. I can only hope to be as positive an influence on others as she is on me.

TABLE OF CONTENTS

Page

LIST OF FIGURES

FIGURE Page

FIGURE Page

LIST OF TABLES

1. INTRODUCTION*

Atmospheric aerosols generally consist of multiple compositional components. While the inorganic species are reasonably well characterized and their hygroscopic, optical, and activation properties are well understood [see, e.g., *Seinfeld and Pandis*, 1998], organic species are far more difficult to characterize [see, e.g., *Saxena et al*., 1995; *Kalberer et al*., 2004]. Since a multitude of organic species are involved in aerosol formation and growth processes, modeling these processes accurately poses a significant challenge [*Bian and Bowman*, 2005; *Griffin et al*., 2005]. Beyond the complexities regarding aerosol formation and growth, additional factors such as the geometry of a particle [see, e.g., *Quinn et al*., 2004], its aging time scale [*Riemer et al*., 2004], and its interactions with other aerosol species [see, e.g., *Nozière and Esteve*, 2005] have all been observed to impact the various properties of the aerosol. Given the numerous complications introduced by individual aerosol species and characteristics, it is desirable to develop a simple model that can accurately simulate aerosol properties.

The radiative impact, cloud nucleating properties, and atmospheric lifetime of an aerosol are strongly influenced by its hygroscopicity. The hygroscopic behavior of the

---

This dissertation follows the style and format of *Journal of Geophysical Research-Atmospheres*.

range of inorganic species typically found in atmospheric aerosols has been well characterized [see, e.g., *Orr et al.*, 1958; *Tang*, 1976; *Tang and Munkelwitz*, 1977]. In contrast, there still remains considerable uncertainty regarding the hygroscopic growth of organic particles. The limited data that are available suggest that most pure organic aerosols grow substantially less in response to increased relative humidity (RH) than do most inorganic particles. Other common particle types such as elemental carbon and dust exhibit only limited hygroscopic growth. Measurements of the hygroscopic properties of an ambient aerosol can be coupled with the extensive dataset available describing the expected growth of single and multi-component particles to constrain the composition of the aerosol. Unlike most conventional techniques for characterizing aerosol composition, size-resolved hygroscopic growth measurements are often able to provide insight into the mixing state of the aerosol and into associations between different particle types.

In some of the earliest studies of ambient aerosol hygroscopicity, *McMurry and Stolzenburg* [1989] and *Zhang et al.* [1993] suggested that the size-dependent hygroscopicity they observed was a result of size-dependent aerosol composition. Measurements of size-dependent hygroscopicity have also been used as potential indicators for various atmospheric processes, such as secondary organic aerosol (SOA) formation [*Svenningsson et al.*, 1997], photochemical oxidation [*Swietlicki et al.*, 1999], and cloud processing [*Kerminen*, 1997]. Most previous studies of hygroscopic growth have been based on measurements made at a set of fixed dry diameters. The extrapolation of these measurements to the entire aerosol population is necessary to

reach conclusions regarding aerosol composition and evolution. There are intrinsic difficulties and limitations with the use of measurements at a few sizes to identify the factors responsible for changes occurring within a dynamic size distribution, especially in complex urban aerosols that contain numerous size distribution modes. A more complete understanding of the sources of individual size distribution modes and the processes affecting them could be reached by characterizing the hygroscopic properties of modes rather than those of specific diameters. Mode-resolved aerosol hygroscopicity could then be combined with details of the origin of the aerosol and the atmospheric conditions it experienced during transport to provide insight into its composition and evolution.

Measurements of aerosol volatility also provide insight into aerosol composition. For example, the mass fraction of sulfuric acid in a sample of fine marine aerosols has been determined using volatility measurements [*Orsini et al.*, 1999]. Volatility measurements of size-resolved aerosol have also been analyzed in order to provide insight into both the mixing state and the aging processes of the aerosol [*Philippin et al.*, 2004]. Furthermore, a better understanding of the composition of non-volatile species is attained when measuring their hygroscopic properties [*Johnson et al.*, 2004].

Ultimately, aerosols impact climate directly through extinction of solar radiation [see, e.g., *Charlson et al*., 1992] and indirectly by altering the lifetimes and albedo of clouds [*Twomey*, 1977; *Albrecht*, 1989]. The Intergovernmental Panel on Climate Change (IPCC) summarizes estimates of global annual mean radiative forcing for various major aerosol types. Among the reported best estimates of direct radiative

forcing by distinct anthropogenic aerosol species, values range from a minimum of -0.4 W m^{-2} for sulfates to a maximum of +0.2 W m^{-2} for fossil fuel black carbon [*IPCC*, 2001]. It also reports a range of 0 to -2 W m^{-2} for the annual global mean radiative forcing resulting from the first indirect effect with no best estimate given, and it provides no estimated range for the second indirect effect though it suggests that the sign is negative [*IPCC*, 2001].

Both the size distribution and composition of a particle population affect its optical and activation properties, which ultimately determine its climatological impact. Unfortunately, detailed time- and size-resolved composition measurements spanning the full size range of tropospheric aerosols are challenging to obtain. Indirect methods of inferring composition, such as analyzing hygroscopicity, are therefore valuable in determining the climatic effects of tropospheric aerosols. To determine the precise effect of aerosols on climate, the representation of aerosol composition employed must result in the successful prediction of both its optical and activation properties.

Closure of modeled and measured light scattering has been achieved within 10% for dry monodisperse calibration aerosol [*Anderson et al.*, 1996], within 13% for hydrated monodisperse single-component aerosol [*Kus et al.*, 2004], and within 19% for dry polydisperse ambient marine aerosol [*Quinn et al.*, 1996]. Many closure studies model the aerosol as consisting of a single component, which is a reasonable assumption for laboratory-generated aerosol. Within the atmosphere, however, the aerosol generally consists of multiple components. For cloud condensation nuclei (CCN) closure, only a few successful studies are reported in refereed scientific literature [*Liu et al.*, 1996;

Cantrell et al., 2001; *Roberts et al.*, 2002; *VanReken et al.*, 2003]. Successful closure was achieved during each of these studies when the aerosol was relatively homogeneous and present at low concentration. In some other attempted closure studies, *Bigg* [1986] observed a decreasing degree of closure with increasing CCN concentrations, *Martin et al.* [1994] achieved reasonable closure for a single maritime sample but did not while sampling more polluted air, and *Covert et al*. [1998] were more successful with closure when sampling background marine aerosol than with continental aerosol or aerosol from oceanic regions of elevated biological activity. This paper describes the prediction of both the humidity-dependent optical properties and CCN spectra of an aerosol using a single model that treats the aerosol as a population of multi-component particles whose composition is inferred using size-resolved hygroscopicity measurements.

Various atmospheric aerosol and radiative properties as well as a number of relevant meteorological variables are continuously measured at the Southern Great Plains (SGP) site established by the U.S. Department of Energy's Atmospheric Radiation Measurement (ARM) Program. The continued commitment to the Central Facility of the ARM SGP site just south of the Oklahoma-Kansas border has yielded a long-term dataset that allowed for the development of a four-year climatology on submicron aerosol scattering and absorption [*Sheridan et al.*, 2001] and a quantification of the aerosol indirect effect [*Feingold et al.*, 2003]. Continuous measurements at the ARM SGP site have also captured events that made possible analyses of the optical properties of smoke-dominated haze [*Iziomon and Lohmann*, 2003a], the vertical variation of aerosol extinction and backscattering [*Turner et al.*, 2001, 2002], and the

application of surface measurements to retrieve aerosol optical depth [*Bergin et al.*, 2000].

Aerosol size distributions and size-resolved hygroscopicity were measured at the surface using a Differential Mobility Analyzer/Tandem Differential Mobility Analyzer (DMA/TDMA) in the Guest Instrument Trailer at the Central Facility of the ARM SGP site during the May 2003 Aerosol Intensive Operational Period (IOP). With the exception of a few periods of instrument downtime for maintenance and repair, sampling was conducted continuously from May 04-29. In addition to hygroscopic growth measurements made at fixed RH at eight different dry diameters, occasional measurements of hygroscopicity were made in which the RH was varied from ~30-90%. Measurements of aerosol volatility were also occasionally made by exposing the aerosol to temperatures ranging from ~40-300°C.

Complementary measurements of optical properties were made with the Aerosol Observing System (AOS) at the SGP site. Two Desert Research Institute (DRI) CCN spectrometers were also operated at the SGP site during the Aerosol IOP to measure CCN spectra spanning critical supersaturations from 0.02% to 1.05%. Such a collection of collocated instruments allowed for independent comparisons of various derived and measured aerosol properties.

2. INSTRUMENT DETAILS*

2.1. DMA/TDMA

A schematic of the DMA/TDMA system as configured during the Aerosol IOP is shown in Figure 1. A thorough description of the various components within the DMA/TDMA is provided in the work of *Gasparini et al.* [2004]. Two Aerosol Dynamics, Inc., High Flow Differential Mobility Analyzers (HF-DMAs) [*Stolzenburg et al*., 1998] are used in the DMA/TDMA to maximize particle count rate. When measuring hygroscopic growth, the aerosol is initially dried in Nafion tube #1 and the electric field in the first HF-DMA is held constant in order to select a monodisperse aerosol. The exiting monodisperse aerosol bypasses Nafion tube #2 by way of the heated tube, in which the heater is off, and is then exposed to and equilibrates with an environment in Nafion tube #3 in which the relative humidity is controlled to 85%. Following this exposure to high RH, the aerosol passes through the second HF-DMA, in which the electric field is exponentially ramped up and then back down as prescribed by *Wang and Flagan* [1990]. The resulting size- and hygroscopically-resolved aerosol is counted using a TSI, Inc., 3762 Condensation Particle Counter (CPC). Hygroscopicity is described by the ratio of the diameter of a particle following exposure to high RH, D_p,

---

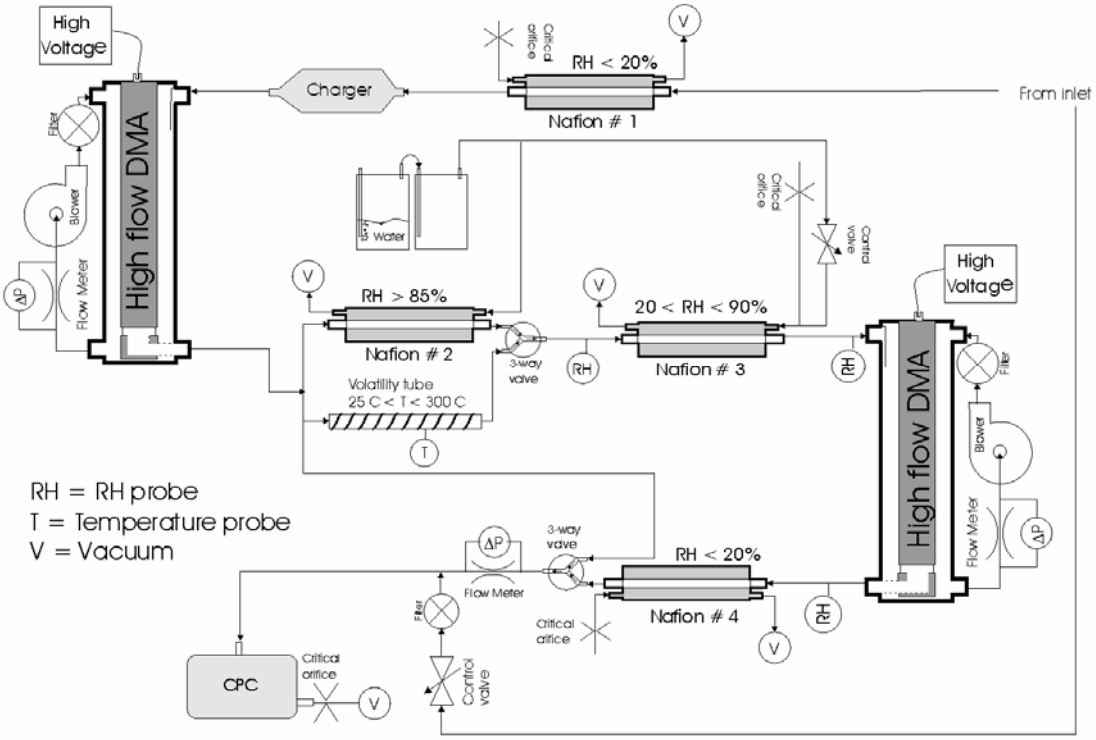

Figure 1. Schematic of the DMA/TDMA as configured at the ARM SGP site during the Aerosol IOP.

to its initial dry diameter, D_p*. This ratio is commonly referred to as the hygroscopic growth factor and is abbreviated G(85) since the higher RH for this study was 85%. In the discussion that follows, dry diameter will always refer to the particle size separated by the first HF-DMA during TDMA measurements.

In addition to measuring hygroscopic growth at a fixed RH, the instrument used during this study is designed to vary the RH to which the dry monodisperse aerosol is exposed over a wide range while hygroscopic growth factor distributions are continuously measured. During these RH scans, the aerosol is exposed to an RH of less than 15% prior to entering the first HF-DMA to ensure that deliquescent particles are crystalline. The dried monodisperse aerosol is then directed through the heated tube, in which the heater is off, exposed to a higher relative humidity in Nafion tube #3, classified by the second HF-DMA in which the voltage is rapidly scanned, and counted by the CPC. This higher relative humidity is decreased gradually from ~90% to ~35% over the course of about 30 minutes. The deliquescence properties of the aerosol are readily determined through examination of the approximately 30 growth factor distributions measured as the RH was decreased. Following the completion of those measurements describing the lower leg of the hygroscopic growth hysteresis loop, the dried monodisperse aerosol selected by the first HF-DMA is exposed to an RH of over 90% in Nafion tube #2 to ensure that all deliquescent particles are hydrated. The humidified aerosol stream is then exposed to an intermediate relative humidity in Nafion tube #3, size-selected by the second HF-DMA, and counted by the CPC. The intermediate relative humidity to which the aerosol is exposed is increased gradually

from ~30% to ~90% over a span of about 30 minutes. The growth factors measured in this way describe the upper or metastable leg of the hygroscopic growth hysteresis loop. The RH at which any discontinuity exists in the relationship between the measured growth factor and RH represents the aerosol crystallization RH.

To characterize size-resolved aerosol volatility, the temperature in the heated tube shown in Figure 1 is first raised to just over 300°C. Over the next 45 minutes, the heated tube is allowed to cool to ambient temperature. Following exposure to high temperature, the non-volatile fraction of the initially monodisperse aerosol is humidified to 85% RH, which permits identification of the hygroscopic and non-hygroscopic fractions so that the volatility behavior of the two populations can be examined. Size distributions of the heated and humidified aerosol are recorded approximately every minute. The resulting temperature resolution over the range in which significant changes in particle size are typically observed is approximately 10°C. The temperature at which most of the hygroscopic particles volatilize can be used to infer the dominant inorganic species present.

Figure 2 contains a time series of the total submicron aerosol number concentration as computed by integrating the size distributions measured with the DMA/TDMA and as measured by a NOAA CMDL TSI CPC. The concentrations computed with the DMA/TDMA data match well with those measured directly. Additionally, the time resolution of the DMA/TDMA is sufficient to capture most abrupt changes in aerosol concentration.

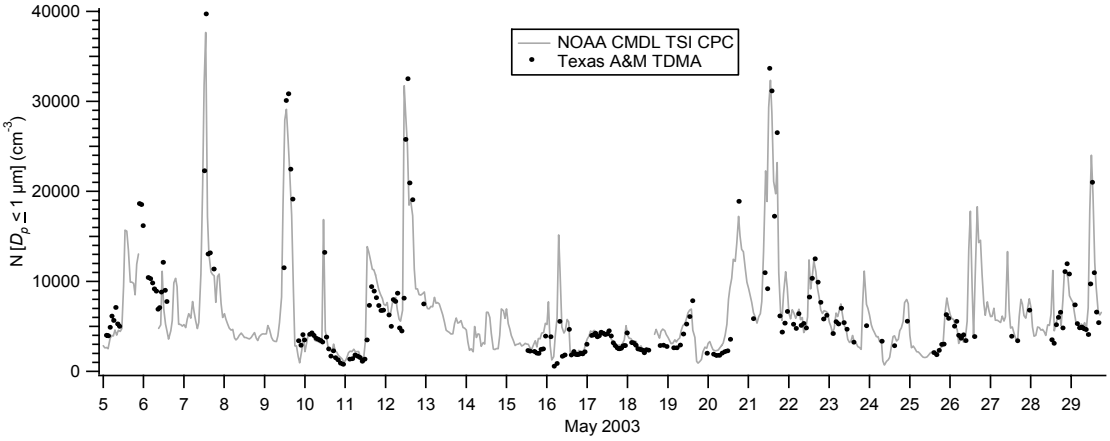

Figure 2. Comparison of total submicron particle number concentrations measured by the Aerosol Observing System with the total number concentration calculated by integrating the submicron aerosol size distributions measured with the Texas A&M DMA/TDMA.

2.2. Aerosol Observing System

The AOS measures a range of quantities including total aerosol scattering, hemispheric backscattering, and light absorption, which are needed to quantify the direct radiative climate forcing by the aerosol. The AOS instrument package includes a humidograph, which incorporates two three-wavelength (0.450, 0.550, and 0.700 μm) TSI 3563 nephelometers and a humidifier to measure the RH-dependence of aerosol scattering [*Carrico et al.*, 1998]. One "dry" nephelometer is always kept at low RH (~10-35%), while the RH is scanned in the second "wet" nephelometer [*Sheridan et al*., 2001]. The humidifier through which the sample flows prior to entering the wet nephelometer consists of a wire mesh tube surrounded by a water vapor permeable membrane. The RH of the sample flow is varied through adjustment of the temperature of a counter-flow water stream around this tube and membrane.

The RH in the wet nephelometer is typically varied between approximately 40 and 85%. However, insufficient ventilation of heat generated by pumps near the humidograph during the IOP limited the upper RH to ~75%. A scan over the full RH range requires one hour, and the RH resolution of the data is controlled by the rate of change over each of the 1-minute averaging intervals. All nephelometer data are corrected for angular truncation through the technique described in the work of *Anderson and Ogren* [1998].

2.3. DRI CCN Spectrometer

CCN spectra were measured during the Aerosol IOP using two DRI streamwise gradient CCN spectrometers [*Hudson*, 1989], one operating at lower supersaturations and one at higher supersaturations. Each DRI CCN spectrometer consists of a thermal gradient diffusion chamber employing multiple thermoelectric elements along the path of sample flow such that the centerline supersaturation increases monotonically with proximity to the chamber outlet. Activated droplets are then sized optically with a Royco white light Optical Particle Counter (OPC). The size distribution measured with the OPC is then translated into a CCN spectrum by employing a calibration-based relationship between outlet droplet size and critical supersaturation.

During the Aerosol IOP, spectra were collected with the two DRI CCN spectrometers with approximately 10-second time resolution. Simultaneous measurements by the two DRI CCN spectrometers were later combined to create cumulative CCN spectra spanning the critical supersaturation range between the minimum of the lower supersaturation spectrometer and the maximum of the higher supersaturation spectrometer. Each spectrum included measurements of CCN concentrations at some or all of the following 19 critical supersaturations: 0.02, 0.04, 0.06, 0.08, 0.09, 0.10, 0.15, 0.20, 0.25, 0.30, 0.40, 0.50, 0.60, 0.70, 0.80, 0.90, 0.95, 1.00, and 1.05%.

3. OBSERVATIONS AND DISCUSSION*

Aerosol size distributions and size-resolved hygroscopicity were measured sequentially. A complete set of these measurements will hereafter be referred to as a loop. A total of 239 loops were completed during the May 2003 Aerosol IOP, each of which consisted of a submicron size distribution measurement and hygroscopic growth measurements G(85) at eight dry diameters: 0.012, 0.025, 0.050, 0.100, 0.200, 0.300, 0.450, and 0.600 μm. During 12 of these 239 loops, particles with dry diameters of 0.050, 0.100, and 0.200 μm were analyzed in greater detail by scanning the RH and temperature in the manner described in the previous section. All data were analyzed using a Twomey-based inversion algorithm described in the work of *Collins et al.* [2002]. Since hygroscopic growth factor distributions tend to be modal by nature, they were all parameterized by fitting them with between one and four lognormals. For the discussion that follows, the mode within a growth factor distribution for which the corresponding lognormal had the greatest integrated concentration will be referred to as the dominant mode. Focus on the dominant mode is justified since the integrated concentration of this mode was typically significantly larger than the concentration of the second largest mode. For the 1787 growth factor distributions considered in this analysis, the average

---

contribution from the dominant mode was 79% while the average contribution from the second largest mode was only 18%.

Box plots showing the median growth factor of the dominant mode in each hygroscopic growth factor distribution as a function of dry diameter are shown in Figure 3. Considering all of the growth factor distributions collectively, the hygroscopicity of the aerosol observed during the IOP increased with increasing dry diameter, with an average median growth factor at 85% RH of 1.20 at 0.012 μm and 1.37 at 0.300 μm. The limited hygroscopic growth of the smallest particles analyzed suggests they are composed largely of carbonaceous compounds. Although the substantial increase in particle mass corresponding to the growth from nucleation to the smallest size considered here precludes identification of the species responsible for particle formation, these data do suggest that the initial growth is dominated by secondary organic species. The addition of sulfate through gas- and aqueous-phase reactions is probably responsible for the observed increase in hygroscopicity with size. The inorganic composition of aerosol samples collected by researchers from the NOAA Pacific Marine Environmental Laboratory during the springtime of 2000 and 2001 indicates that sulfate contributed 30% of the total submicron aerosol mass, while nitrate contributed just over 1% [*Iziomon and Lohmann*, 2003b]. Measurements made with a Particle-Into-Liquid Sampler [PILS, *Weber et al.*, 2001] operated by researchers from Brookhaven National Laboratory during the Aerosol IOP also support the conclusion that sulfate is the dominant inorganic aerosol type at the ARM SGP site (Y.-N. Lee, manuscript in preparation, 2005). Averaged over the study period, the sulfate mass concentration was

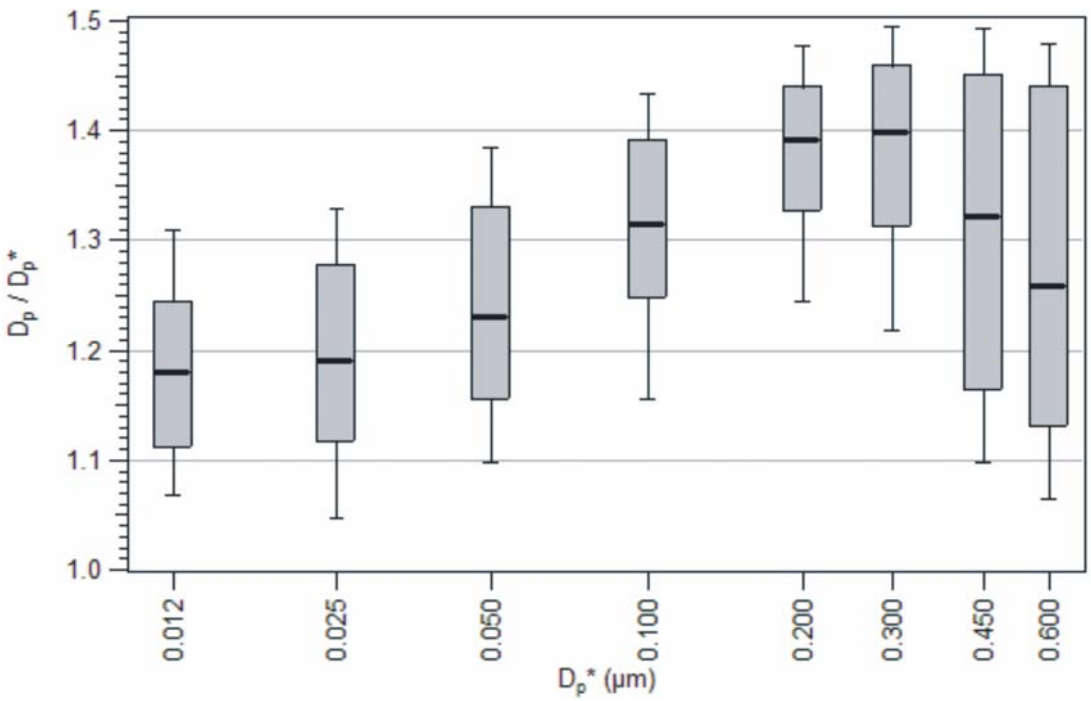

Figure 3. Box plots showing the median growth factor of the dominant mode at each dry diameter for all 239 measurement loops during the Aerosol IOP. The horizontal bar in each box represents the median, the box spans the range from the 25th to the 75th percentiles, and the whiskers denote the 10th and 90th percentiles.

95 times greater than that of nitrate. Figure 3 shows that for dry diameters greater than 0.300 μm the median growth factor decreased with increasing dry diameter, and that the variability in the growth factor of the dominant mode was much greater for the two largest particle sizes analyzed. A non-hygroscopic mode with a median growth factor less than 1.10 was sometimes observed at 0.450 μm and 0.600 μm, though one was rarely observed at 0.200 μm and 0.300 μm. These non-hygroscopic modes were likely due to the presence of a coarse dust mode in the size distribution whose tail on the smaller particle side only influenced the measurements at the largest dry diameters. Traffic on the numerous dirt roads surrounding the Central Facility of the ARM SGP site may have elevated the dust concentration and contributed to the concentration of submicron non-hygroscopic particles.

Figure 4 shows a timeline of the median growth factor of the dominant mode at each dry diameter for the 239 loops measured during the Aerosol IOP. The persistent trend of increasing hygroscopicity with increasing dry diameter is further emphasized in this figure. Figure 4 also shows that the largest particles considered were usually either very hygroscopic or only sparingly hygroscopic, but rarely in between these extremes. A few points in Figure 4, in addition to three points that are not depicted in Figure 4 marking growth factors greater than 1.80 on May 04, represent extremely high growth factors. Such erroneously high growth factors indicate that the instrument was not correctly calibrated at the time of those measurements. While the precise growth factors measured at those times were not correct, they are still useful in a relative sense since the calibration error likely caused a shift in growth factors that resulted in hygroscopic

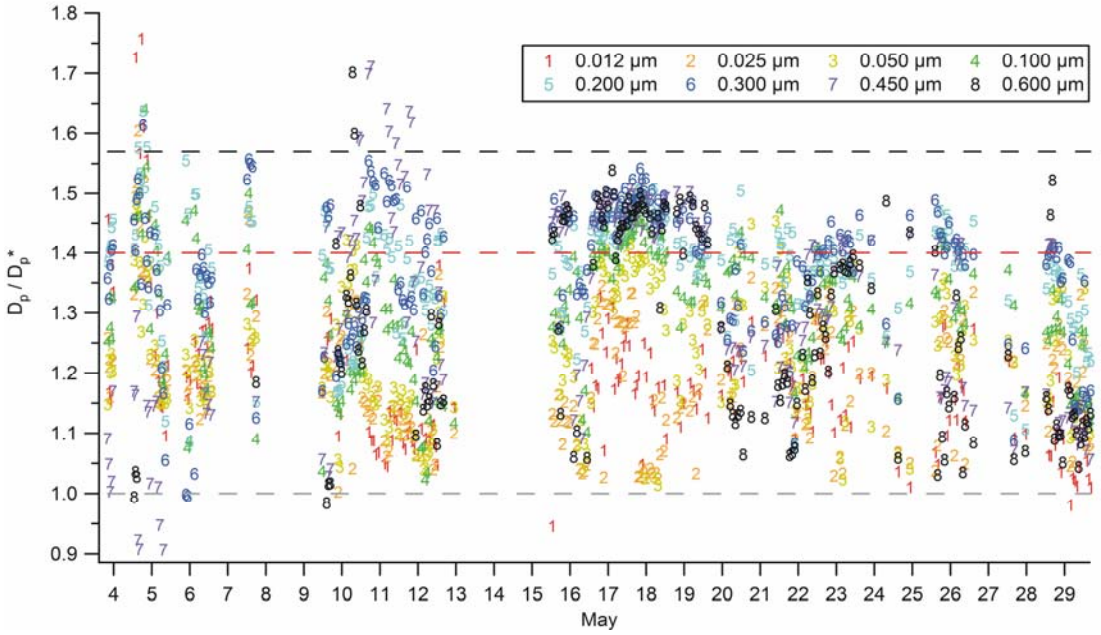

Figure 4. Timeline of the median growth factors of the dominant mode for the eight dry diameters in each of the 239 measurement loops during the Aerosol IOP. The dashed gray horizontal line marks a growth factor of 1.0, the dashed red horizontal line marks the expected growth factor at 85% RH of a 0.012-µm pure ammonium sulfate particle (D_p/D_p^* = 1.40), and the dashed black horizontal line marks the expected growth factor at 85% RH of a 0.600-µm pure ammonium sulfate particle (D_p/D_p^* = 1.57). The growth factors of pure ammonium sulfate particles were calculated using data from the work of *Tang and Munkelwitz* [1994].

particles appearing excessively hygroscopic. Because of their utility as relative measurements, they were not discarded. All DMA/TDMA data were subsequently corrected for flow and voltage control errors using daily midnight scans at dry conditions (RH < 20%).

In order to examine the short-term temporal variability of aerosol hygroscopicity, growth factor distributions were separated by loop start time into eight three-hour intervals covering the 24-hour day. Box plots showing the median growth factor of the dominant mode in each hygroscopic growth factor distribution binned according to local time are shown in Figure 5. In addition to highlighting the increase in hygroscopic growth with increasing dry diameter, Figure 5 also shows that at dry diameters of 0.300 μm or less, hygroscopicity increased in the morning and afternoon before decreasing in the evening and overnight hours. Increased aqueous-phase sulfate production resulting from increased convective cloud coverage in the morning and afternoon may have contributed to this daily cycle. Data recorded by the automated National Weather Service observation station in Ponca City, Oklahoma, about 30 km east-northeast of the ARM SGP Central Facility, showed that between 06:00 and 12:00 local time on the 31 days in May 2003, cloud bases were lower than 1 km on 13 days and between 1 km and 2 km on 5 days [*Lackey*, 2004]. However, similar behavior observed for particles with dry diameters of 0.025 μm or less, which are likely too small to activate in cloud, suggests that gas-phase reactions were also important.

Backtrajectories of parcels arriving 150 m above ground level at the ARM SGP Central Facility were calculated using the NOAA HYSPLIT4 model [*Draxler*, 1988] at

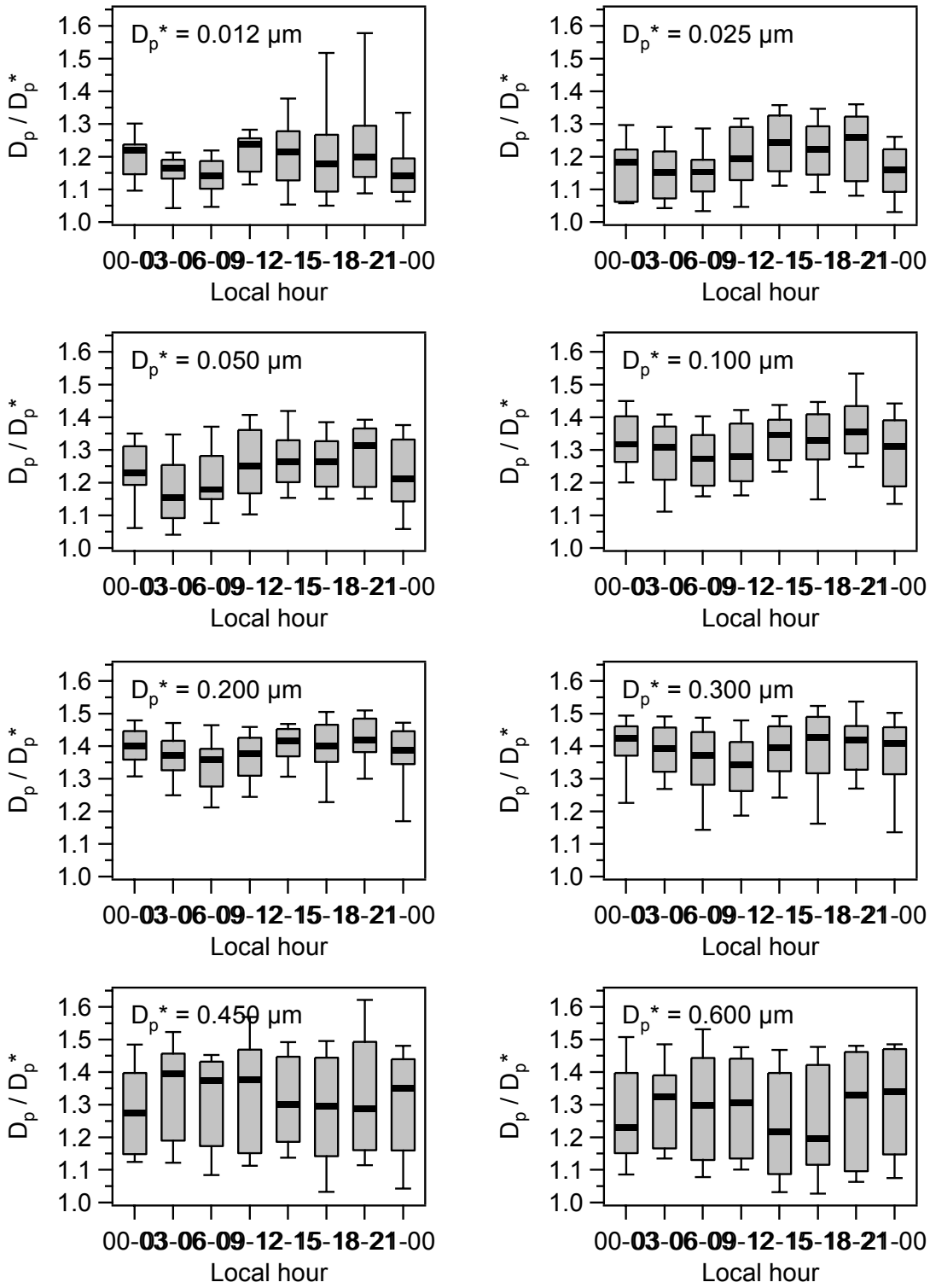

Figure 5. Box plots showing the median growth factor of the dominant mode in each growth factor distribution as a function of time of day.

three-hour intervals for the entire Aerosol IOP. In order to establish the dominant profiles among these 219 backtrajectories, similar backtrajectories were grouped using the cluster analysis technique described by *Dorling et al.* [1992]. This analysis resulted in eight distinct backtrajectory clusters. Because of the small number of observations associated with several of the backtrajectory clusters, some of the visually similar clusters were merged into four classifications that were more statistically-significant. Figure 6 shows the original eight clusters and their grouping into the four backtrajectory classifications considered in the analysis that follows. These represent backtrajectories from the northwest, Midwest, southeast, and southwest.

Since backtrajectories were created at three-hour intervals, each backtrajectory was assumed to be representative of the aerosol advection pattern for 1.5 hours before and after the end time of each trajectory. The start time of each DMA/TDMA loop was used to associate the hygroscopic growth factor distributions in that loop with a backtrajectory by matching the start time with the three-hour time window in which it occurred. Figure 7 shows box plots for each backtrajectory classification of the median growth factor of the dominant mode in each hygroscopic growth factor distribution as a function of dry diameter. During periods in which backtrajectories were from the northwest, increasing hygroscopicity was observed with increasing dry diameter except at the largest sizes. At 0.600 μm, the particles were mostly non-hygroscopic. A plausible explanation for this size-dependence is initial growth of recently-nucleated particles through condensation of SOA, addition of sulfate to larger particles primarily through in-cloud aqueous phase reactions, and the influence of a tail of a coarse mode

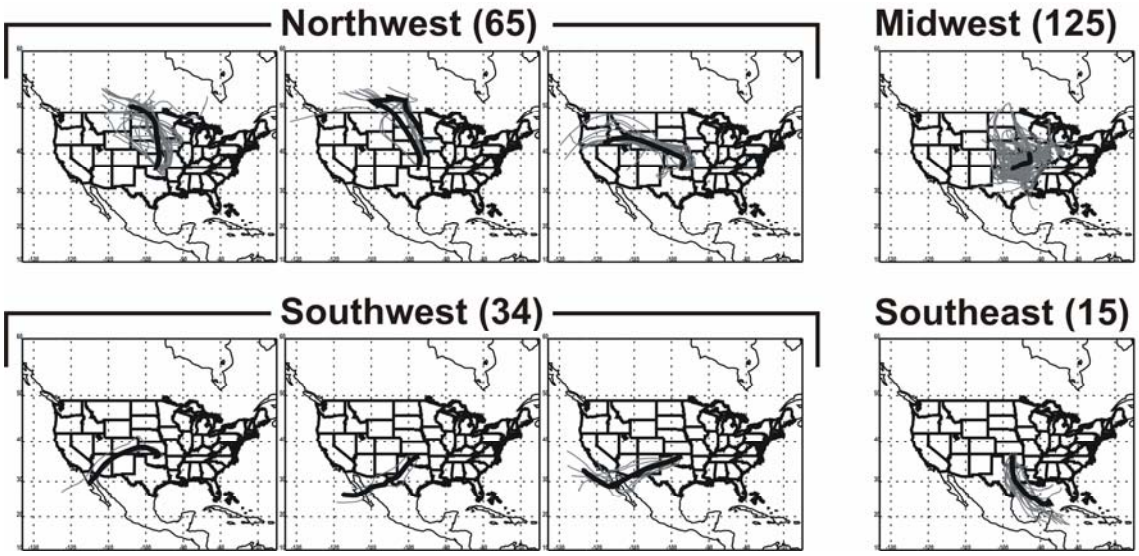

Figure 6. Results of the cluster analysis performed on the backtrajectories calculated for each three-hour period during the Aerosol IOP. Individual backtrajectories are plotted in gray, and the cluster mean backtrajectory is marked by the thick black arrow in each plot with large dots marking 24-hour increments. The eight clusters were combined into the four classifications shown here: northwest, Midwest, southeast, and southwest. The numbers in parentheses denote the number of measurement loops linked to each classification.

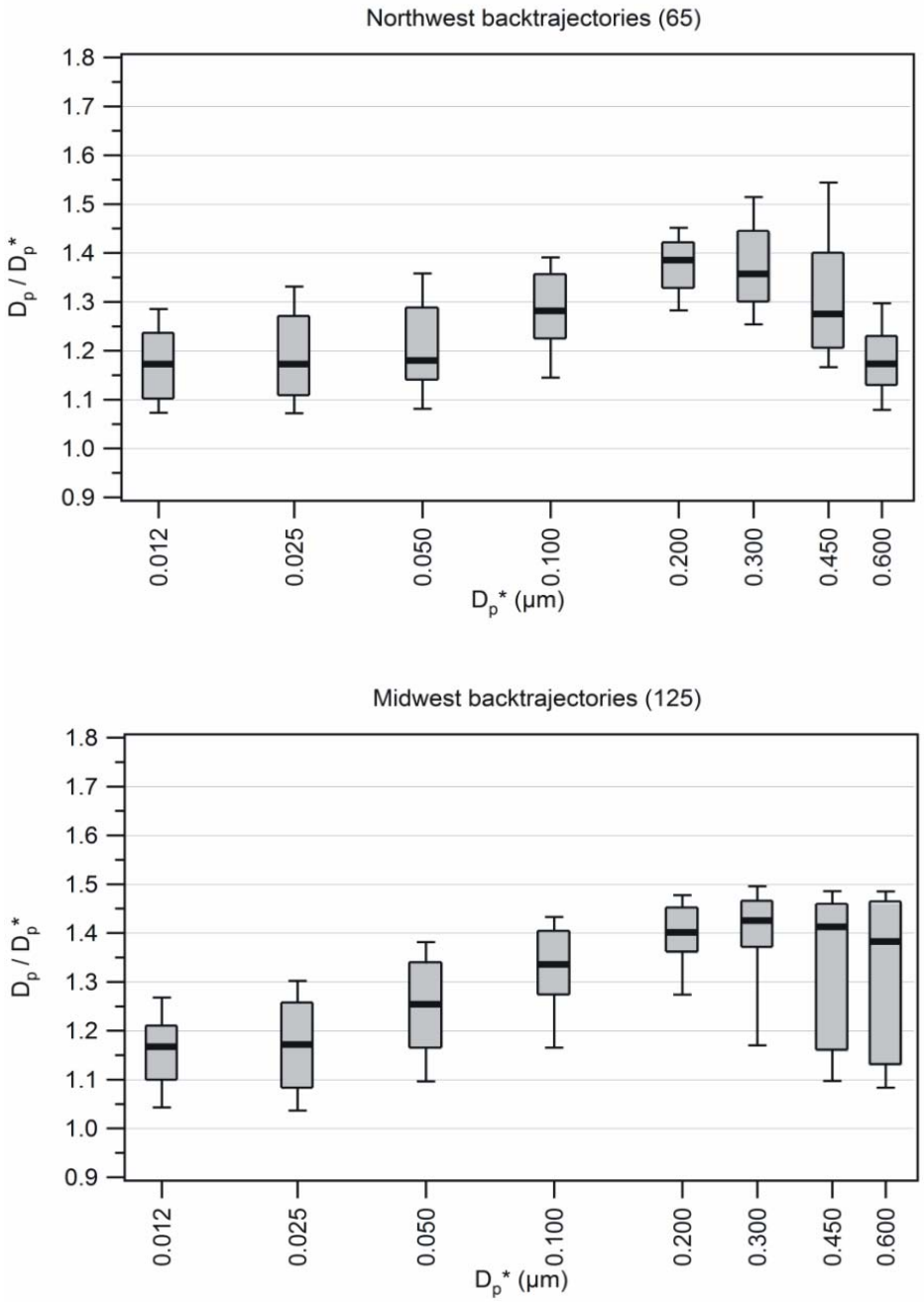

Figure 7. Box plots showing the median growth factor of the dominant mode as a function of dry diameter, separated by backtrajectory classification.

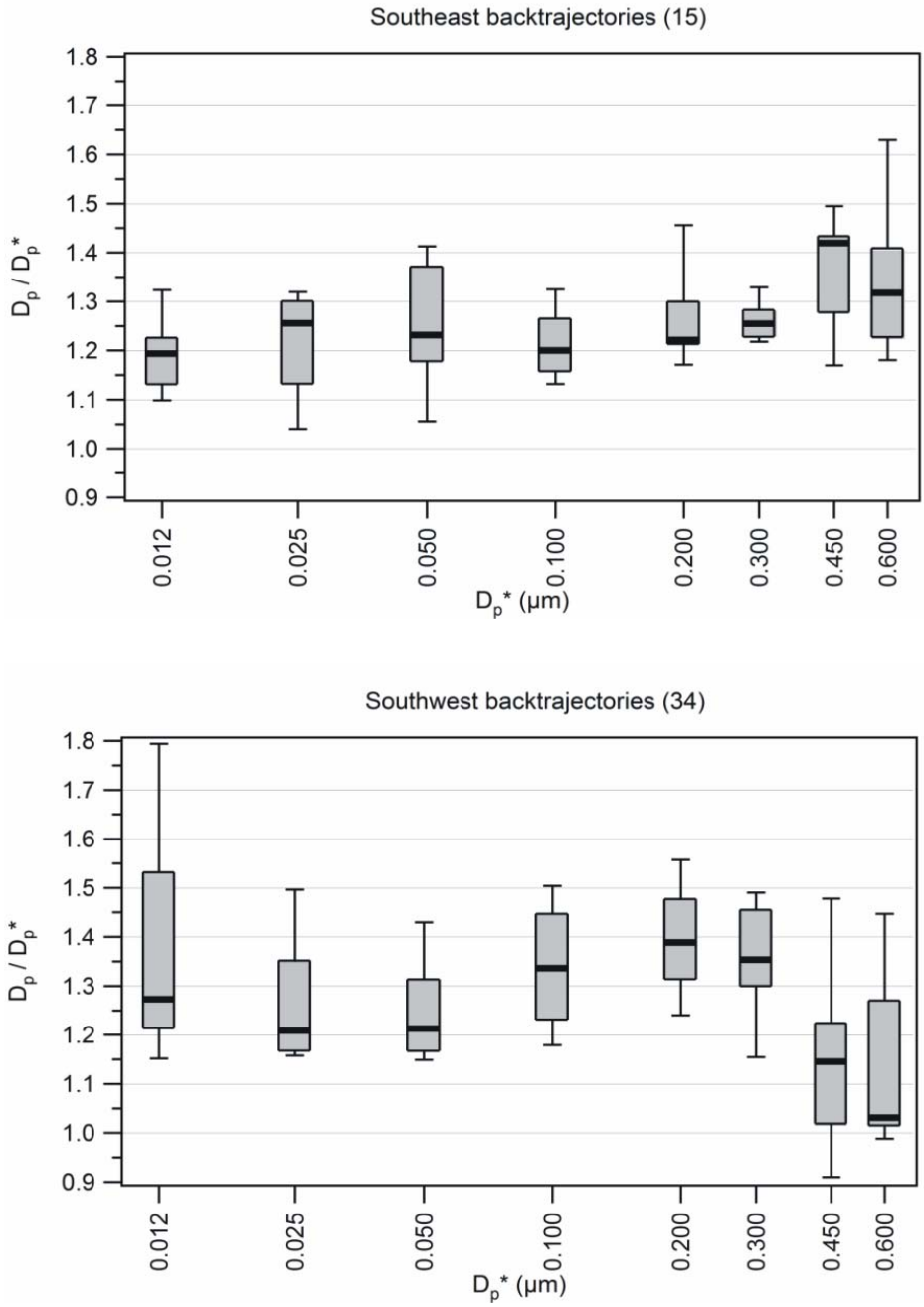

Figure 7 (continued).

that is responsible for the non-hygroscopic large particles. Hygroscopicity also increased with increasing particle size during periods in which backtrajectories were from the Midwest, although particles having dry diameters of 0.300, 0.450, and 0.600 μm were considerably more hygroscopic than particles of those same sizes when backtrajectories were from the northwest. This enhanced hygroscopicity of the larger particles from the Midwest is possibly a result of anthropogenic emissions of sulfur dioxide and other inorganic aerosol precursors from a number of urban and industrial sources. During periods in which backtrajectories were from the southeast, the aerosol was only sparingly hygroscopic with a median growth factor of 1.20-1.25 at all six dry diameters from 0.012 μm to 0.300 μm. Most of these observations were made on May 09-10, during which time backtrajectories trace the aerosol to the Yucatan Peninsula. Archived visible satellite images from that time and area show a large smoke plume from numerous wildfires being advected to the north and west, across the Gulf of Mexico to the U.S. mainland. Based on the limited hygroscopicity measured and the backtrajectories tracing the aerosol to a region of extensive biomass burning, it is believed that this aerosol was dominated by smoke. Growth factor distributions of 0.012-μm particles measured when the backtrajectories were from the southwest exhibited substantial variability. The range in hygroscopicity of these particles suggests a range in composition from almost pure secondary organic to almost pure sulfuric acid. The limited hygroscopic growth of 0.025-μm and 0.050-μm particles suggests that the addition of SOA may have controlled the initial growth of recently formed particles. The greater hygroscopic growth observed at 0.100, 0.200, and 0.300 μm was similar to

that observed when backtrajectories were from the northwest and Midwest. The low median growth factors of the dominant mode in the growth factor distributions measured at 0.450 μm and 0.600 μm indicate that non-hygroscopic particles, perhaps from the tail of a coarse mode, often dominated at the larger submicron sizes.

Since both RH scans and temperature scans took approximately one hour to complete, these more detailed measurements were only made occasionally. Therefore, their analysis is presented only for insight into individual cases. Figure 8 shows the results of RH and temperature scans for particles with dry diameters of 0.050, 0.100, and 0.200 μm. Figure 8a displays data from May 20, when the aerosol source region was northwest of the ARM SGP site. Deliquescence was observed at ~80% RH, crystallization was observed at ~35% RH, and the dominant hygroscopic particle type volatilized at or above ~175°C at all three dry diameters measured. These characteristics are consistent with an aerosol having a soluble inorganic fraction composed primarily of ammonium sulfate. At temperatures exceeding ~200°C, measurements at all three sizes show a residual non-volatile aerosol mode having a median diameter that is approximately 30-40% of that of the initial particles. This residual aerosol may be the insoluble cores of particles that had been coated with ammonium sulfate. In the plots showing data collected during RH scans for dry diameters of 0.100 μm and 0.200 μm, a secondary mode consisting of non-hygroscopic particles is evident only at high RH. This mode was likely obscured below 80% RH by the dominant ammonium sulfate-coated aerosol mode.

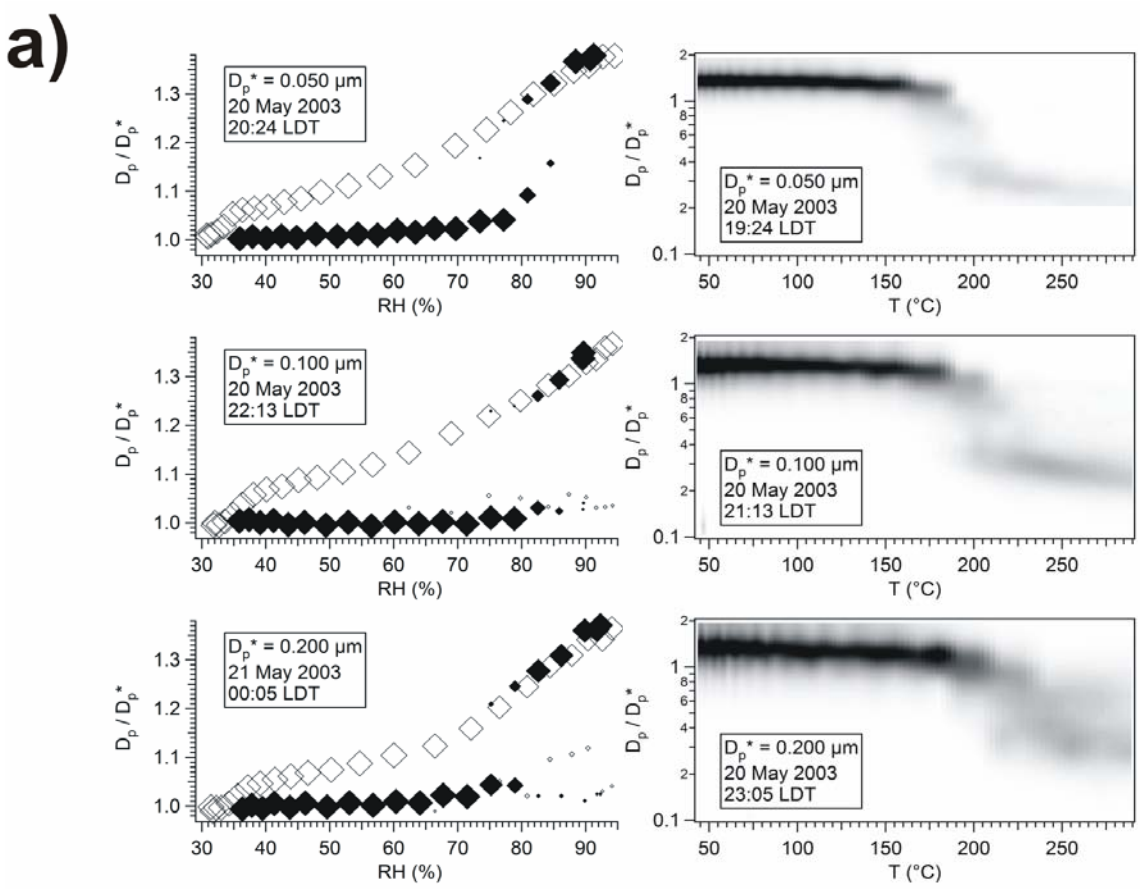

Figure 8. The first column contains plots of RH scan data collected on (a) 20 May 2003, when the aerosol source region was northwest of the ARM SGP site, and (b) 27 May 2003, when the source region was the Midwest, for 0.050-, 0.100-, and 0.200-µm dry diameter particles. The darkened diamonds and hollow diamonds represent the median growth factors of each mode observed during measurements made when the aerosol was not pre-humidified and when it was, respectively. Marker size reflects the relative concentration when multiple modes were observed. The second column contains plots of temperature scan data from the same day at the same sizes. Darker shading corresponds to higher concentrations.

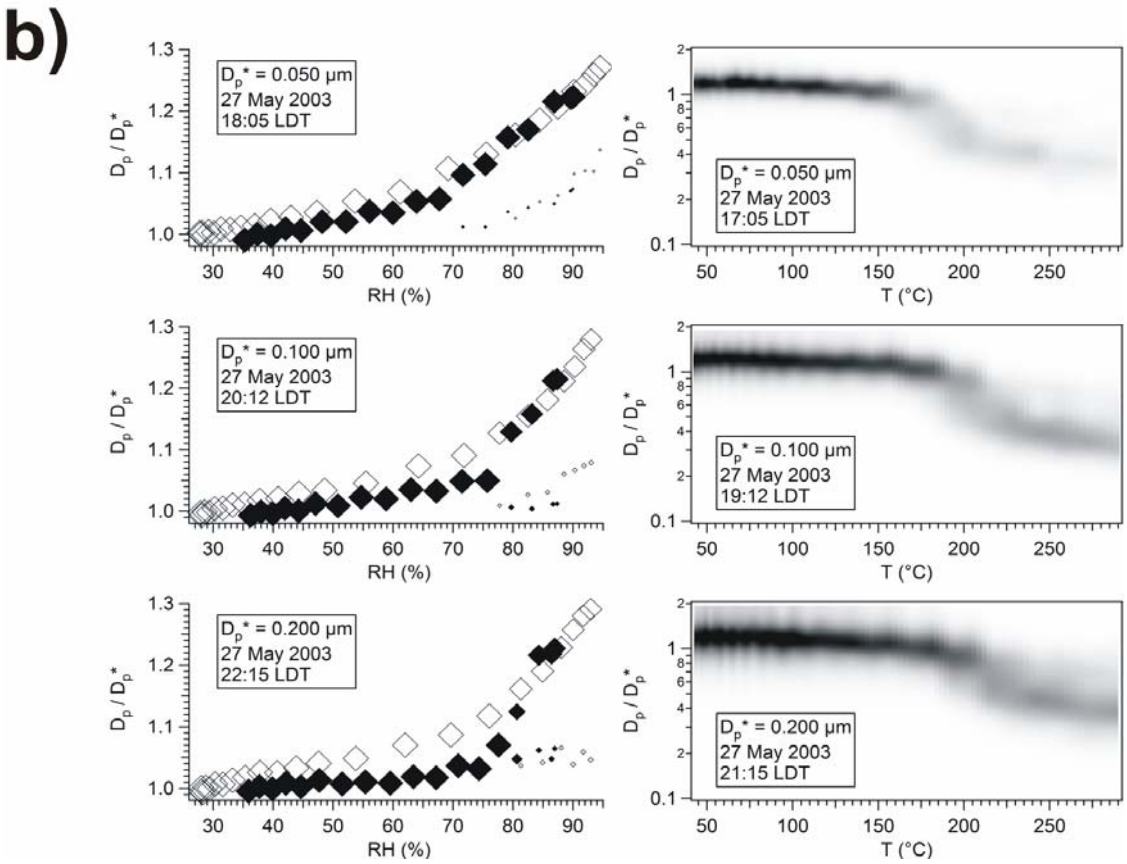

Figure 8 (continued).

Figure 8b shows a complete set of RH and temperature scans from one week later on May 27, when the aerosol source region was the Midwest. Unlike the previous week when the aerosol exhibited clear hygroscopic growth hysteresis at 0.050, 0.100, and 0.200 μm, there was only a slight displacement between the growth factor curves measured on May 27. The aerosol on this day was less hygroscopic than on May 20, which is probably the result of an increased concentration of carbonaceous species. The slopes of the growth factor curves measured on this day appear to increase with increasing RH to a greater extent than on May 20. A sparingly-soluble organic compound mixed with a more soluble inorganic would exhibit this pattern of enhanced hygroscopic growth at high RH. The temperature scans from May 27 shown in Figure 8b indicate that the non-volatile residuals that remained at temperatures exceeding 200°C were larger than those observed on May 20. Though volatility and composition are not uniquely related, it is believed that these residuals were carbonaceous.

4. MODE-RESOLVED HYGROSCOPICITY*

As would be true for measurements made at any other location, distinct modes within the size distributions measured during the Aerosol IOP were often observed to evolve slowly over a period of hours or even days. A greater understanding of the processes responsible for this evolution can be gained through examination of the hygroscopic growth measurements. Consideration of the hygroscopicity of particles with dry diameters nearest the median diameter of a size distribution mode could offer some insight into the changes in particle properties that accompany changes in particle size. Unfortunately, even if the aerosol within each size distribution mode is compositionally homogeneous, contributions of distinct particle types from several overlapping size distribution modes will be reflected in the fixed-size hygroscopic growth measurements. In order to facilitate examination of the evolution of aerosol populations, a model has been developed to couple measured size distributions and fixed-size hygroscopic growth factor distributions to describe mode-resolved hygroscopic properties.

Figure 9 provides a graphical depiction of the relationship between a size distribution possessing multiple modes that contain particles having distinct hygroscopic

---

* Parts of this section reproduced by permission of *American Geophysical Union*. Gasparini, R., R. Li, D. R. Collins, R. A. Ferrare, and V. G. Brackett, Application of aerosol hygroscopicity measured at the ARM Southern Great Plains site to examine composition and evolution, *J. Geophys. Res.*, in press, 2005. Copyright 2005 *American Geophysical Union*.

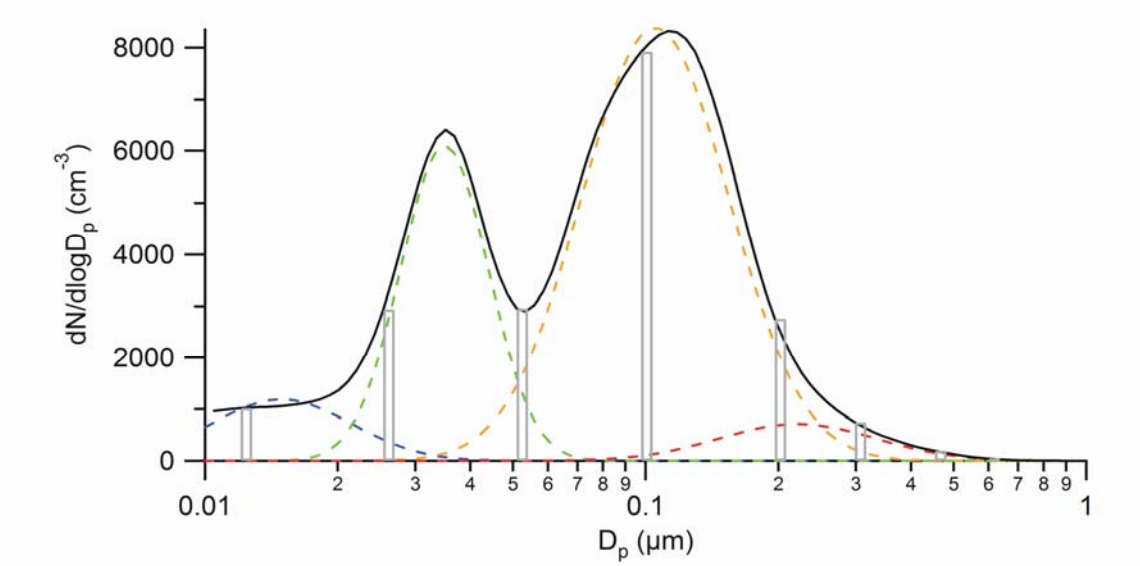

Figure 9. An example showing the convolution of a size distribution described by a series of lognormals and the mode-resolved hygroscopicity determined through the model described in Section 4. The top graph shows a size distribution measured at 20:45 local time on 22 May 2003. The bars represent the dry diameters at which growth factor distributions were measured. The four colored modes represent the lognormals used to fit this size distribution. The four mode-resolved growth factor distributions determined for this measurement loop are shown below the size distribution. The table displays the fractional contribution of each mode to the total number concentration at the eight dry diameters. The lowest graph shows the eight growth factor distributions measured (solid black line) and the eight growth factor distributions simulated by coupling the mode-resolved growth factor distributions weighted by the fractions listed in the table (dashed gray line). The scaled final mean-square error of this loop was 1.166, which indicates that more than half of the loops contain data that were deconvoluted more successfully than this one.

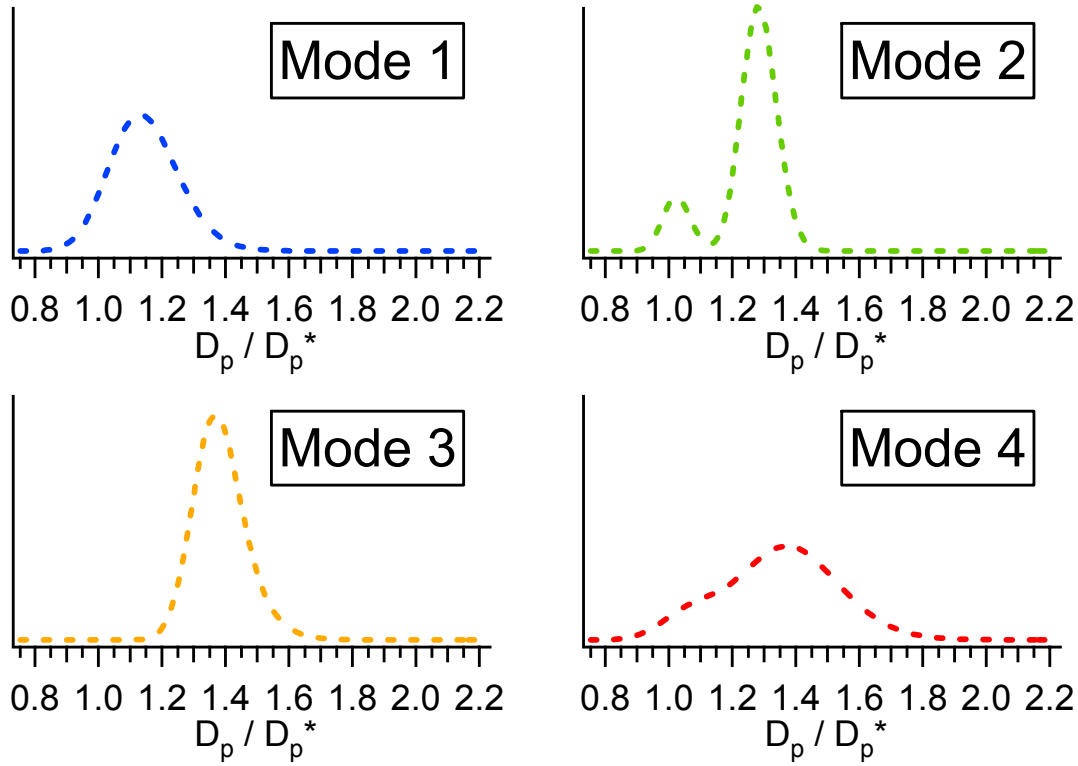

	D_p^* (µm)							
	0.012	**0.025**	**0.050**	**0.100**	**0.200**	**0.300**	**0.450**	**0.600**
Mode 1	0.9999	0.1688	0.0015	0.0000	0.0000	0.0000	0.0000	0.0000
Mode 2	0.0001	0.8279	0.5714	0.0000	0.0000	0.0000	0.0000	0.0000
Mode 3	0.0000	0.0033	0.4267	0.9869	0.7521	0.2779	0.0409	0.0087
Mode 4	0.0000	0.0000	0.0003	0.0130	0.2479	0.7222	0.9591	0.9913

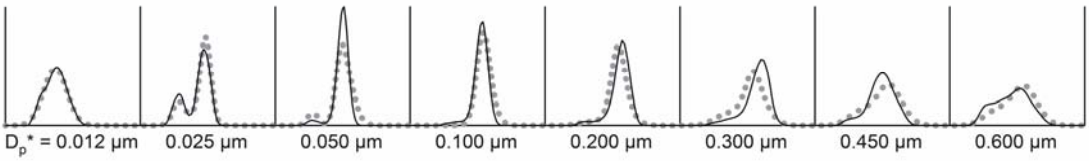

Figure 9 (continued).

properties and the resulting size-resolved hygroscopic growth factor distributions. A convolution of the size distribution and mode-resolved hygroscopicity results in size-resolved growth factor distributions. Therefore, deconvolution of the measured data is necessary to compute the desired mode-resolved hygroscopicity. To accomplish this, each mode within the size distribution in each loop was fitted with a lognormal. Particles within each size distribution mode were assumed to be hygroscopically homogeneous. As with the size distributions, each mode-resolved hygroscopic growth factor distribution was described by multiple lognormals. Growth factor distributions are simulated at the eight dry diameters at which measurements were made by summing the mode-resolved growth factor distributions weighted by the fractional contributions of each size distribution lognormal to the concentration at that dry diameter.

4.1. Parameterization and Adjustment Technique

Each measured size distribution was fitted with a combination of no more than four lognormals. Hygroscopic growth factor distributions were normalized since the relative concentration of particles at a given growth factor is significant whereas the absolute concentration is not. All growth factor distributions were also fit with no more than four lognormals. Of the 1912 growth factor distributions measured, 125 lacked sufficient particle counts to be accurately parameterized. Of the remaining 1787 distributions, considering only those modes that contained more than 10% of the total integrated growth factor distribution, 708 (39.6%) were monomodal, 924 (51.7%) were bimodal, 150 (8.4%) had three modes, and 5 (0.3%) had four modes. Because over 90%

of the measured growth factor distributions could be adequately described using either one or two modes, and because the computation time increased substantially as the number of hygroscopic modes was increased, a maximum of two lognormals were considered in this analysis.

The average geometric standard deviation of the lognormals used to describe the size distribution modes was 1.53. For a lognormal having this geometric standard deviation, the ratio of the diameters along the two sides of the distribution at half its height is 2.72. This is greater than the maximum ratio of adjacent dry diameters for which hygroscopic growth was measured. Therefore, each size distribution mode typically spanned a particle size range that encompassed multiple hygroscopic growth measurements. Additionally, because of the breadth of the size distribution lognormals, each dry diameter for which hygroscopicity was measured often consisted of significant contributions from multiple modes. For instance, the size distribution lognormal with the largest contribution to the number concentration at 0.025 μm contributed on average 83% of that concentration. At 0.100 μm, the average contribution from the most contributing mode was 74%.

The set of two lognormals used to represent each hygroscopic growth factor distribution can be described by a total of six parameters. Adjusting these six parameters for each mode-resolved growth factor distribution would subsequently change the simulated growth factor distributions at the eight dry diameters for which hygroscopicity was directly measured. The sum of the mean-square errors between each of the eight measured and simulated hygroscopic growth distribution was used to describe the ability

of the model to represent the aerosol as a series of compositionally-uniform size distribution modes. Because only the sum of mean-square errors will be considered, and not that between any individual simulated and measured distribution, this sum will be referred to simply as the mean-square error (MSE). The mathematical objective of the model used to determine the mode-resolved hygroscopic growth distributions was minimization of this MSE. To accomplish this, the parameters describing the mode-resolved growth factor distributions were optimized through the use of a Levenberg-Marquardt algorithm.

The initial guess of the mode-resolved hygroscopic properties needed to initiate the Levenberg-Marquardt algorithm was generated using the following approach. The fractional contribution of each of the size distribution lognormals to the particle concentration at the eight dry diameters for which growth factors were measured was first determined. For each size distribution mode, the dry diameter for which the size distribution lognormal contributed the highest percentage to the number concentration was selected. The parameters defining the one or two most dominant modes of the measured growth factor distribution at that selected dry diameter were used as the initial guess for that mode-resolved growth factor distribution. The MSE between the measured size-resolved hygroscopic growth distributions and those simulated using this initial guess was calculated to provide a basis for comparison with the model solution.

For each DMA/TDMA measurement loop, the Levenberg-Marquardt algorithm was called in a five-step adjustment sequence, with each call attempting to adjust only a subset of the parameters defining the mode-resolved growth factor distributions. This

sequential adjustment approach was found to produce better results than when all parameters were varied simultaneously. The sequence first adjusted the normalized concentrations, then the normalized concentrations and the median growth factors simultaneously, then the geometric standard deviations, then the median growth factors again, and finally both the normalized concentrations and geometric standard deviations. When the MSE decreased after a call to the algorithm, the new parameters were used as the guess parameters in the next call. The parameters for each loop were adjusted until either the MSE after the fifth and final call of an entire sequence was within two percent of the MSE of the previous call or when the entire sequence had been cycled through four times for a total of twenty calls to the algorithm.

The performance of this deconvolution technique is quantified by the MSE between the measured data and the simulated growth factor distributions. For the 239 measurement loops, the deconvolution technique reduced the MSE by an average of 80% relative to that computed using the initial guess. Since the size-resolved hygroscopic growth factor distributions were normalized, the numerical value of the MSE is meaningless. To facilitate comparison of the model performance at different times during the IOP, the final MSEs were scaled by dividing by the median value among all of the final MSEs. Thus, among the 239 loops, the loop with the median final MSE has a scaled final MSE of 1.0. Figure 10 shows the actual and simulated growth factor distributions for five loops representing the 1^{st}, 25^{th}, 50^{th}, 75^{th}, and 99^{th} percentile scaled final MSEs. A first-order visual evaluation of Figure 10 indicates that the simulated growth factor distributions in the loop with the 50^{th} percentile scaled final

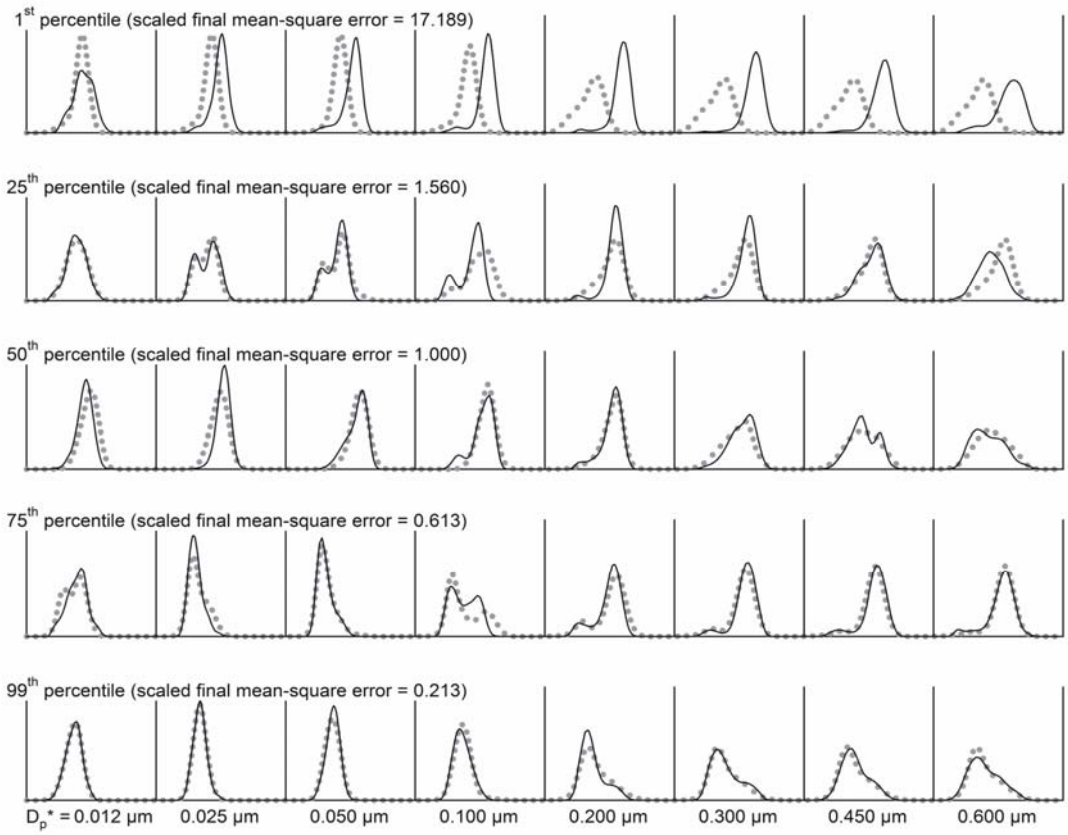

Figure 10. Examples showing the agreement between the measured (solid black line) and simulated (dashed gray line) size-resolved hygroscopic growth factor distributions. The scaled final mean-square error corresponding to each set of distributions is also included. The top row of plots represents the 1st percentile of scaled final mean-square error (worst agreement) and the bottom row of plots represents the 99th percentile (best agreement).

MSE appear to closely match the actual measurements, and even those in the loop with the 25th percentile scaled final MSE reasonably match the observations.

4.2. Analysis of Hygroscopic Homogeneity

The deconvolution of mode-resolved growth factor distributions from the measured size distributions and size-resolved hygroscopicity is sensitive to the validity of the inherent assumption that particles within each mode have uniform hygroscopic properties. This sensitivity is reflected in a degradation of the agreement between the simulated and measured size-resolved growth factor distributions, and a corresponding increase in the calculated MSE, with increasing heterogeneity. Aerosols whose size-resolved growth factor distributions contain multiple distinct modes can present cases that mode-resolved growth factor distributions described by a maximum of only two modes simply cannot resolve. Urban aerosols consisting of a range of distinct particle types are among the most challenging to describe due to their hygroscopic heterogeneity [*Cocker et al.*, 2001].

Figure 11 shows box plots of the scaled final MSE for each of the four backtrajectory classifications. From this figure, the best agreement was most often achieved for measurements made during periods in which the backtrajectories were from the northwest. Though they represent only a few outliers, some of the poorest agreement occurred when the backtrajectories were from the Midwest. This is possibly due to the inability of this simplified model to resolve heterogeneity of the aerosol in, and affected by, urban plumes. As discussed above, the aerosol from the southeast was strongly

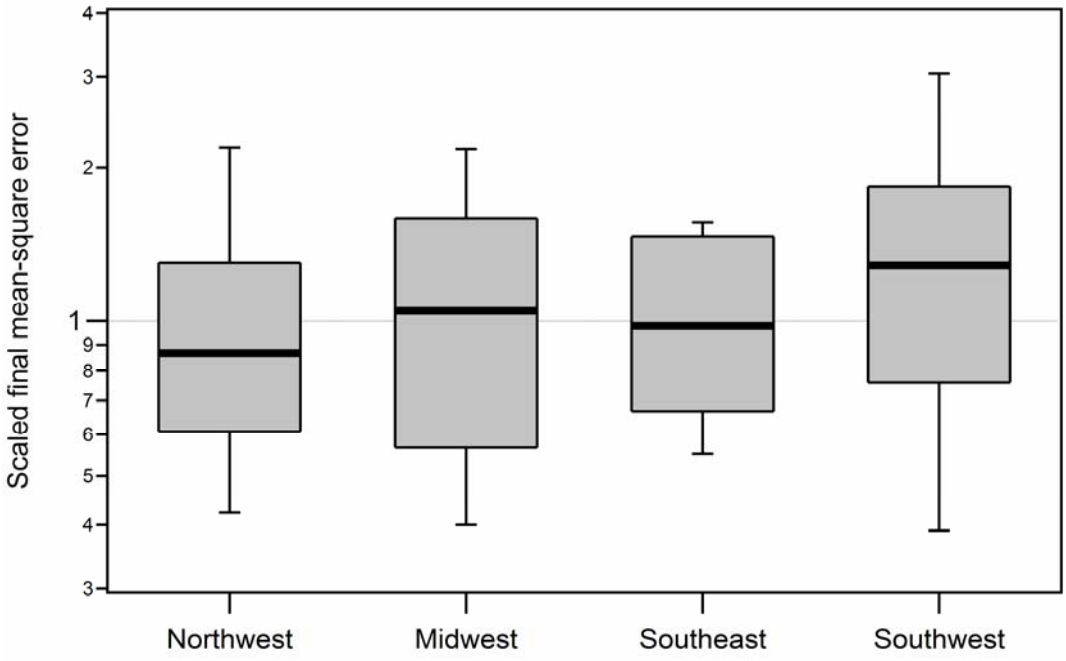

Figure 11. Box plots of the final scaled mean-square error as a function of backtrajectory classification.

influenced by biomass burning. The hygroscopic homogeneity of this biomass burning aerosol simplified computation of mode-resolved properties. Unlike that transported from the southeast, aerosol from the southwest could have been influenced by a number of regions, which is reflected in the observed variability in final scaled MSE.

4.3. Case Studies: May 11-12, May 16-17, and May 19

Understanding the factors responsible for transforming a size distribution mode is facilitated by considering the evolution of mode-resolved hygroscopicity. During the IOP, gradual changes in the median diameters of lognormals used to describe aerosol size distributions were observed over periods ranging from hours to days. May 11-12, May 16-17, and May 19 are three periods during which such growth was pronounced. Backtrajectories indicate that the aerosol arrived from the northwest on May 11-12 and from the Midwest on May 16-17 and May 19. Figure 12 contains time series of the median diameters of the size distribution modes for these three periods. The number concentration and median growth factor of the particles in each of the modes are represented by marker color and marker size, respectively. Although it is never possible to decouple the evolution of an aerosol population from changes observed at a fixed site that result from variations in sampled aerosol history, the persistent trends observed during these periods make them ideally suited for this type of analysis.

The overall goal of this analysis was to consider the relative importance of different growth mechanisms. The analysis here considers i) in-cloud aqueous phase production of sulfate, ii) condensation of both sulfuric acid and SOA when the gas-phase

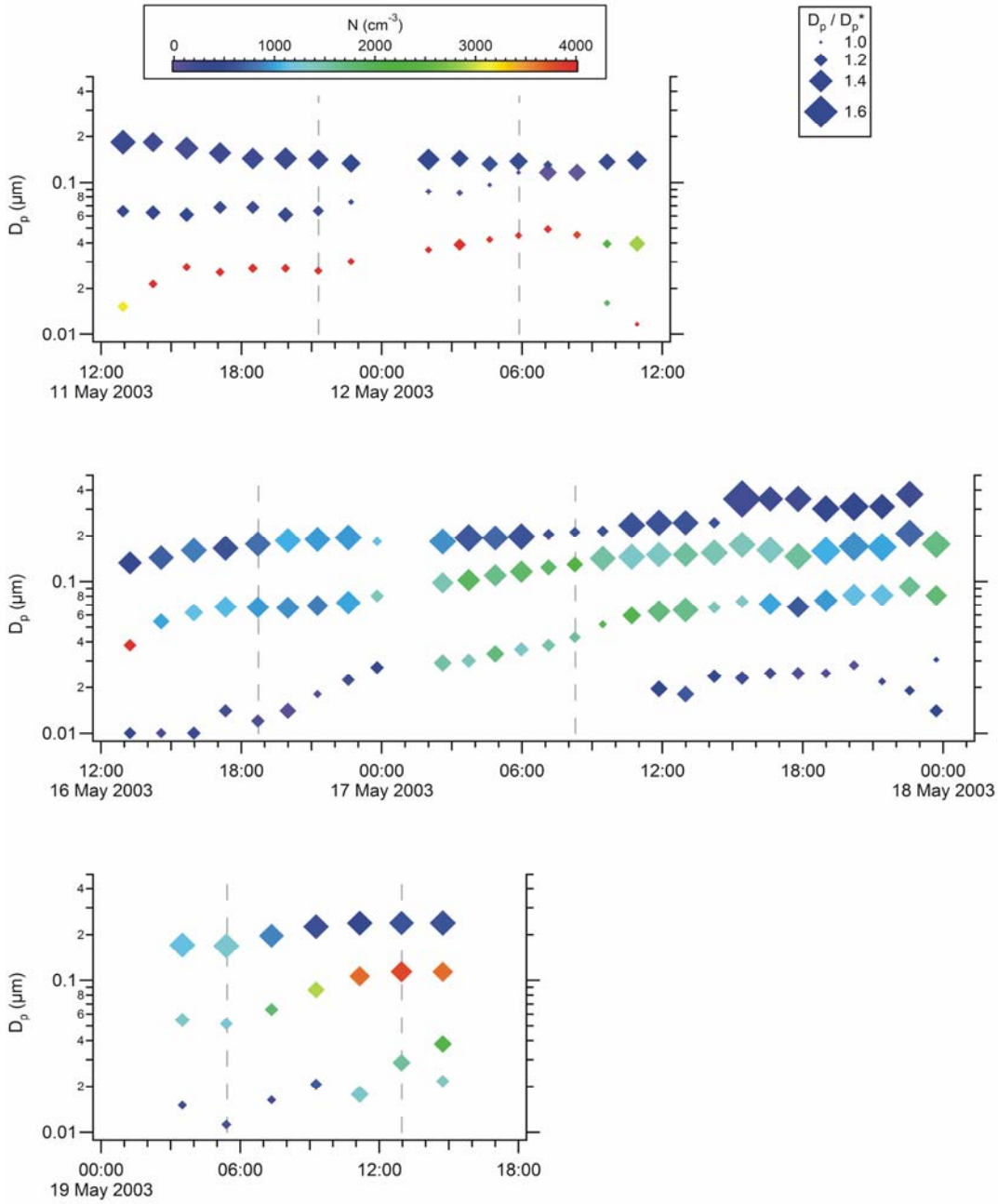

Figure 12. Time series from May 11-12, May 16-17, and May 19 showing the evolution of the median diameter and median growth factor in the mode-resolved growth factor distribution for each aerosol size distribution mode. Marker color is a function of the number concentration contained in the mode, and marker size increases with increasing median growth factor. The time periods bounded by the dashed vertical lines in each plot mark the specific periods considered for the computations shown in Figure 13.

species are supersaturated, and iii) partitioning of SOA into particles composed partially or completely of organic compounds when gas-phase species are subsaturated. Particles were assumed to be composed of a two-component mixture of organic compounds and ammonium sulfate. The organic fraction was assumed to be insoluble to simplify the analysis, although a more realistic representation would have had little impact on the results. For a given size distribution mode, the insoluble and soluble fractions of particles within that mode were determined by using the mode-resolved growth factor distribution calculated for that mode. The soluble fraction in that mode was calculated based on the relationship between soluble fraction and hygroscopic growth using solution activity and density relationships described in the work of *Tang and Munkelwitz* [1994]. The product of this soluble fraction and the total volume concentration within the size distribution mode will be referred to as the soluble volume. The difference between the total volume concentration in a mode and the soluble volume will be referred to as the insoluble volume.

In order to identify the mechanisms most likely contributing to evolution of aerosol size and composition, observed changes in the soluble and insoluble volumes over time were compared with the expected changes resulting from the three processes mentioned above. Quantification of the impact of the different mechanisms is facilitated by considering the differing effects they would have on each of the distinct size modes characterized. Because particles within the smallest diameter size distribution mode usually had predicted critical supersaturations exceeding expected peak supersaturations in typical convective clouds, they were assumed to be modified only through

condensation. The concentrations of gas-phase condensable species necessary to result in the observed increase in soluble (sulfate) modal volume concentration over time intervals during which growth was relatively monotonic were iteratively determined using equations governing condensational growth [*Seinfeld and Pandis*, 1998]. The specific time intervals used for each of the three cases are identified in Figure 12 by the dashed vertical lines. A similar procedure was used to determine the concentration of gas-phase organic compounds that would result in the increased insoluble volume when partitioning of subsaturated species into the aerosol phase was neglected. These calculated gas phase concentrations were then used to determine the expected growth of the particles within the size distribution mode having the second smallest median diameter due solely to condensation. The sensitivity of these calculations to assumptions regarding the hydration state of the aerosol was evaluated by repeating them for a scenario in which all particles were assumed to be at equilibrium at 85% RH throughout the growth period. The impact of the assumed hydration state on the final median diameter of the second size mode was found to be negligible. Therefore, particles were assumed to be dry to simplify the computations.

For those cases in which the soluble volume concentration increased over the time interval considered, the condensable species concentrations calculated based on the growth of the smallest particles was insufficient to explain the observed growth of particles in the second mode. Disparities in the soluble volume concentration are believed to be the result of in-cloud aqueous phase reactions that add sulfate only to the larger particles in the second mode, which are expected to activate in cloud. As will be

discussed below, this conclusion is supported by local cloud cover observations. The insoluble volume concentration within the second mode increased more than can be explained through simple condensation of one or more supersaturated gas-phase compounds. This observation suggests that subsaturated organic species partitioned into the aerosol phase. Whereas the condensational growth rate due to organics that do not interact with the existing aerosol phase is approximately inversely related to particle size, the relative growth rate of the particles within the two modes considered due to partitioning between the gas and aerosol phase will be dependent upon the organic content of the two particle populations [*Odum et al.*, 1996]. Similar to the procedure described above, the growth rate of particles within the second size mode was predicted using a gas-phase concentration of some arbitrary organic compound that would result in the observed growth of particles within the first mode. Unlike the procedure described above, the organic volume added to the particles was assumed to be linearly related to the insoluble volume concentration already in the aerosol. This results in a significant enhancement in the growth of the larger particle modes.

Results of this analysis for the mode having the second smallest median diameter for each of the three periods considered are shown in Figure 13. The shaded swaths in each insoluble volume plot are bounded by predictions assuming growth is through condensation of a supersaturated organic compound at the bottom and by that assuming growth is through partitioning of a subsaturated organic compound at the top. For each soluble volume plot, the shaded swaths are bounded by no change in volume concentration at the bottom and the projected growth by single-component condensation

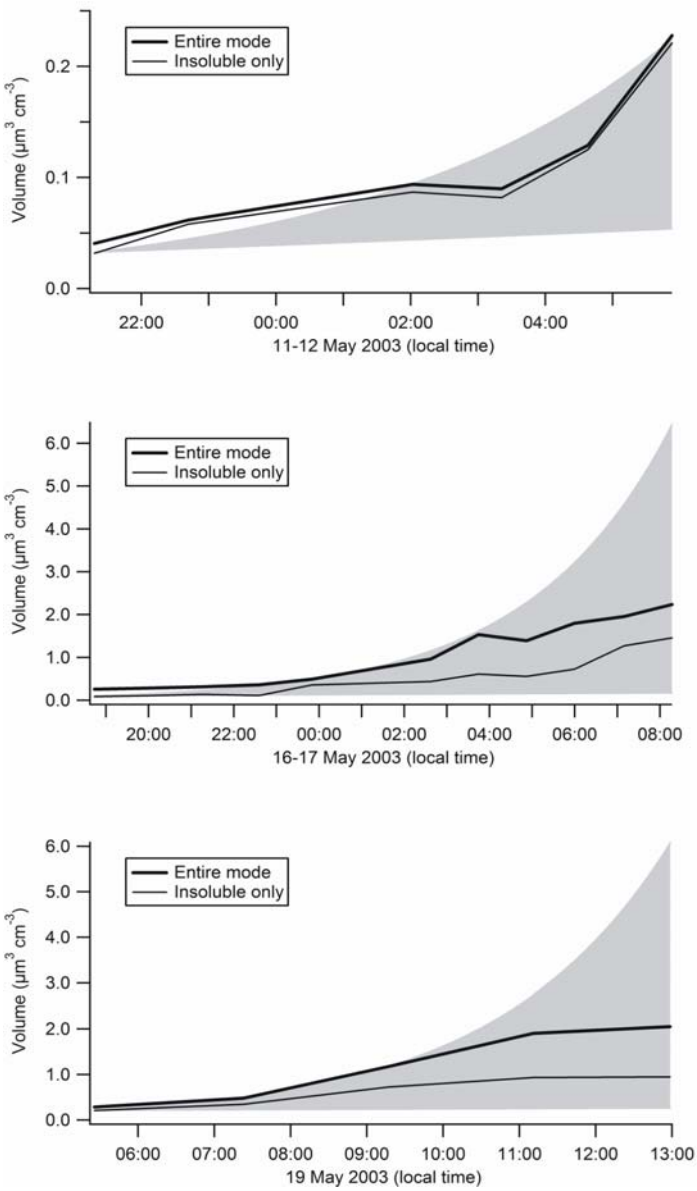

Figure 13. Time series from the same periods as Figure 13 tracking the added volume within the second smallest size distribution mode. The thick black line tracks the evolution of the total volume of the mode. The first page contains plots tracking the insoluble volume while the second page contains plots tracking the soluble volume. The shaded regions in the plots in the first page represent projected increases in the insoluble volume and are bounded by SOA formation when gas-phase organics are supersaturated at the bottom and partitioning of SOA into the existing organic aerosol when gas-phase organics are subsaturated at the top. The shaded regions in the plots in the second page represent projected increases in the soluble volume and are bounded by no growth at the bottom and single-component condensational growth at the top.

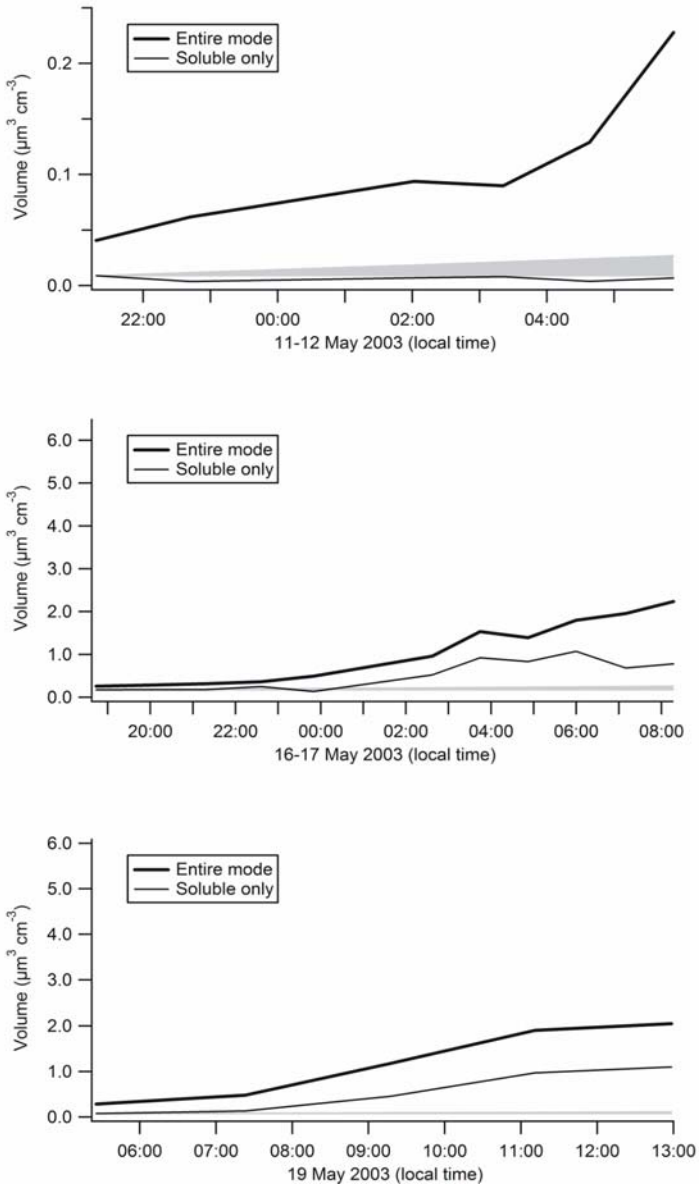

Figure 13 (continued).

at the top. The solid lines represent the measured total, soluble, and insoluble volume concentrations. Details of each of the three cases are provided below.

4.3.1. Case 1: May 11-12

Limited variability in both aerosol concentration and hygroscopicity was observed during the period from May 9 to May 12. Throughout this time, the hygroscopic properties of the aerosol were consistent with particles composed largely of organic compounds. Figure 12 shows that on May 11-12, the median diameters of the two lognormals representing the smallest particles increased gradually overnight, while the aerosol within these modes remained sparingly hygroscopic. The soluble volume in the second size mode did not change appreciably over the interval considered. In contrast, the insoluble volume increased by more than a factor of 5. The graphs for May 11-12 in Figure 13 indicate that the increase in insoluble volume concentration observed in the second size distribution mode was consistent with predictions based on the assumption that SOA partitioned into the existing organic aerosol. The absence of significant changes in the hygroscopicity of particles within these two modes also implies that oxidation of organics within the particles did not appreciably change their behavior.

4.3.2. Cases 2 and 3: May 16-17 and May 19

On the evening of May 16 and through the morning of May 17, three modes were observed in the submicron size distribution. As shown in Figure 12, the median

diameters of all three modes gradually increased during this period. Particles within the smallest diameter mode were the least hygroscopic, and those within the largest diameter mode were the most hygroscopic. The simultaneous increase in the median diameter and hygroscopicity of the smallest diameter mode can be explained by condensation of soluble species such as sulfate. However, the graphs for May 16-17 in Figure 13 indicate that the observed increase in the soluble volume of the second mode exceeded the expected growth due solely to single-component condensation. The likely explanation for the inability to resolve the growth of the first and second modes through condensation only is the added growth of the larger diameter mode through aqueous phase reactions. During the initial stages of growth considered, the particles within the smaller mode had critical supersaturations exceeding 1%, making it unlikely that they activated in cloud. The addition of sulfate to the particles within the larger diameter mode through cloud processing was likely the cause of the enhanced growth observed in the second size distribution mode. According to the hourly measurements of various meteorological variables at the weather station in nearby Ponca City, clouds were prevalent within the boundary layer during the May 16-17 growth event. This is in contrast to observations during the May 11-12 period, which indicated that only a few higher clouds were present. The rate at which the insoluble volume concentration increased was intermediate of that predicted for the two limiting SOA addition scenarios described above. The characteristics of, and explanation for, the aerosol evolution observed on May 19 were very similar to those for the May 16-17 period.

5. MULTI-COMPONENT PARTICLE MODEL

In order to predict the optical and activation properties of the aerosol, a multi-component particle model is employed. For this study, each particle is assumed to be a sphere consisting of a homogeneous mixture of organic carbon (OC), elemental carbon (EC), mineral dust, ammonium sulfate, and water, or some subset of these components. The rationale for including these specific aerosol species follows.

TDMA measurements made during the Aerosol IOP indicate that for dry diameters greater than 0.300 μm, non-hygroscopic particles were frequently present at sufficiently high concentrations to produce a discernable mode in the measured growth factor distributions. In contrast, such non-hygroscopic modes were rarely observed for particles having dry diameters between 0.100 and 0.300 μm (see Figure 3). The presence of this non-hygroscopic aerosol at only the largest submicron sizes suggests the influence of the leftmost tail of a supermicron mode consisting of dust particles. Therefore, the insoluble component of particles with dry diameters greater than 0.300 μm and G(85) values less than 1.1 is assumed to be mineral dust.

For all other particles, the insoluble component is assumed to be a combination of OC and EC. Because size-resolved composition data were unavailable, it was assumed that the OC/EC mass ratio was independent of particle size. For this study, the OC/EC mass ratio is determined by iterating until the single-scattering albedo (SSA) predicted in the manner described later in Section 5.2.1 using the DMA/TDMA compositionally-resolved size distribution agrees with that calculated using NOAA CMDL scattering and absorption measurements made with a nephelometer and a light

absorption photometer, respectively. This approach of adjusting the relative amount of EC in the aerosol based on measured absorption provides an alternative to the oversimplified method of assuming a constant OC/EC ratio. Available OC and EC mass concentrations determined through thermoevolution analysis are sensitive to the cutoff temperature defining the transition from OC to EC. Furthermore, this approach minimizes the impact of the assumed mixing scenario of EC and other components since the concentration of EC determined in this way will be inversely related to its mass absorption efficiency. Hence, the unrealistically-high mass absorption efficiency that results from the assumption made here that particles are homogeneous spheres simply results in a decreased EC concentration. Although this bias would impact direct comparison of the predicted and measured EC mass concentration, it is expected to have only a minimal impact on the resulting scattering phase function, which is the only optical quantity derived using these data that is used in the comparisons described in Section 5.2.

The assumptions regarding the soluble component of the aerosol are partly based on compositional analysis of aerosol samples collected during the springtime of 2000 and 2001 at the ARM SGP site. Those data indicate that nitrate contributed just over 1% of the total submicron aerosol mass while sulfate contributed 30% [*Iziomon and Lohmann*, 2003]. Since the hygroscopic and activation properties of several sulfate-based inorganic aerosols are quite similar, the computations described here will be only slightly sensitive to the choice of inorganic aerosol. *Dusek et al*. [2003] showed that the relative difference in critical supersaturation between a pure ammonium sulfate particle

and a pure ammonium bisulfate particle of the same size is less than 3%. With respect to the degree of neutralization of aerosol-phase sulfate, measurements made at the ARM SGP site with a Particle-Into-Liquid Sampler [PILS, *Weber et al.*, 2001] operated by researchers from Brookhaven National Laboratory indicate that aerosol-phase sulfate was present in the fully-neutralized form of ammonium sulfate on approximately 75% of the days during the Aerosol IOP on which those measurements were made (Y.-N. Lee, manuscript in preparation, 2005). Ammonium sulfate is therefore assumed to comprise the soluble component of the aerosol.

5.1. Combining DMA and TDMA Data

Figure 14 illustrates the approach used to combine a DMA size distribution and the subsequent TDMA size-resolved hygroscopicity measurements. A size distribution as measured at the beginning of a hypothetical measurement sequence is depicted on the near face of the rectangular prism shown in Figure 14. Whereas eight G(85) distributions were measured during each sequence, only three are shown in Figure 14 to improve clarity. Using the G(85) distributions measured at each of the eight fixed dry diameters, G(85) distributions are interpolated for each of the 75 size bins in the measured submicron aerosol size distribution. The fraction of particles of a specific dry diameter and G(85), $T_{G(85)}$, can be determined through the expression:

$$T_{G(85)} = \frac{\frac{dn_{G(85)}}{d\log G(85)} \times \Delta \log G(85)}{\sum_{G(85)} n_{G(85)}} = \frac{\Delta n_{G(85)}}{\sum_{G(85)} n_{G(85)}}, \qquad (1)$$

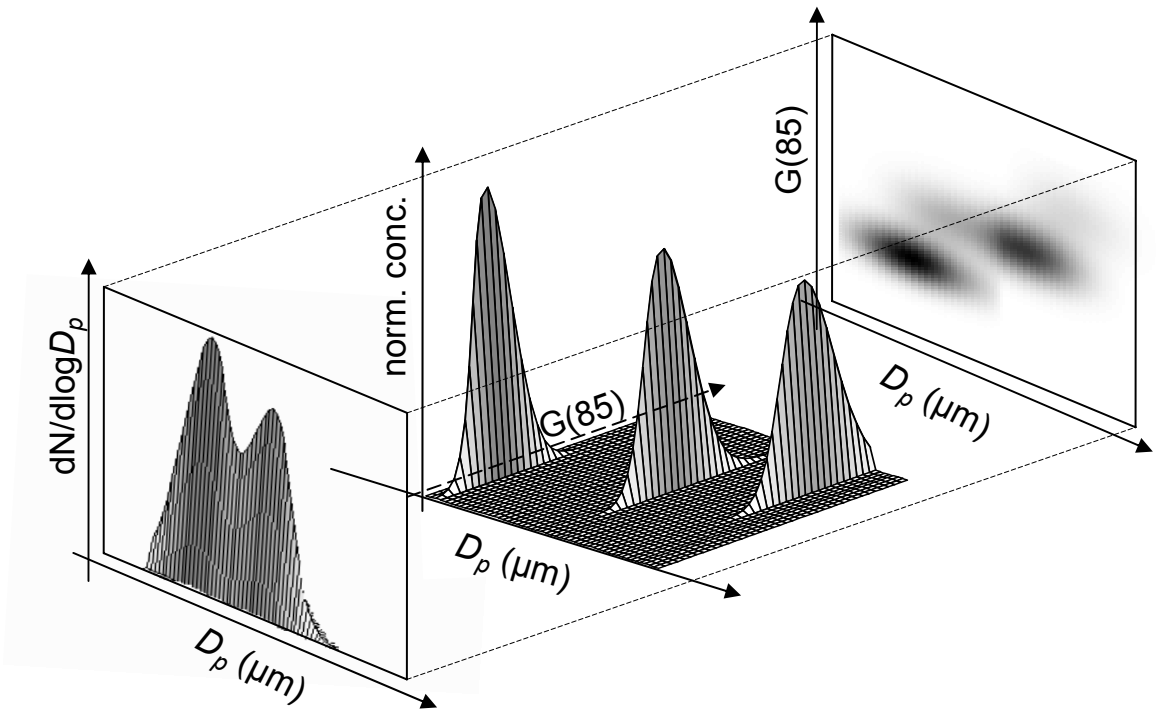

Figure 14. Conceptual model showing how the concentration of particles as a function of dry diameter and TDMA hygroscopic growth factor is derived. A sample dry size distribution is shown at the front of the box. Three sample TDMA hygroscopic growth factor distributions, showing non-hygroscopic particles at 0.012 μm, moderately hygroscopic particles at 0.100 μm, and hygroscopic particles at 0.450 μm, are plotted in the middle of the box. The combination of the size distributions and TDMA hygroscopic growth factor distributions, interpolated throughout the entire dry diameter range, is projected onto the back of the box.

where $\Delta n_{G(85)}$ is the concentration of particles exhibiting a G(85) within that particular growth factor bin. Therefore, the concentration of particles in a bin centered at a specified dry diameter and growth factor, $\Delta N_{Dp^*,G(85)}$, is simply the product of the corresponding values in the size and hygroscopic growth factor distributions:

$$\Delta N_{D_p^*,G(85)} = T_{G(85)} \times \Delta N_{D_p^*}, \tag{2}$$

where ΔN_{Dp^*} is the concentration of particles in the size bin centered at dry diameter D_p^*. An example of the resulting matrix of number concentrations as a function of both dry diameter and G(85) is projected onto the back of the rectangular prism in Figure 14.

For a hydrated particle of a given size, the mass fraction of solute in aqueous solution, x_s, is needed to calculate its optical and activation properties. The volume of the particle at 85% RH V_{85} and its dry volume V_{dry} are related to the volume of insoluble material V_i, the volume of soluble material V_s, and the volume of aqueous solution V_{as}:

$$V_{85} = \frac{\pi}{6} D_{p(85)}{}^3 = V_i + V_{as} \tag{3}$$

$$V_{dry} = \frac{\pi}{6} D_p^{*\,3} = V_i + V_s \tag{4}$$

An empirical relationship for the density of an aqueous ammonium sulfate solution, ρ_{as}, is provided in the work of *Tang and Munkelwitz* [1994]:

$$\rho_{as} = 0.9971 + \sum_i A_i x_s{}^i = \rho_{as}(x_s), \tag{5}$$

where the coefficients A_1, A_2, and A_3 are $5.92\text{H}10^{-3}$, $-5.036\text{H}10^{-6}$, and $1.024\text{H}10^{-8}$, respectively. Subtracting (4) from (3) and performing some manipulation yields:

$$\frac{m_s}{x_s \rho_{as}(x_s)} - \frac{m_s}{\rho_s} = \frac{\pi}{6}\left(D_{p(85)}{}^3 - D_p^{*\,3}\right), \tag{6}$$

where m_s and ρ_s represent the mass and density of soluble material, respectively.

The diameter of a particle at 85% RH, $D_{p(85)}$, which is simply the product of its dry diameter and its G(85), is related to its composition and water activity, a_w, by Köhler Theory:

$$\ln(0.85) = \frac{4M_w\sigma_{as}}{RT\rho_w D_{p(85)}} + \ln(a_w), \tag{7}$$

where T denotes temperature, σ_{as} is the surface tension of aqueous solution, and M_w and ρ_w are the molecular weight and density of water, respectively [see, e.g., *Seinfeld and Pandis*, 1998]. The surface tension of the aqueous solution is a function of the surface tension of water, which is dependent on temperature, and the molarity of the aqueous solution, which is dependent on both the mass fraction of solute in solution and the density of the aqueous solution:

$$\sigma_{as} = \sigma_w(T) + \frac{0.000002 x_s \rho_{as}(x_s)}{M_s} = \sigma_{as}(x_s) \ , \tag{8}$$

into which (5) can be substituted for the density of aqueous solution [see, e.g., *Seinfeld and Pandis*, 1998]. The empirical relationship for the water activity as provided in the work of *Tang and Munkelwitz* [1994] is:

$$a_w = 1.0 + \sum_i C_i x_s^{\ i} = a_w(x_s), \tag{9}$$

where the coefficients C_1, C_2, C_3, and C_4 are -2.715H10^{-3}, 3.113H10^{-5}, -2.336H10^{-6}, and 1.412H10^{-8}, respectively. The effect of any insoluble material within a particle on its water activity is assumed to be negligible and is therefore neglected. Accounting for the dependence of the density and water activity of aqueous solution on the solute mass fraction and manipulating, (7) becomes:

$$0.85 = a_w(x_s)\exp\left[\frac{4M_w\sigma_{as}(x_s)}{RT\rho_w D_{p(85)}}\right] \tag{10}$$

The mass fraction of solute in aqueous solution, x_s, is iterated until both (6) and (10) are satisfied. The soluble mass fraction of the population of particles represented by each of the elements of the number concentration matrix, $\Delta N_{Dp^*,G(85)}$, is computed using this approach. The refractive index and critical supersaturation of the particles represented

by each element are then calculated in the manner described below and used to determine the optical properties and CCN spectra of the aerosol.

5.2. Humidity-Dependent Optical Properties

5.2.1. Computation of Scattering

The calculated mass of ammonium sulfate within each particle is used to compute the refractive index of the aqueous ammonium sulfate solution using the method described in the work of *Tang and Munkelwitz* [1994]. A representative refractive index for the multi-component particle is computed by adding the volume-weighted refractive indices of the crystalline ammonium sulfate or aqueous ammonium sulfate solution, OC, EC, and mineral dust [*Kerker*, 1969]. The refractive indices of OC [*Larson et al*., 1988], EC [*Ouimette and Flagan*, 1982], mineral dust [*Mishchenko et al*., 1997], and crystalline ammonium sulfate [*Tang*, 1996] used for this analysis are listed in Table 1. Though the refractive index is dependent upon the wavelength of incident radiation, the real component of the refractive index varies little across the visible light spectrum. Since the primary analysis presented here concerns aerosol scattering, for this study the refractive indices listed in Table 1 are assumed to be invariant with wavelength.

Figure 15 shows the real and imaginary components of the refractive index of such a multi-component aerosol as a function of dry diameter and G(85) for an OC/EC ratio of 6.0. The discontinuities observed in Figure 15 at dry diameters greater than 0.300 μm and G(85) values less than 1.1 in each plot reflect the transition in the assumption of the insoluble composition from OC and EC to mineral dust. Figure 15 shows that the refractive index is sensitive to composition while it is mostly insensitive

Table 1. Refractive indices of each component used in modeling the aerosol optical properties based on DMA size and TDMA hygroscopic growth information.

Aerosol component	Real	Imaginary
Organic carbon (OC)[a]	1.55	0.0
Elemental carbon (EC)[b]	1.96	0.66
Mineral dust[c]	1.53	0.0005
Ammonium sulfate[d]	1.53	0.0

[a]Larson et al. [1988]

[b]Ouimette and Flagan [1982]

[c]Mishchenko et al. [1997]

[d]Tang [1996]

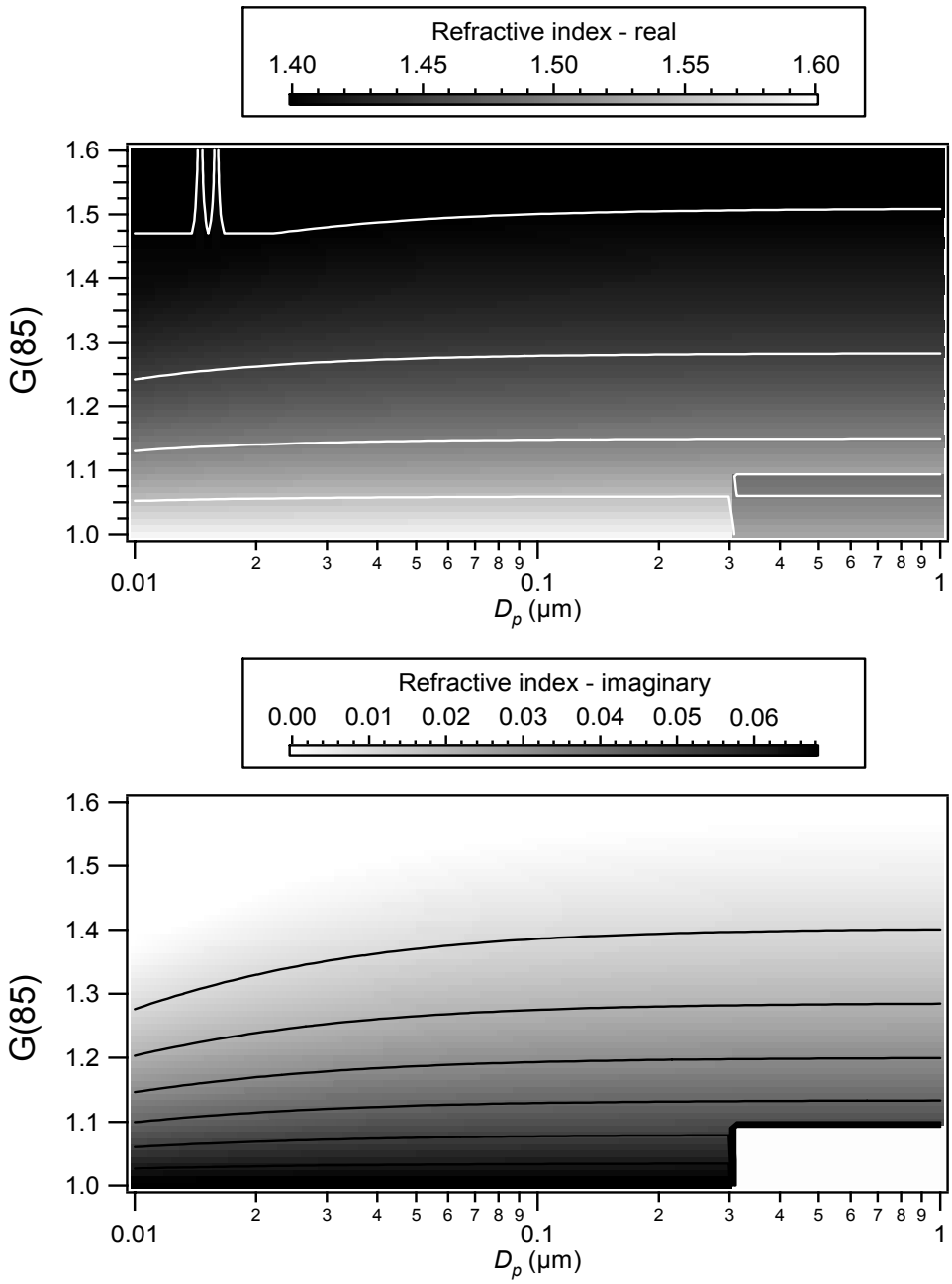

Figure 15. Modeled real and imaginary components of the refractive index of a homogeneous spherical particle as a function of dry diameter and TDMA hygroscopic growth factor. For these calculations, the soluble component is assumed to consist of ammonium sulfate $(NH_4)_2SO_4$, the insoluble component of particles larger than 0.300 μm and with growth factors less than 1.1 is assumed to consist of mineral dust, and the OC/EC ratio is 6.0.

to particle size. The slight size dependence reflects the increased soluble fraction needed to offset the influence of the Kelvin effect, which increases in magnitude with decreasing particle size. Figure 16 contains plots showing the difference between each component of the refractive index for aerosol with an OC/EC ratio of 6.0 and aerosol with an OC/EC ratio of 36.0. These ratios represent the extremes computed using the optically-based iterative procedure described above. Since particles with dry diameters greater than 0.300 μm and G(85) values less than 1.1 are assumed to be void of OC and EC, neither the real nor imaginary component of the refractive index for such large, non-hygroscopic particles shows variability based on changes in the assumed OC/EC ratio.

Scattering and absorption efficiencies, represented respectively by $Q_{sca}[D_p^*,\mathrm{G(RH)}]$ and $Q_{abs}[D_p^*,\mathrm{G(RH)}]$, are calculated for each particle size and hygroscopicity pair through a Mie light scattering model [*Bohren and Huffman*, 1983]. Computations of scattering based on the DMA/TDMA measurements were made under the assumptions that the aerosol was in equilibrium with the RH concurrently measured within the AOS, which is depicted in Figure 17a, and that the aerosol followed the crystallization leg of the hygroscopicity hysteresis loop of ammonium sulfate described in the work of *Tang and Munkelwitz* [1994]. Using the mass fraction of solute x_s computed by combining the DMA and TDMA data as described in Section 5.1, the growth factor of a particle at any RH is computed:

$$G(RH) = \frac{4M_w\sigma_{as}(x_s)}{(D_p^*)RT\rho_w\left[\ln\left(\frac{RH(\%)}{100}\right) - \ln(a_w(x_s))\right]} \tag{11}$$

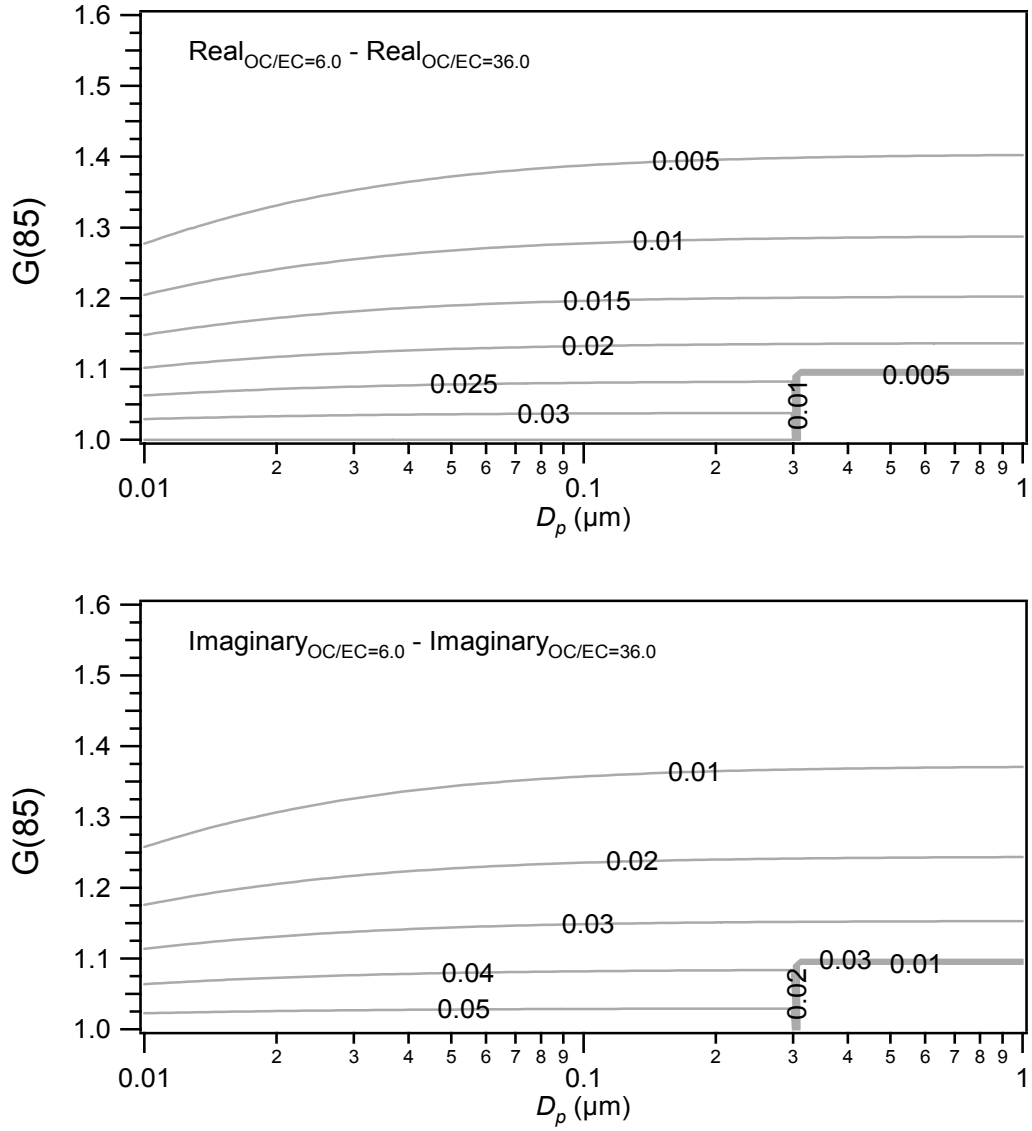

Figure 16. The differences in the modeled real and imaginary components of the refractive index as a function of dry diameter and TDMA hygroscopic growth factor introduced by varying the OC/EC ratio. The graphs were created by subtracting the refractive index computed using an OC/EC ratio of 36.0 from that calculated using an OC/EC ratio of 6.0.

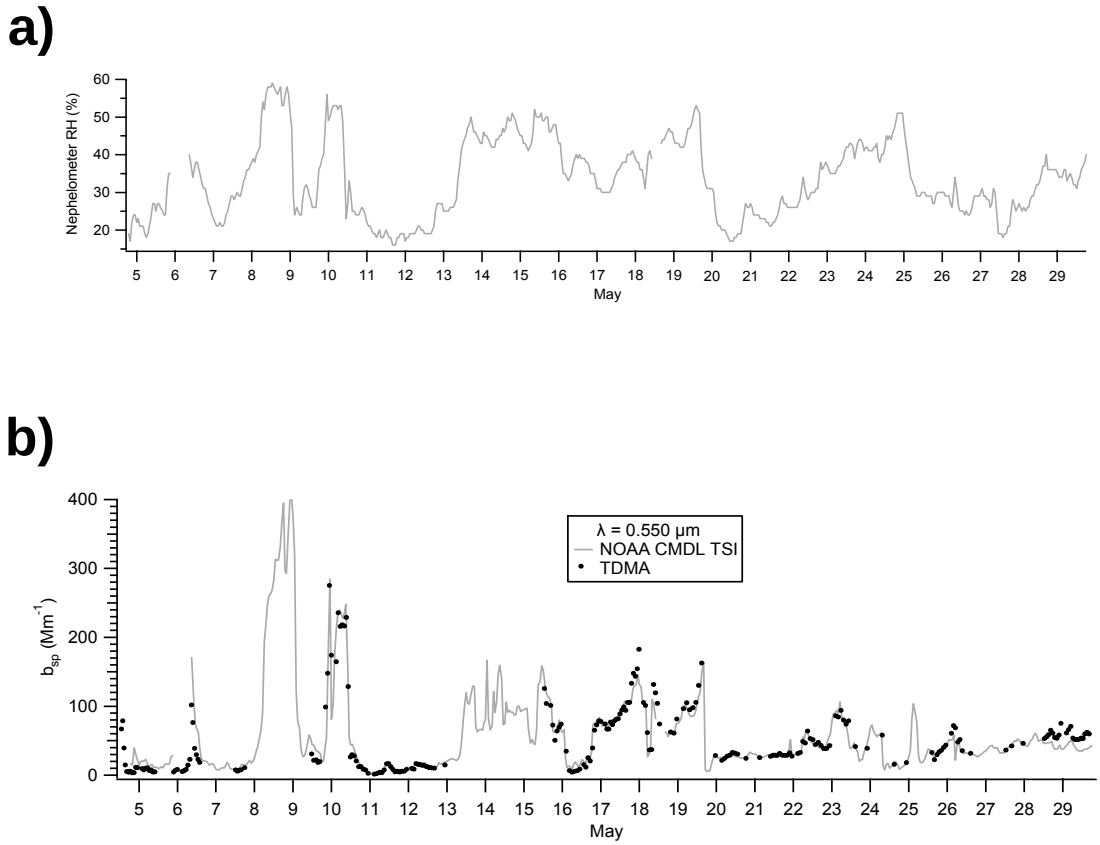

Figure 17. The RH measured within the nephelometer is depicted (a) and was incorporated in the scattering computations with the assumption that the hygroscopic growth of the aerosol followed the efflorescence leg of the hysteresis loop. Also depicted (b) is the ambient submicron aerosol scattering coefficient of green visible light (λ=0.550 µm) measured by NOAA CMDL during the Aerosol IOP as well as that computed using DMA submicron aerosol size distributions whose composition is modeled based upon TDMA hygroscopic growth factor information.

The total scattering coefficient by an aerosol population at a given RH, b_{sp}(RH), is calculated by adding the scattering contributions of each dry diameter and hygroscopicity pair:

$$b_{sp}(RH) = \sum_{D_p^*} \sum_{G(RH)} \left(\Delta N_{D_p^*, G(RH)} \frac{\pi}{4} \left(G(RH) \times D_p^* \right)^2 Q_{sca}[D_p^*, G(RH)] \right) \qquad (12)$$

Figure 17b shows the total scattering coefficient of green light (λ=0.550 μm) by the submicron aerosol throughout the Aerosol IOP as measured by the AOS and as predicted by the Mie light scattering model with the multi-component aerosol inferred using DMA/TDMA measurements. Excellent agreement is realized between the measured and predicted submicron scattering, yielding confidence in employing this multi-component aerosol model.

5.2.2. Computation of f(RH)

The ratio of the total scattering by an aerosol population at high RH to that by the same population at lower RH is termed the aerosol hygroscopic growth factor, *f*(RH). This is not the same as the TDMA hygroscopic growth factor, G(RH), which quantifies the change in particle diameter with a change in RH. The ammonium sulfate-dominated aerosol present at the ARM SGP site is expected to be crystalline at the lower RH, which was typically below 30%.

The *f*(RH) is predicted using DMA/TDMA data by taking the ratio of the total scattering computed at the high and low relative humidities measured concurrently within the humidograph. Measurements of *f*(RH) are made every minute during the

hour-long RH scan. The DMA size distribution and TDMA G(85) distributions are assumed to be constant during each DMA/TDMA measurement sequence. Because the extensive properties of an aerosol are expected to vary more rapidly than the intensive properties, the representative time selected for each DMA/TDMA measurement sequence is that corresponding to the time at which the size distribution is measured rather than the midpoint of the overall sequence. Comparisons were made between the predicted f(RH) values based on that DMA/TDMA measurement sequence and those measured during the hour-long RH scan in the humidograph that spanned the DMA/TDMA sequence time.

Each humidograph measurement yields a single value of f(RH). If the higher RH considered falls between the crystallization and deliquescence relative humidities of the aerosol, the predictions based on the measured size distributions and size-resolved hygroscopicity yield a range bounded by a minimum of 1.0 corresponding to an assumed crystalline aerosol and a maximum for an assumed metastable aerosol. Since the soluble component of the multi-component aerosol modeled in this study consists of ammonium sulfate, the crystallization and deliquescence relative humidities of the aerosol are approximately 39% and 80%, respectively [*Tang and Munkelwitz*, 1994]. The size-dependence of these quantities over the size range of optically-relevant aerosols is negligible [*Tang and Munkelwitz*, 1994]. Though the crystallization and deliquescence relative humidities have both been shown to be lower in mixed organic-ammonium sulfate particles than in pure ammonium sulfate particles [*Brooks et al*., 2002; *Pant et al*.,

2004; *Parsons et al*., 2004], these effects are not included here due to their dependence on the specific composition of the organic constituent.

5.2.3. Analysis of f(RH)

While *f*(RH) is typically described as the ratio of scattering at 85% RH to that at 40% RH, the following analysis contains comparisons at all measured relative humidities, in part due to the uncharacteristically low upper RH of ~75% attained in the wet nephelometer. Before May 19, the measured size distributions were limited to particles with dry diameters less than 0.750 μm, while beginning on May 19 the size distributions included particles with dry diameters up to 1.000 μm. The contribution of particles with dry diameters between 0.750 and 1.000 μm to the overall scattering coefficient would result in a bias when comparing with the direct measurements, which included all submicron particles. Hence, for the following analysis of *f*(RH), only those measurements made on or after May 19 are considered.

Figure 18 contains time series from May 19-29 of humidograph *f*(RH) measured when the wet nephelometer RH was in the range of 45-50% (a) and 70-75% (b). Only those measurements made when simultaneous DMA/TDMA measurements are available for comparison are shown in Figure 18. Also shown in Figure 18 are the ranges of *f*(RH) predicted using DMA/TDMA measurements, from 1.0 for crystalline aerosol to larger values for metastable aerosol. For the measurements shown in both Figure 18a and 19b, measured *f*(RH) values typically fall between the minimum and maximum predicted values, though the measurements more frequently approach the maximum predicted

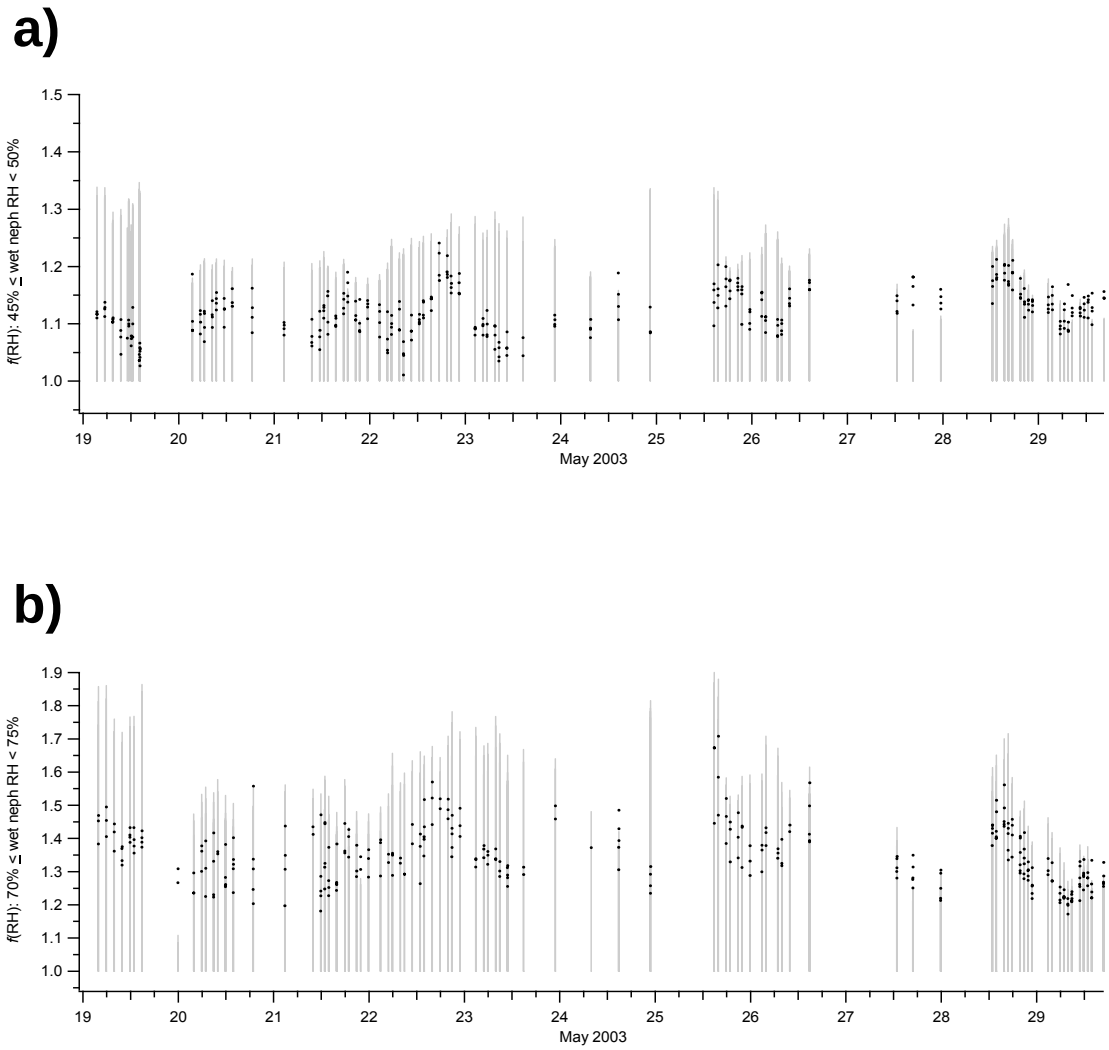

Figure 18. Comparison of hygroscopic growth factor *f*(RH) measured by NOAA CMDL with the range of *f*(RH) predicted using the DMA/TDMA data when the wet nephelometer RH was from 45% to 50% (a) and from 70% to 75% (b). The range of *f*(RH) predicted is bound at the low end by aerosol in the crystalline state whose hygroscopic growth follows the deliquescence leg of the hysteresis loop and at the high end by aerosol in the metastable state whose hygroscopic growth follows the efflorescence leg of the hysteresis loop.

f(RH) than the minimum. This suggests that some hygroscopic growth with respect to dry conditions is realized at intermediate values of RH, indicating that at least a subset of the particles remained aqueous.

To calculate the proximity P_f(RH) of the measured *f*(RH) to either the minimum or maximum predicted *f*(RH), the following relationship was employed:

$$P_f(RH) = \frac{f(RH)_{NOAA} - f(RH)_{TDMA,cry}}{f(RH)_{TDMA,meta} - f(RH)_{TDMA,cry}} = \frac{f(RH)_{NOAA} - 1.0}{f(RH)_{TDMA,meta} - 1.0} \quad (13)$$

A value of 0.0 indicates that the measured *f*(RH) agrees perfectly with the predicted *f*(RH) for crystalline aerosol, while a value of 1.0 indicates that the measured *f*(RH) agrees perfectly with the predicted *f*(RH) for metastable aerosol. Figure 19 shows box plots of the proximity P_f(RH) at intervals of 5% RH. Figure 19 indicates that predictions of *f*(RH) using DMA/TDMA data assuming metastable aerosol yield better agreement than those made for crystalline aerosol, though the assumption that all particles are aqueous leads to an overprediction of *f*(RH).

The ratio of the *f*(RH) predicted assuming metastable aerosol to the measured *f*(RH) is shown in box plots at intervals of 2% RH in Figure 20a. Figure 20b contains a histogram of the number of humidograph and DMA/TDMA measurement pairs considered within each RH interval. From May 19-29, 5908 measurement pairs are identified. For RH values less than 40% RH, the predicted *f*(RH) is consistently lower than that measured. No hygroscopic growth, and consequently no enhancement in total scattering, is predicted below 39% RH since that marks the crystallization RH of ammonium sulfate and, therefore, of the multi-component aerosol modeled here. The

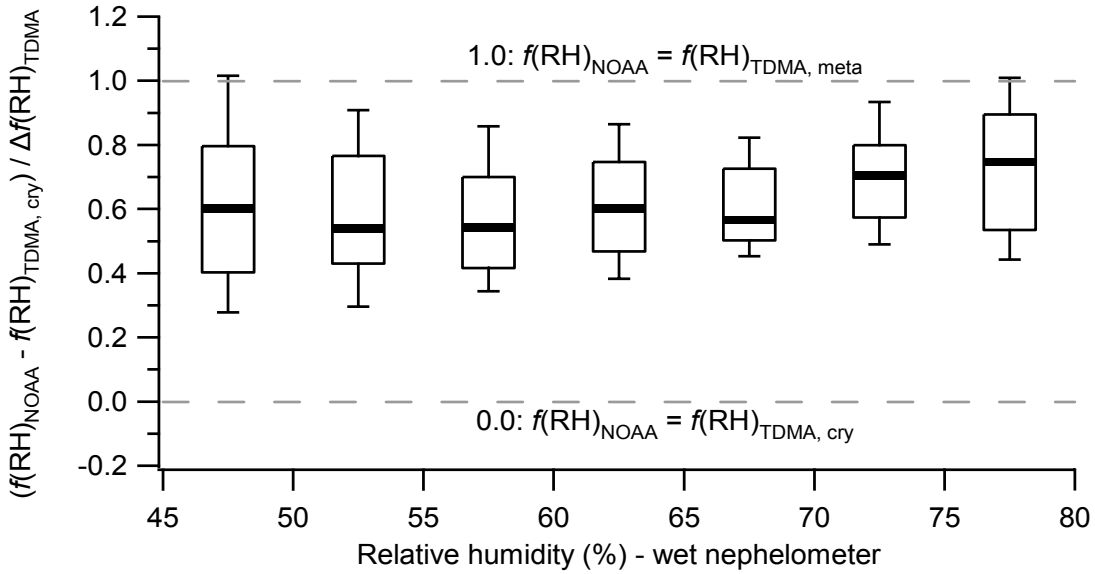

Figure 19. Box plots for RH intervals of 5% depicting the difference between the hygroscopic growth factor *f*(RH) measured by NOAA CMDL and that predicted using the DMA/TDMA data assuming aerosol in the crystalline state (deliquescence leg of the hysteresis loop). These differences were all normalized with the difference in *f*(RH) predicted assuming metastable aerosol with that predicted with crystalline aerosol. This allows for the ratio to equal 0.0 when the measured *f*(RH) agrees with the *f*(RH) predicted assuming crystalline aerosol and to equal 1.0 when it agrees with that predicted assuming metastable aerosol.

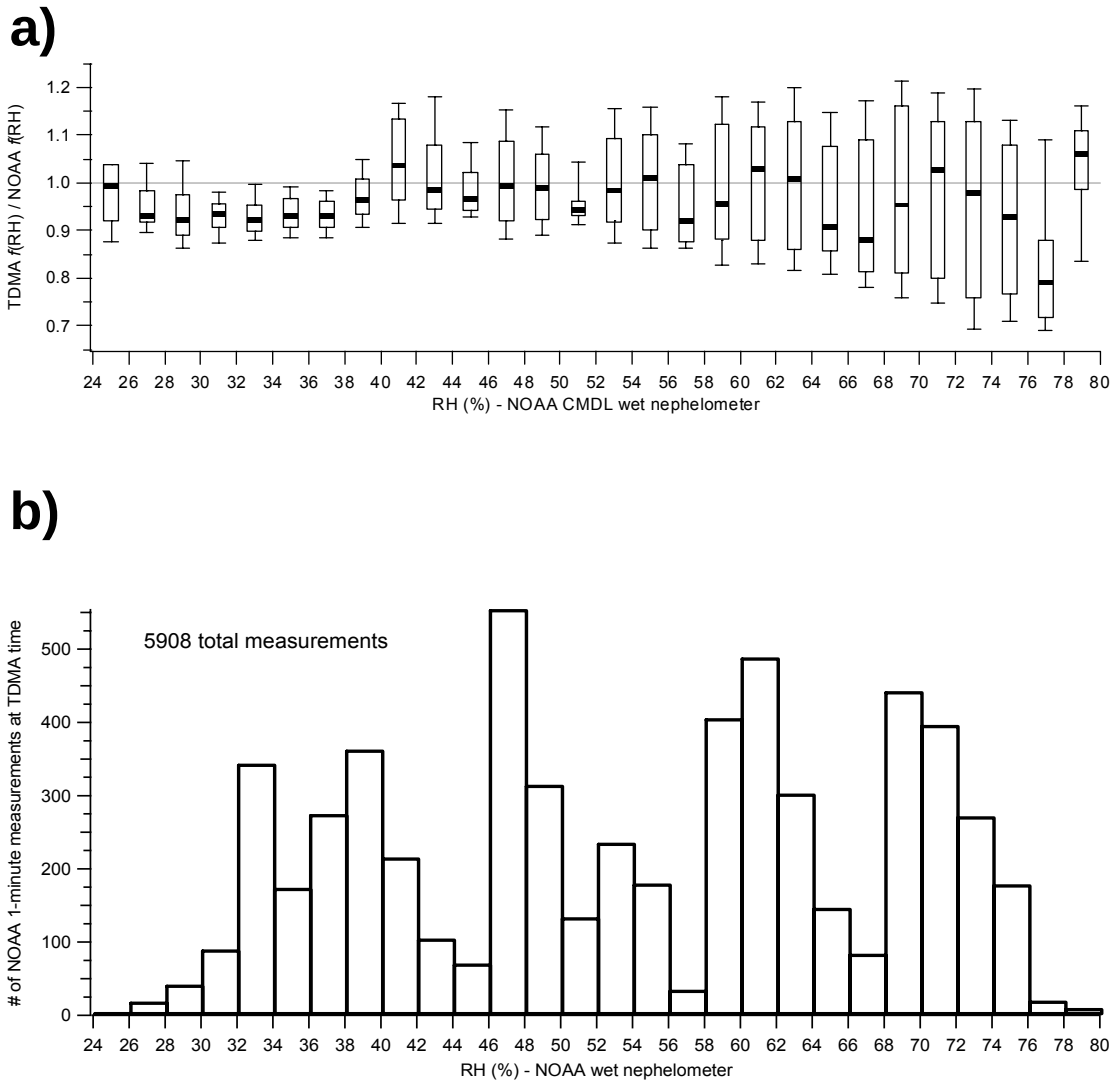

Figure 20. (a) Box plots at 2% RH intervals depicting the ratio of *f*(RH) predicted using DMA/TDMA data to that measured by the NOAA CMDL. The heavy line within each box marks the median value, the ends of the box mark the 25th and 75th percentiles, and the whisker caps mark the 10th and 90th percentiles. The horizontal line at 1.0 marks perfect agreement. The histogram (b) depicts the number of NOAA CMDL measurements (1-minute time resolution) as a function of the wet nephelometer RH that were paired with concurrent DMA/TDMA measurements.

model fails to capture the measured enhancement in scattering for RH values below 40%. This unpredicted enhancement could be due to hygroscopic growth of water-soluble organics at relative humidities below the crystallization RH of ammonium sulfate, or it could be due to the aforementioned depression in the crystallization RH observed in multi-component particles [*Brooks et al*., 2002; *Pant et al*., 2004; *Parsons et al*., 2004]. At RH above 40%, the predicted f(RH) is generally within $\pm$10% of the measured f(RH). The caps on the whiskers above each of the boxes in Figure 20a, marking the 90th percentile values, indicate that the largest overpredictions of f(RH) are mostly confined to 15-20% error. Those below each of the boxes in Figure 20a, marking the 10th percentile values, indicate that the f(RH) occasionally is increasingly underpredicted with increasing RH above ~65% RH. This suggests that under some circumstances, in addition to underestimating the enhanced scattering at high RH, the increase in the scattering enhancement with increasing RH may also be underestimated when employing this multi-component particle model.

5.3. Cloud-Nucleating Properties

5.3.1. Method of Derivation of CCN Spectra

DMA/TDMA data were analyzed to produce a matrix of soluble masses as a function of dry diameter and G(85) using the method of deriving the soluble mass within a particle described in Section 5.1. Solving equation (11) for the RH and replacing the empirically-calculated water activity with a mole fraction-based representation produces

a relationship between the supersaturation, *S*, and the size and composition of a thermodynamically-stable solution droplet:

$$S[D_p^*, G(RH)] = \frac{1}{\frac{M_w \nu}{M_s}\left(\frac{x_s}{1-x_s}\right)+1.0} \exp\left[\frac{4M_w\sigma_{as}(x_s)}{RT\rho_w\left(G(RH)\times D_p^*\right)}\right] - 1.0, \quad (14)$$

with assumed values of 3 for the van't Hoff factor, ν, and 132 g mol^{-1} for the molecular weight of solute, M_s. These assumed values correspond to their respective values for ammonium sulfate, which is assumed to comprise the soluble component of the aerosol. While the insoluble mass in each particle certainly influences the size of the particle, its effect on the water activity is uncertain, though this effect is likely negligible. Therefore, for these computations, the size of each particle includes the contribution from the insoluble mass, but the insoluble mass is assumed to have no effect on the water activity of the particle.

Equation (14) is used to construct a Köhler curve considering an array of droplet sizes for each dry diameter and G(85) pair. The ordinate of the highest point on this simulated Köhler curve represents the critical supersaturation for a particle of that dry diameter and hygroscopicity. This is done for every dry diameter and G(85) pair, yielding a matrix of predicted critical supersaturations based on dry diameter and hygroscopicity. A matrix of these predicted critical supersaturations created for the multi-component aerosol based on the computations described in Section 5.1 is shown in Figure 21. Because the predicted critical supersaturations range from 0.01-10.00%, the data in Figure 21 are contoured logarithmically. The sensitivity of the critical supersaturation of a particle to its dry diameter is evident in Figure 21.

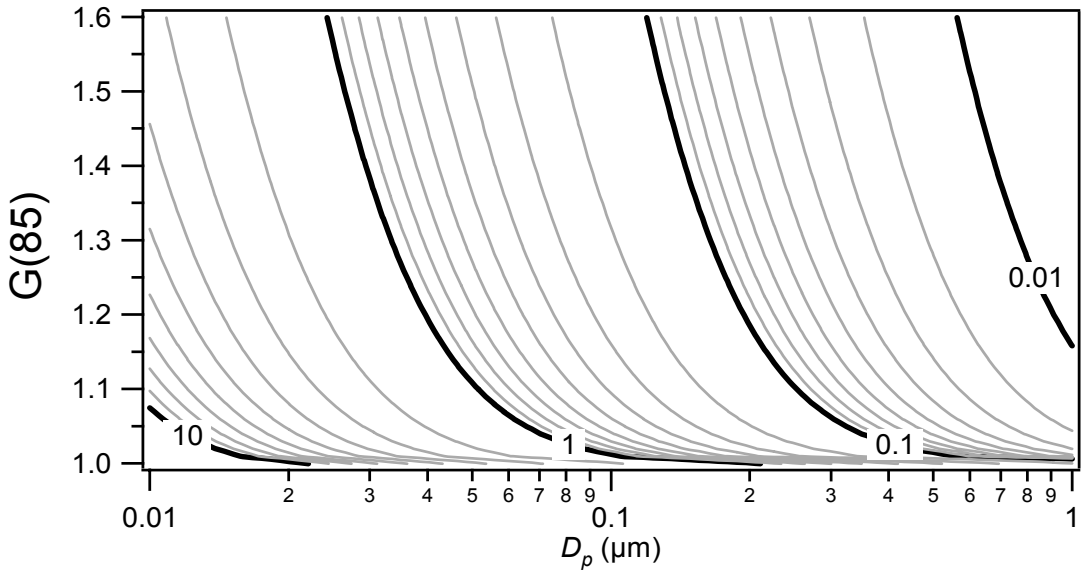

Figure 21. Contoured logarithmically are critical supersaturations (%) predicted using Köhler Theory, displayed as a function of dry diameter and TDMA hygroscopic growth factor. The particles are assumed to be homogeneous spheres whose compositions were determined using TDMA hygroscopic growth factor information.

Derivation of the cumulative CCN spectrum corresponding to each DMA/TDMA measurement sequence requires the matrix of number concentrations computed as a function of both dry diameter and G(RH), similar to the example shown in Figure 14. The number of activated particles at a given supersaturation is calculated by integrating the matrix of number concentrations above the respective critical supersaturation contour, similar to the contours depicted in Figure 21. The CCN spectrum is constructed by performing this integration over the entire range of supersaturations considered.

5.3.2. Derived versus Measured CCN Spectra

Figure 22 contains three pairs of measured and predicted CCN spectra from the Aerosol IOP. The first pair, from May 18, shows excellent agreement between predicted and measured CCN concentrations, though imprecise measurements of larger particles may have led to the overpredictions of CCN concentrations at the lowest supersaturations. The second spectrum, from May 25, shows good agreement across the entire range of supersaturations considered. The third spectrum, from May 28, shows excellent agreement at supersaturations up to 0.30%, but predicted CCN concentrations exceed those measured at higher supersaturations. This overprediction is possibly the result of coincidence errors within the Royco white light OPC, in which multiple droplets generate a single pulse, thereby lowering the measured CCN concentration.

Because of the sensitivity of the supersaturation distribution of an aerosol population to its size distribution, comparisons are made only for those spectra measured with the DRI CCN spectrometers within 2 minutes of the start time of the DMA/TDMA

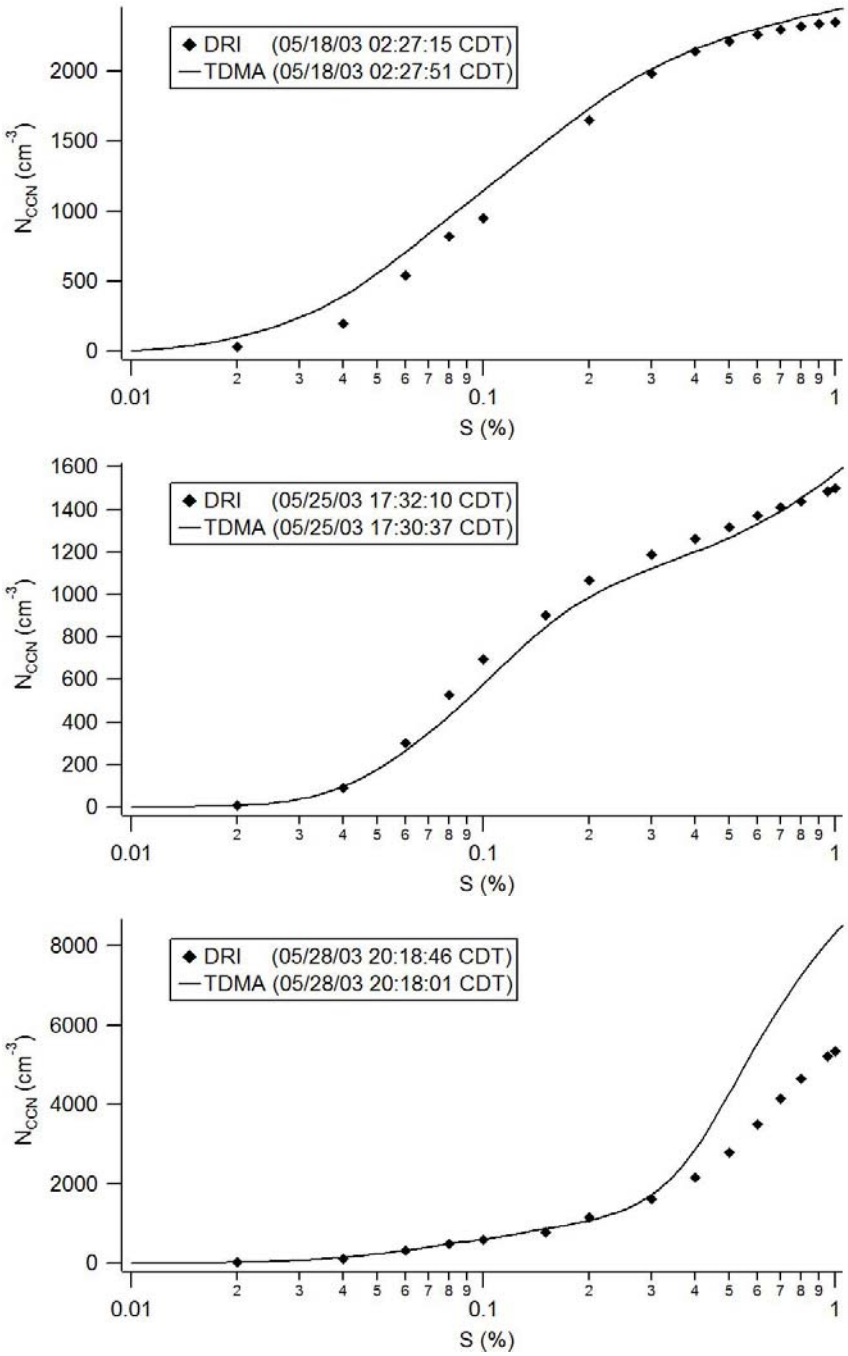

Figure 22. CCN spectra predicted using DMA/TDMA data overlaid with measurements of cumulative CCN concentrations at various supersaturations measured with the DRI CCN spectrometer. The spectra from May 18 and May 25 show good agreement at all supersaturations. The spectrum from May 28 shows excellent agreement except at higher supersaturations, where coincidence errors may be contributing to the discrepancy.

size distribution measurement. CCN spectra were directly measured within this 4-minute window during 137 of the 239 completed DMA/TDMA measurement sequences. Over these 137 DMA/TDMA measurement sequences, 1490 measurements were made at various supersaturations ranging from 0.02-1.05% for which cumulative CCN concentrations were predicted using the DMA/TDMA data. Figure 23 contains a scatter plot showing the cumulative number concentration of CCN at a given supersaturation as predicted using DMA/TDMA data versus that at the same supersaturation as measured with the DRI CCN spectrometers. The R^2 value for the linear regression is 0.86, and 57% of the predicted CCN concentrations are within 20% of those measured. Figure 23 is plotted with logarithmic axes because of the wide ranges of supersaturations and CCN concentrations considered. While CCN concentrations less than 10 cm^{-3} were both measured and predicted, they are not shown in Figure 23 since such occurrences were rare.

Figure 24 contains scatter plots of CCN concentrations predicted versus those measured at 16 supersaturations: 0.02, 0.04, 0.06, 0.08, 0.10, 0.15, 0.20, 0.25, 0.30, 0.40, 0.50, 0.60, 0.70, 0.80, 0.90, and 1.00%. The R^2 values for the linear regressions at these supersaturations, as well as the slopes and intercepts of the linear regressions, are listed in Table 2. The sample number-weighted mean R^2 value for the data shown in Figure 24 and listed in Table 2 is 0.74. For supersaturations of 0.02% and 0.04%, the predicted CCN concentrations are generally higher than those measured. Since CCN concentrations are small at such low supersaturations, any error in measurement or prediction is magnified. At CCN concentrations of over approximately 5000 cm^{-3},

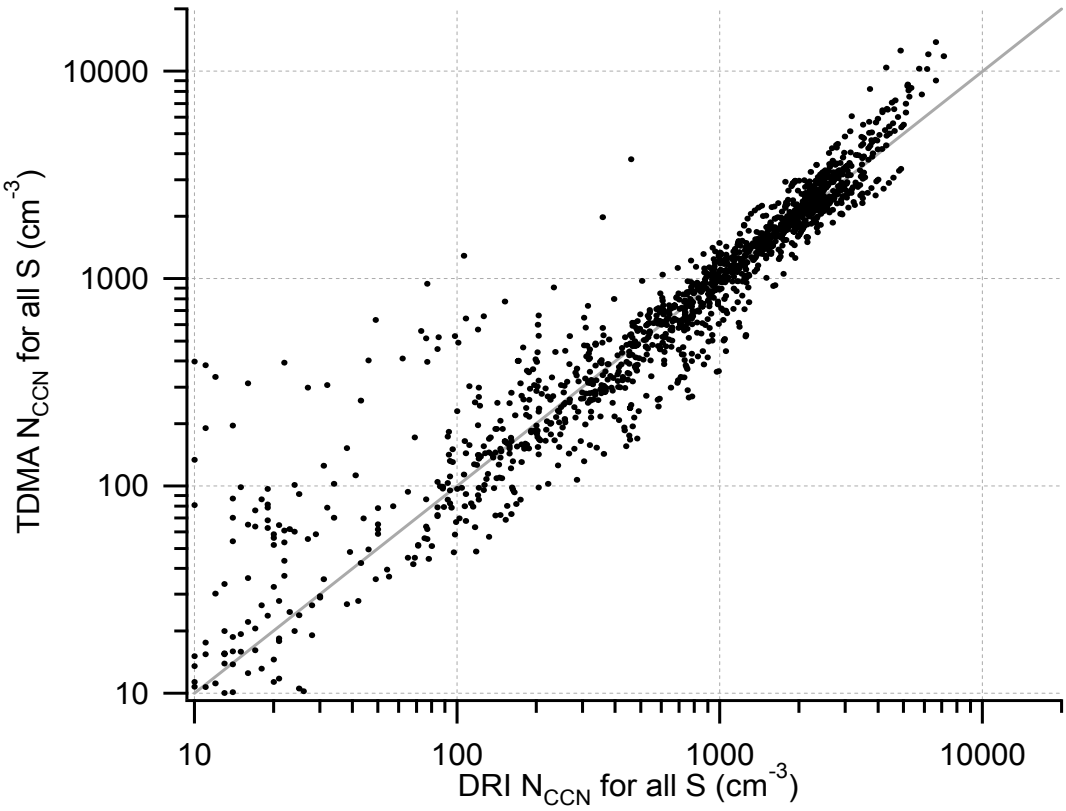

Figure 23. Scatter plot of cumulative CCN concentrations (cm^{-3}) predicted using DMA/TDMA data versus those measured with the DRI CCN spectrometer at all critical supersaturations measured within the DRI CCN spectrometer for the entire Aerosol IOP (1490 measurement pairs). The scales are logarithmic in order to display several orders of magnitude, and CCN concentrations less than 10 cm^{-3} are not shown in order to focus on larger orders of magnitude.

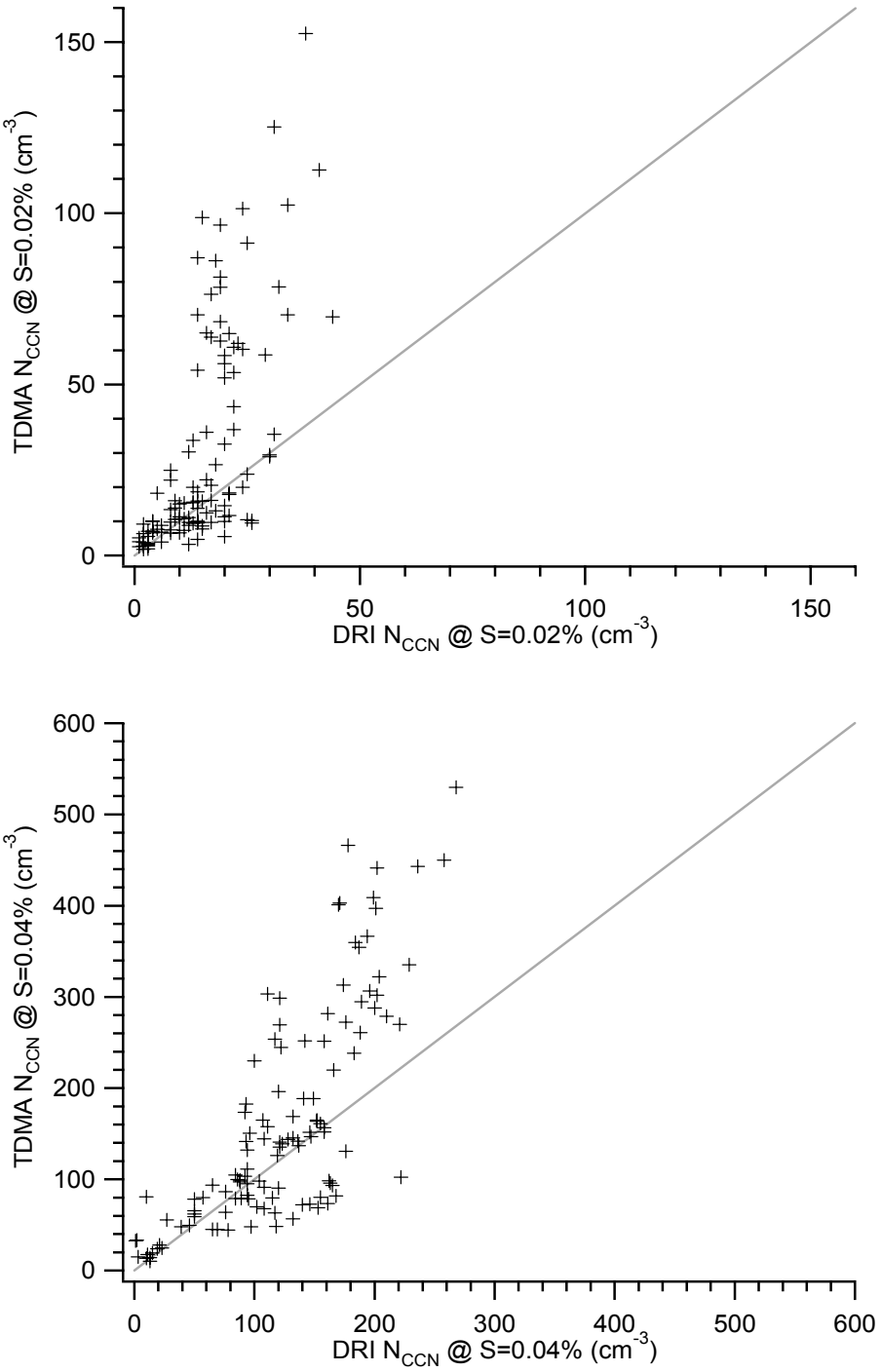

Figure 24. Scatter plots of cumulative CCN concentrations (cm^{-3}) predicted using DMA/TDMA data versus those measured with the DRI CCN spectrometer at a given S.

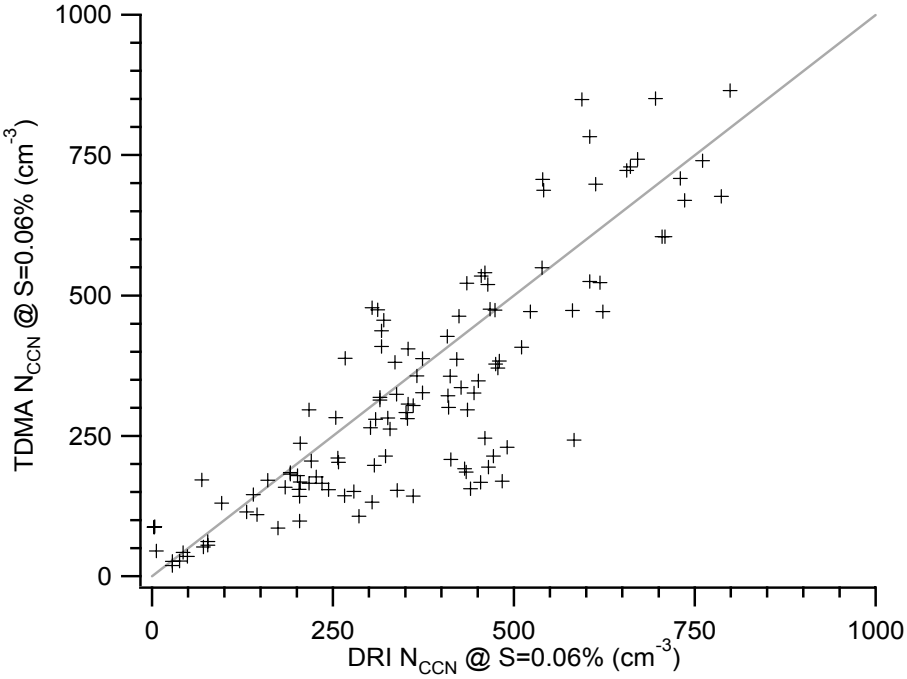

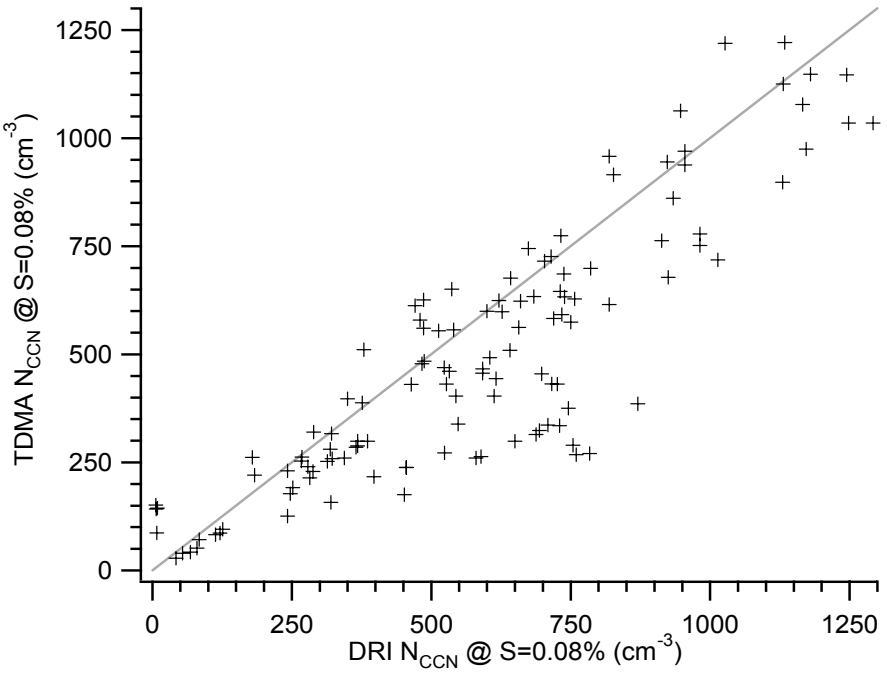

Figure 24 (continued).

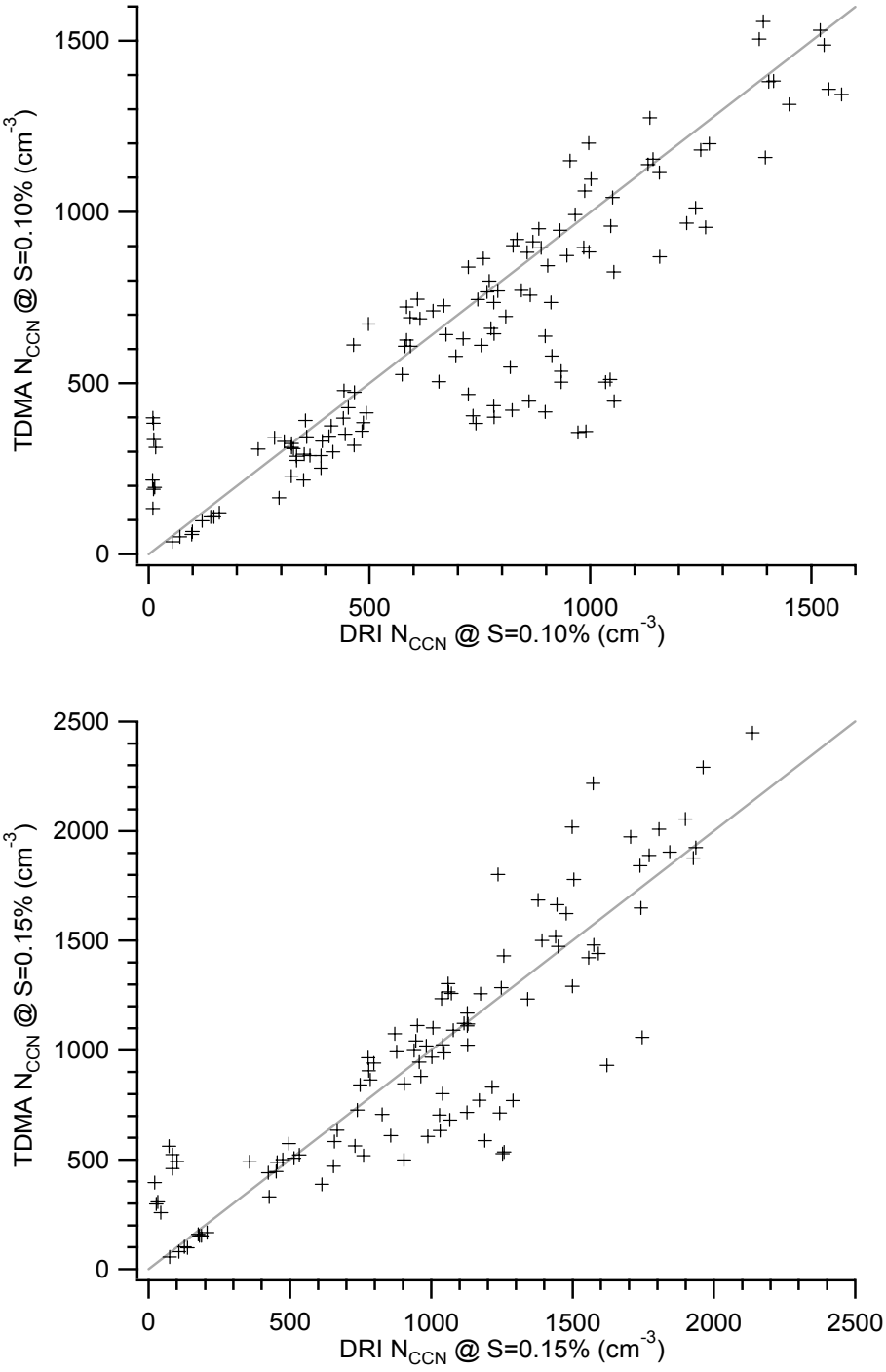

Figure 24 (continued).

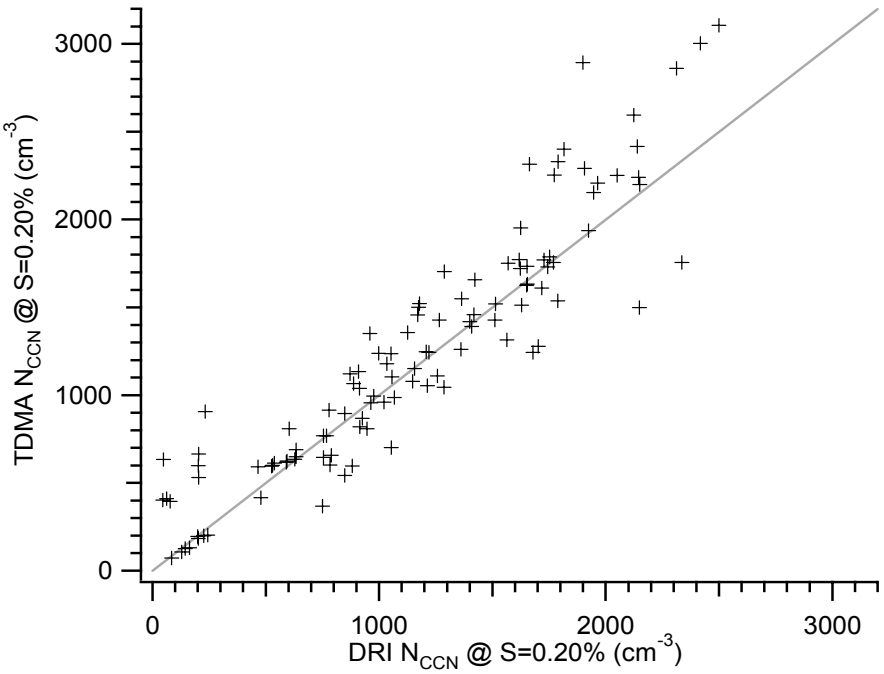

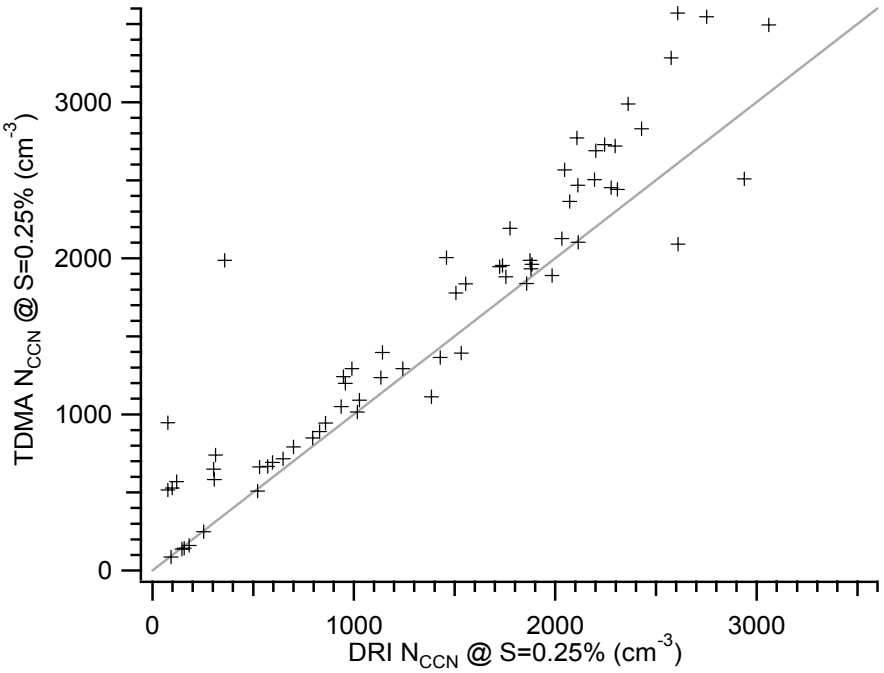

Figure 24 (continued).

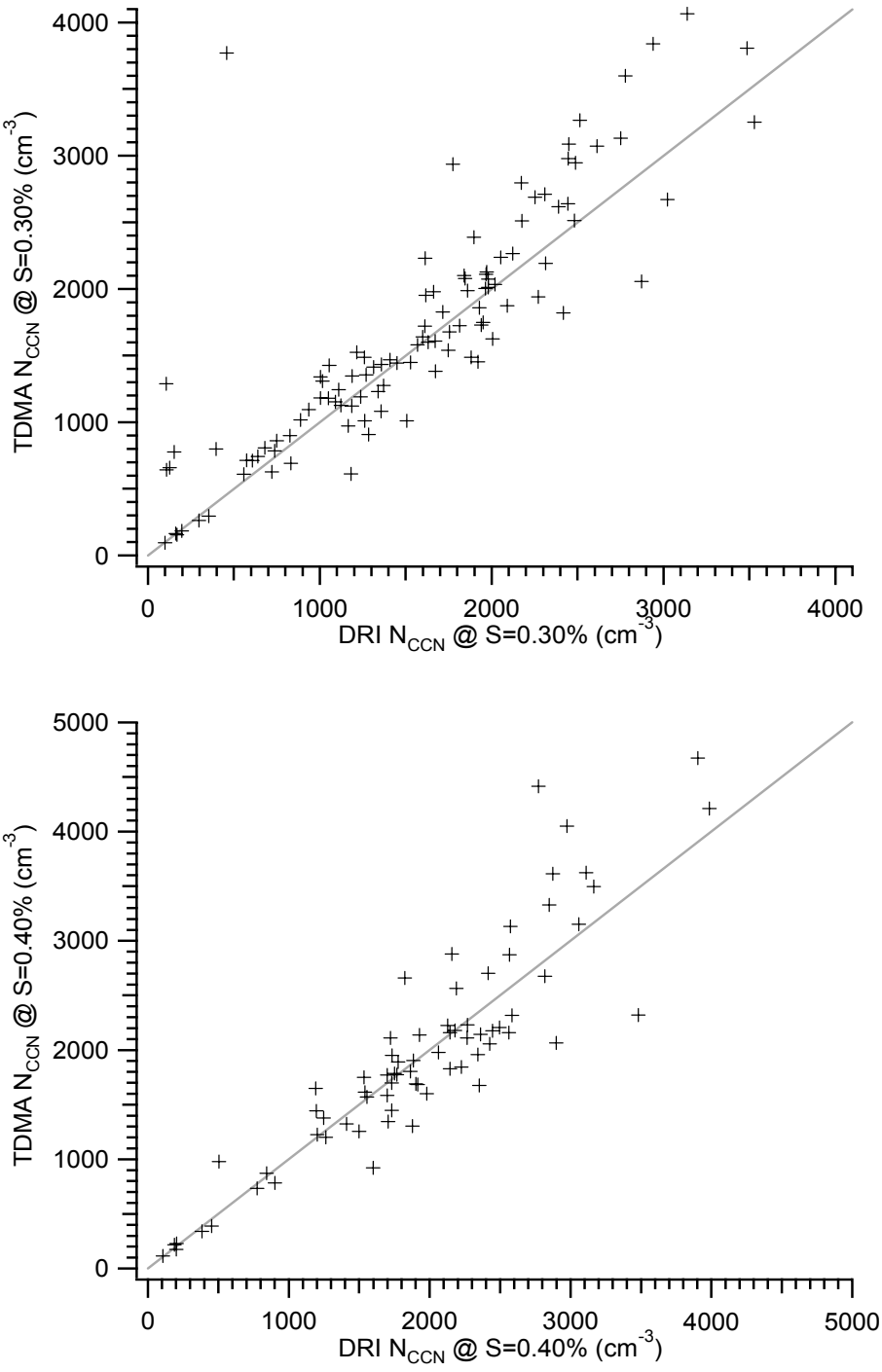

Figure 24 (continued).

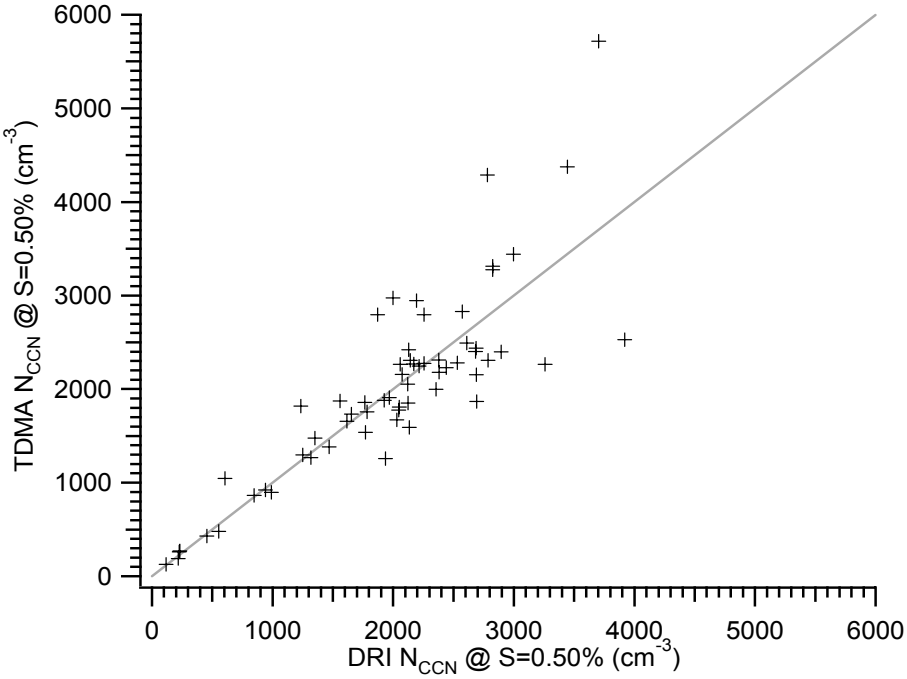

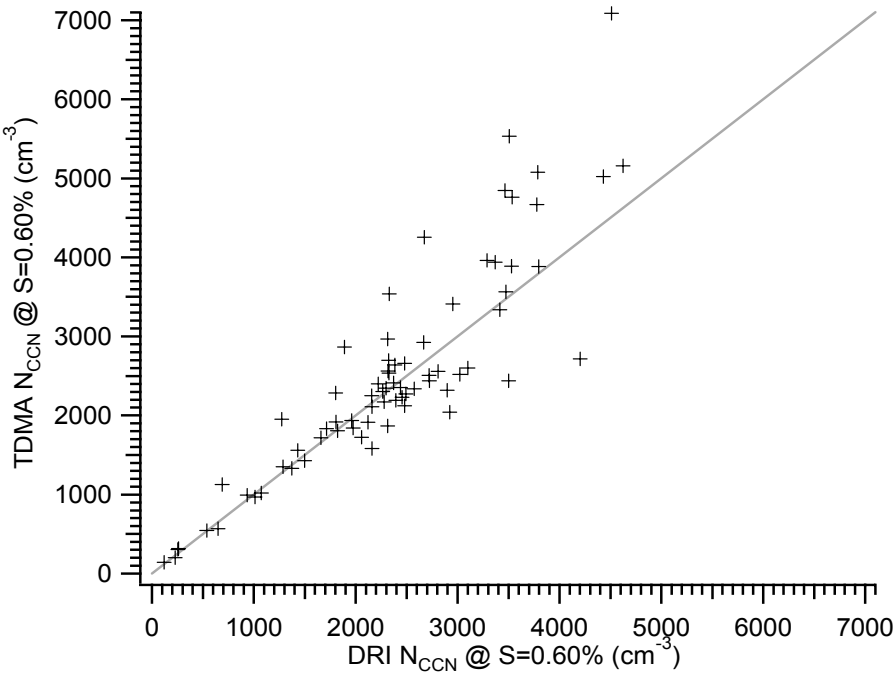

Figure 24 (continued).

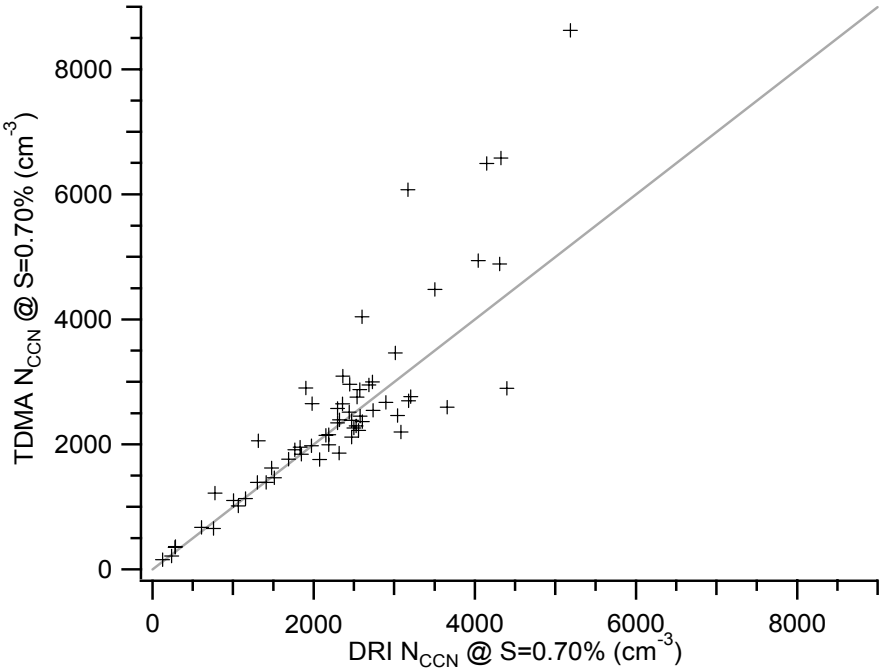

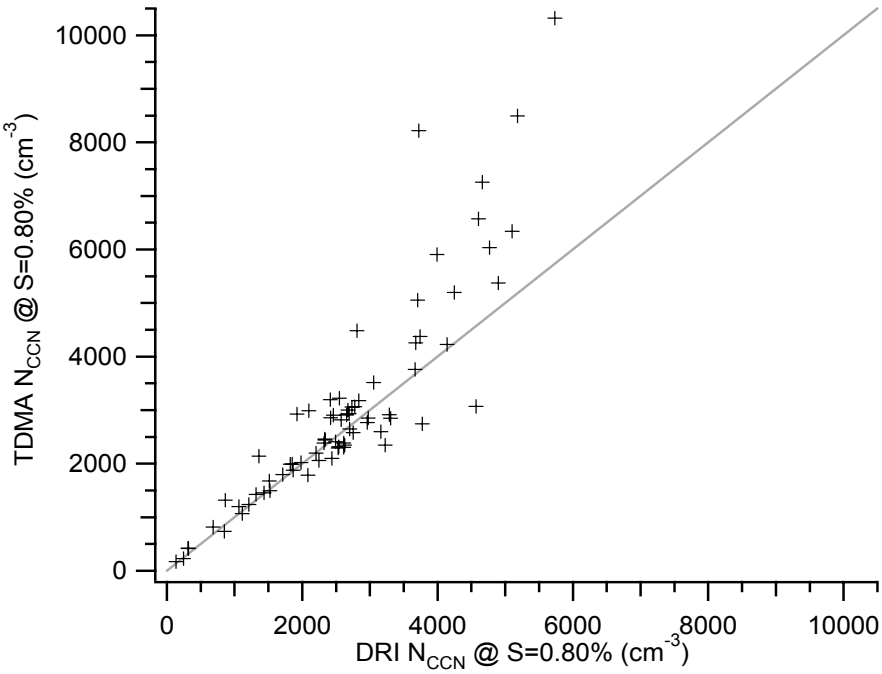

Figure 24 (continued).

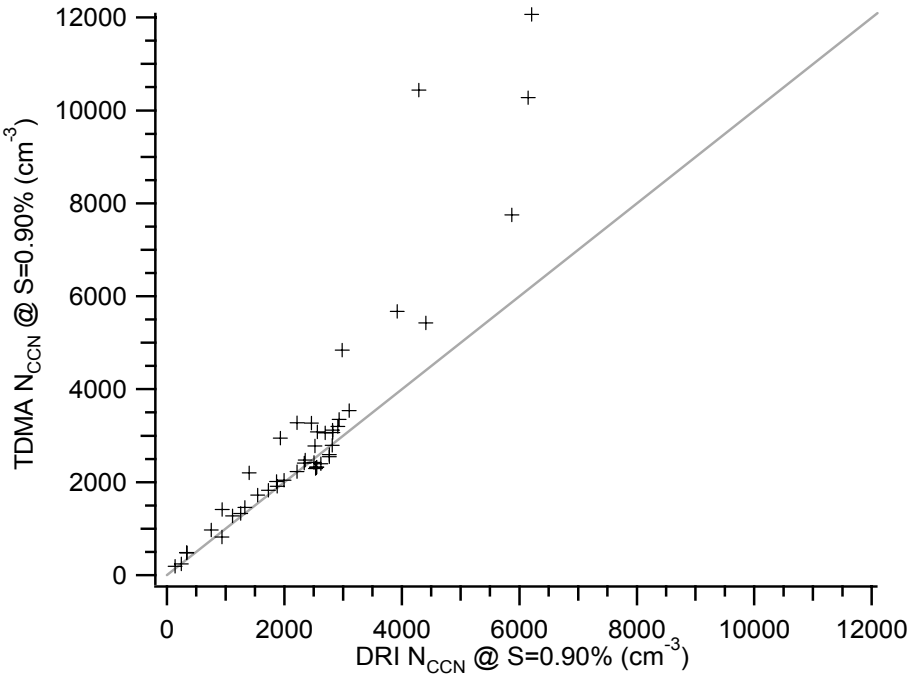

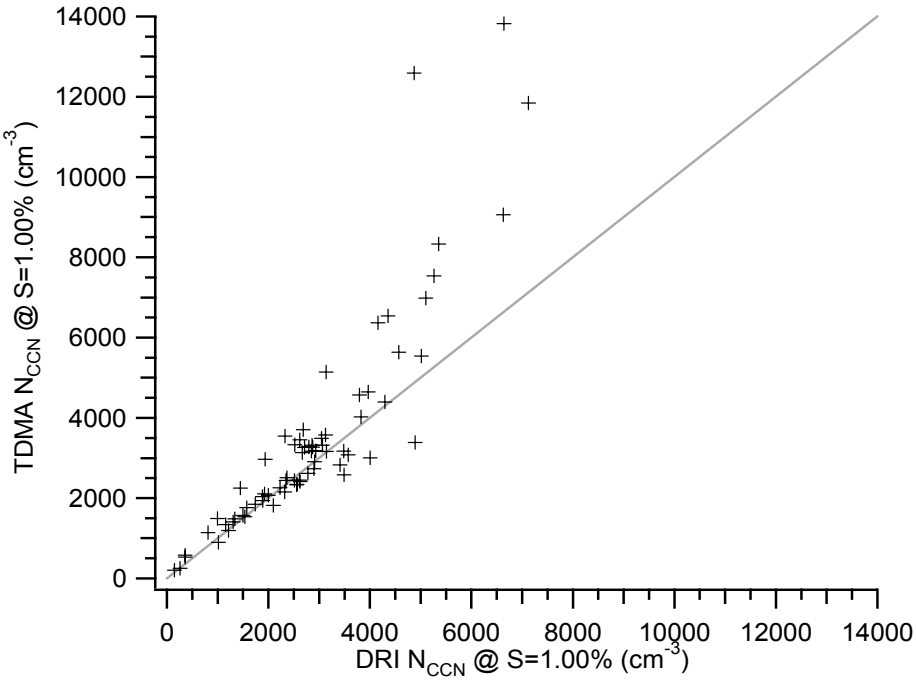

Figure 24 (continued).

Table 2. Number of DRI/TDMA measurement pairs at each supersaturation along with the corresponding R^2 values for the best-fit lines with the listed slopes and intercepts. Though data at 16 supersaturations are listed, the data from 3 additional supersaturations not shown in Figure 24 (0.09, 0.95, and 1.05%) are included in the totals and account for the 31-point discrepancy between the sum of the points listed and the total.

S(%)	Pairs	R^2	slope	intercept
0.02	118	0.44	2.31	-4.81
0.04	119	0.60	1.54	-25.52
0.06	120	0.72	0.93	-10.02
0.08	120	0.77	0.84	2.33
0.10	133	0.77	0.82	58.86
0.15	107	0.77	0.93	61.76
0.20	111	0.85	1.02	70.88
0.25	66	0.88	1.02	212.73
0.30	107	0.73	0.96	207.90
0.40	72	0.81	1.05	-62.93
0.50	62	0.72	1.00	44.80
0.60	73	0.78	1.14	-167.67
0.70	62	0.74	1.24	-321.65
0.80	73	0.78	1.37	-578.54
0.90	45	0.84	1.68	-988.33
1.00	71	0.78	1.57	-987.10
ALL	1490	0.86	1.20	-141.07

which were only observed at the highest supersaturations measured, predictions again exceed measured values. This overprediction is perhaps due to coincidence within the OPCs downstream of the DRI CCN spectrometers.

Aside from these overpredictions at very low and high supersaturations, agreement between predicted CCN concentrations and those measured is quite good. Figure 25 shows box plots of the ratio of predicted to measured CCN concentrations at each of the 19 supersaturations for which measured concentrations were reported. The horizontal dashed line denotes perfect agreement, and the shaded region highlights a range including $\pm$10%. Predicted CCN concentrations are generally close to those measured throughout the range of supersaturations considered, especially at supersaturations greater than 0.10%. The overpredictions at both ends of the spectrum described above are also apparent in Figure 25, and it is evident that they are more pronounced at lower supersaturations than at higher ones.

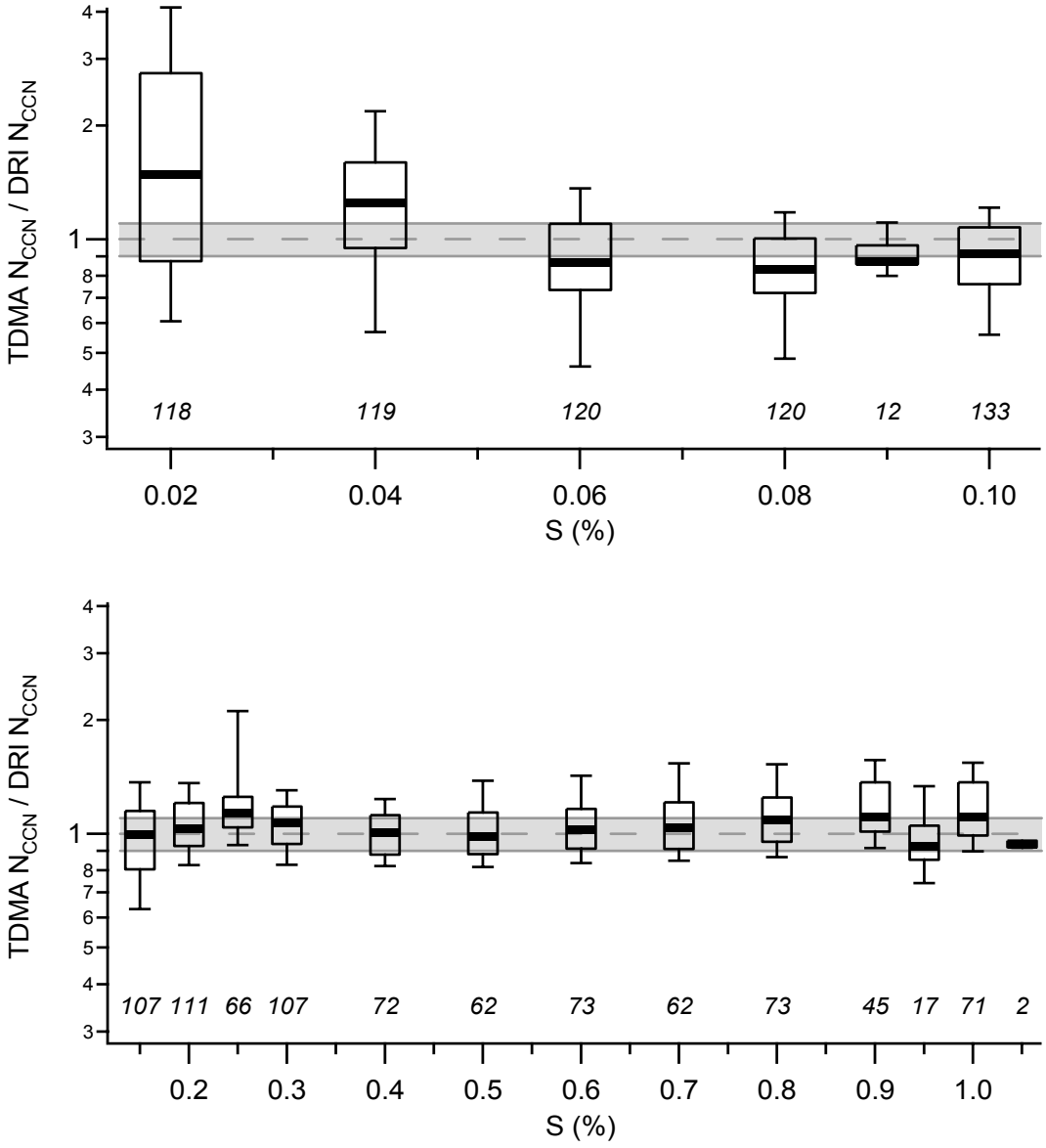

Figure 25. Box plots of the ratios of cumulative CCN concentrations (cm^{-3}) predicted using DMA/TDMA data versus those measured with the DRI CCN spectrometer as a function of the critical supersaturation measured within the DRI CCN spectrometer for the entire Aerosol IOP. The horizontal dashed line at 1.0 denotes perfect agreement, and the shaded region marks a range of $\pm$10%. The numbers in italics below each box indicate the number of DMA/TDMA-DRI CCN spectrometer measurement pairs included within each box plot.

6. SUMMARY*

Surface measurements of aerosol hygroscopicity and occasionally volatility were made with a DMA/TDMA at the ARM SGP Central Facility during the May 2003 Aerosol IOP. Although substantial variability in particle concentration and properties was observed during this month-long project, certain characteristics of the aerosol were repeatedly observed. Hygroscopicity usually increased with increasing particle size for particles smaller than 0.300 μm. This observation suggests that initial particle growth may be controlled by SOA, while subsequent growth was dominated by aqueous phase sulfate production. Aqueous and gas-phase production of sulfate is also believed to be the cause of the observed maximum in hygroscopicity during the morning and afternoon. The tail of a coarse dust mode is thought to be responsible for the frequent presence of non-hygroscopic 0.450- and 0.600-μm particles.

To segregate the sampled aerosol by direction of transport, a cluster analysis of backtrajectories terminating at the Central Facility of the ARM SGP site was coupled with the DMA/TDMA data. That cluster analysis yielded eight predominant backtrajectory profiles that were combined into four classifications: northwest, Midwest, southeast, and southwest. The hygroscopicity of the aerosol from the northwest and

---

Midwest generally increased with size, though larger particles from the Midwest were more hygroscopic than those from the northwest. This enhanced hygroscopicity in the large particles from the Midwest may be the result of exposure to urban or industrial plumes in which sulfate production rates were high. Aerosol from the southeast appeared to be heavily influenced by biomass burning in the Yucatan. Although influence from fires in Central America is not unusual, the magnitude of this event was. Therefore, the typical aerosol properties associated with that backtrajectory profile may differ substantially from those described here. The hygroscopic behavior of the aerosol during periods when transport was from the southwest was highly variable.

Coupling data from RH scan measurements with data from temperature scan measurements suggests that on May 20 most particles were composed of a mixture of ammonium sulfate and some insoluble and non-volatile compounds. Identical measurements made on May 27 suggest particles were composed of a more complex mixture of sulfate, insoluble and non-volatile compounds, and possibly a sparingly soluble organic that seemed to cause hygroscopicity to increase more rapidly at high RH than expected for a fixed solute content.

A new method for determining representative hygroscopic properties of aerosol size distribution modes was presented. The degree to which measured size-resolved hygroscopicity could be simulated by coupling parameterized size distributions with mode-resolved hygroscopicity was used to assess the compositional uniformity within size distribution modes. The calculated mode-resolved hygroscopicity was used to assess the relative importance of several processes that alter the size and properties of an

aerosol. During one of the periods considered, SOA dominated growth could be explained only through partitioning of subsaturated species into the aerosol. During both of the other periods examined, aqueous phase sulfate production was believed to be responsible for most of the observed increase in soluble volume concentration within the size distribution modes made up of particles that are expected to activate in cloud.

In addition, size distributions and hygroscopic growth factor distributions were combined to construct a simplistic model of the aerosol as a combination of organic carbon, elemental carbon, mineral dust, ammonium sulfate, and water, or a subset of these constituents. This multi-component model is used to compute humidity-dependent optical properties and to derive CCN spectra, which both provide independent methods of validating the proposed model.

Comparisons with direct measurements indicate that the total submicron scattering measured and its dependence on relative humidity are reasonably predicted with a Mie light scattering model using this multi-component aerosol, provided the aerosol is assumed to be in the metastable state. Enhanced scattering is observed at relative humidities below the crystallization RH of ammonium sulfate, suggesting that other particle constituents are either contributing to water uptake or depressing the crystallization RH of the entire particle. While overpredictions of f(RH) are limited to ~20% error, instances are observed in which both the scattering enhancement and the increase in scattering enhancement with increasing RH are underpredicted at relative humidities greater than ~65%. The agreement between derived CCN spectra and those measured with the DRI CCN spectrometers indicates that the activation properties of the

aerosol can be predicted based on this multi-component representation of the aerosol, though predicted CCN concentrations were slightly higher than the measurements at both the lowest and highest critical supersaturations measured.

REFERENCES

Albrecht, B. (1989), Aerosols, cloud microphysics and fractional cloudiness, *Science*, *245*(4923), 1227-1230.

Anderson, T. L., D. S. Covert, S. F. Marshall, M. L. Laucks, R. J. Charlson, A. P. Waggoner, J. A. Ogren, R. Caldow, R. L. Holm, F. R. Quant, G. J. Sem, A. Wiedensohler, N. A. Ahlquist, and T. S. Bates (1996), Performance characteristics of a high sensitivity, three wavelength, total scatter/backscatter nephelometer, *J. Atmos. Oceanic Technol.*, *13*(5), 967-986.

Anderson, T. L., and J. A. Ogren (1998), Determining aerosol radiative properties using the TSI 3563 integrating nephelometer, *Aerosol Sci. Technol.*, *29*(1), 57-69.

Bergin, M. H., S. E. Schwartz, R. N. Halthorne, J. A. Ogren, and D. L. Hlavka (2000), Comparison of aerosol optical depth inferred from surface measurements with that determined by Sun photometry for cloud-free conditions at a continental U.S. site, *J. Geophys. Res.*, *105*(D5), 6807-6816.

Bian, F., and F. M. Bowman (2005), A lumping model for composition- and temperature-dependent partitioning of secondary organic aerosols, *Atmos. Environ.*, *39*(7), 1263-1274.

Bigg, E. K. (1986), Discrepancy between observation and prediction of concentrations of cloud condensation nuclei, *Atmos. Res.*, *20*(1), 81-86.

Bohren, C. F., and D. R. Huffman (1983), *Absorption and Scattering of Light by Small Particles*, Wiley & Sons, New York.

Brooks, S. D., M. E. Wise, M. Cushing, and M. A. Tolbert (2002), Deliquescence behavior of organic/ammonium sulfate aerosol, *Geophys. Res. Lett.*, *29*(19), 1917, doi:10.1029/2002GL014733.

Cantrell, W., G. Shaw, G. R. Cass, Z. Chowdhury, L. S. Hughes, K. A. Prather, S. A. Guazzotti, and K. R. Coffee (2001), Closure between aerosol particles and cloud condensation nuclei at Kaashidhoo Climate Observatory, *J. Geophys. Res.*, *106*(D22), 28711-28718.

Carrico, C. M., M. J. Rood, and J. A. Ogren (1998), Aerosol light scattering properties at Cape Grim, Tasmania, during the first Aerosol Characterization Experiment (ACE 1), *J. Geophys. Res.*, *103*(D13), 16565-16574.

Charlson, R. J., S. E. Schwartz, J. M. Hales, R. D. Cess, J. A. Coakley, J. E. Hansen, and D. J. Hofmann (1992), Climate forcing by anthropogenic aerosols, *Science*, *255*(5043), 423-430.

Cocker, D. R., N. E. Whitlock, R. C. Flagan, and J. H. Seinfeld (2001), Hygroscopic properties of Pasadena, California aerosol, *Aerosol Sci. Technol.*, *35*(2), 637-647.

Collins, D. R., R. C. Flagan, and J. H. Seinfeld (2002), Improved inversion of scanning DMA data, *Aerosol Sci. Technol.*, *36*(1), 1-9.

Covert, D. S., J. L. Gras, A. Wiedensohler, and F. Stratmann (1998), Comparison of directly measured CCN with CCN modeled from the number-size distribution in the marine boundary layer during ACE 1 at Cape Grim, Tasmania, *J. Geophys. Res.*, *103*(D13), 16597-16608.

Dorling, S. R., T. D. Davies, and C. E. Pierce (1992), Cluster analysis: A technique for estimating the synoptic meteorological controls on air and precipitation chemistry – method and applications, *Atmos. Environ.*, *26*(14), *Ser. A.*, 2575-2581.

Draxler, R. R. (1988), Hybrid single-particle Lagrangian integrated trajectories (HYSPLIT): Model description, *ERL ARL-166*, Natl. Oceanic and Atmos. Admin., Washington, D. C.

Dusek, U., D. S. Covert, A. Wiedensohler, C. Neusüß, D. Weise, and W. Cantrell (2003), Cloud condensation nuclei spectra derived from size distributions and hygroscopic properties of the aerosol in coastal south-west Portugal during ACE-2, *Tellus*, *Ser. B, 55*(1), 35-53.

Feingold, G., W. L. Eberhard, D. E. Veron, and M. Previdi (2003), First measurements of the Twomey indirect effect using ground-based remote sensors, *Geophys. Res. Lett.*, *30*(6), 1287, doi:10/1029/2002GL016633.

Gasparini, R., R. Li, and D. R. Collins (2004), Integration of size distributions and size-resolved hygroscopicity measured during the Houston Supersite for compositional categorization of the aerosol, *Atmos. Environ.*, *38*(20), 3285-3303.

Gasparini, R., R. Li, D. R. Collins, R. A. Ferrare, and V. G. Brackett (2005), Application of aerosol hygroscopicity measured at the ARM Southern Great Plains site to examine composition and evolution, *J. Geophys. Res.*, in press.

Griffin, R. J., D. Dabdub, and J. H. Seinfeld (2005), Development and initial evaluation of a dynamic species-resolved model for gas phase chemistry and size-resolved gas/particle partitioning associated with secondary organic aerosol formation, *J. Geophys. Res.*, *110*, D05304, doi:10.1029/2004JD005219.

Hudson, J. G. (1989), An instantaneous CCN spectrometer, *J. Atmos. Oceanic Technol.*, *6*(6), 1055-1065.

Intergovernmental Panel on Climate Change (IPCC) (2001), *Climate Change 2001: The Scientific Basis*, edited by J.T. Houghton et al., Cambridge Univ. Press, New York.

Iziomon, M. G., and U. Lohmann (2003a), Optical and meteorological properties of smoke-dominated haze at the ARM Southern Great Plains Central Facility, *Geophys. Res. Lett.*, *30*(3), 1123, doi:10.1029/2002GL016606.

Iziomon, M. G., and U. Lohmann (2003b), Characteristics and direct radiative effect of mid-latitude continental aerosols: The ARM case, *Atmos. Chem. Phys.*, *3*, 1903-1917.

Johnson, G. R., Z. Ristovski, and L. Morawska (2004), Method for measuring the hygroscopic behaviour of lower volatility fractions in an internally mixed aerosol, *J. Aerosol Sci.*, *35*(4), 443-455.

Kalberer, M., D. Paulsen, M. Sax, M. Steinbacher, J. Dommen, A. S. H. Prevot, R. Fisseha, E. Weingartner, V. Frankevich, R. Zenobi, and U. Baltensperger (2004), Identification of polymers as major components of atmospheric organic aerosols, *Science*, *303*(5664), 1659-1662.

Kerker, M. (1969), *The Scattering of Light and Other Electromagnetic Radiation*, Academic Press, New York.

Kerminen, V.-M. (1997), The effects of particle chemical character and atmospheric processes on particle hygroscopic properties, *J. Aerosol Sci.*, *28*(1), 121-132.

Kus, P., C. M. Carrico, M. J. Rood, and A. Williams (2004), Measured and modeled light scattering values for dry and hydrated laboratory aerosols, *J. Atmos. Oceanic Technol.*, *21*(7), 981-994.

Lackey, M. (2004), *Hourly Surface Data: Unedited Local Climatological Data*, ncdc.info@noaa.gov, Natl. Climatic Data Cent., Asheville, NC.

Larson, S. M., G. R. Cass, K. J. Hussey, and F. Luce (1988), Verification of image-processing based visibility models, *Environ. Sci. Technol.*, *22*(6), 629-637.

Liu, P. S. K., W. R. Leaitch, C. M. Banic, S.-M. Li, D. Ngo, and W. J. Megaw (1996), Aerosol observations at Chebogue Point during the 1993 North Atlantic Regional Experiment: Relationships among cloud condensation nuclei, size distribution, and chemistry, *J. Geophys. Res.*, *101*(D22), 28971-28990.

Martin, G. M., D. W. Johnson, and A. Spice (1994), The measurement and parameterization of effective radius of droplets in warm stratocumulus clouds, *J. Atmos. Sci.*, *51*(13), 1823-1842.

McMurry, P. H., and M. R. Stolzenburg (1989), On the sensitivity of particle-size to relative humidity for Los Angeles aerosols, *Atmos. Environ.*, *23*(2), 497-507.

Mishchenko, M. I., L. D. Travis, R. A. Kahn, and R. A. West (1997), Modeling phase functions for dustlike tropospheric aerosols using a shape mixture of randomly oriented polydisperse spheroids, *J. Geophys. Res.*, *102*(D14), 16831-16847.

Nozière, B., and W. Esteve (2005), Organic reactions increasing the absorption index of atmospheric sulfuric acid aerosols, *Geophys. Res. Lett.*, *32*, L03812, doi:10.1029/2004GL021942.

Odum, J. R., T. Hoffmann, F. Bowman, D. R. Collins, R. C. Flagan, and J. H. Seinfeld (1996), Gas/particle partitioning and secondary organic aerosol yields, *Environ. Sci. Technol.*, *30*(8), 2580-2585.

Orr, C. Jr., F. K. Hurd, and W. J. Corbett (1958), Aerosol size and relative humidity, *J. Colloid Sci*., *13*(5), 472-482.

Orsini, D. A., A. Wiedensohler, F. Stratmann, and D. S. Covert (1999), A new volatility tandem differential mobility analyzer to measure the volatile sulfuric acid aerosol fraction, *J. Atmos. Oceanic Technol.*, *16*(6), 760-772.

Ouimette, J. R., and R. C. Flagan (1982), The extinction coefficient of multicomponent aerosols, *Atmos. Environ.*, *16*(10), 2405-2419.

Pant, A., A. Fok, M. T. Parsons, J. Mak, and A. K. Bertram (2004), Deliquescence and crystallization of ammonium sulfate-glutaric acid and sodium chloride-glutaric acid particles, *Geophys. Res. Lett.*, *31*, L12111, doi:10.1029/2004GL020025.

Parsons, M. T., D. A. Knopf, and A. K. Bertram (2004), Deliquescence and crystallization of ammonium sulfate particles internally mixed with water-soluble organic compounds, *J. Phys. Chem. A*, *108*(52), 11600-11608.

Philippin, S., A. Wiedensohler, and F. Stratmann (2004), Measurements of non-volatile fractions of pollution aerosols with an eight-tube volatility tandem differential mobility analyzer (VTDMA-8), *J. Aerosol Sci.*, *35*(2), 185-203.

Quinn, P. K., T. L. Anderson, T. S. Bates, R. Dlugi, J. Heintzenberg, W. von Hoyingen-Huene, M. Kulmala, P. B. Russell, and E. Swietlicki (1996), Closure in tropospheric research: A review and future needs, *Contr. Atmos. Phys./Beitr. Phys. Atmosph., 69*, 547-577.

Quinn, P. K., D. J. Coffman, T. S. Bates, E. J. Welton, D. S. Covert, T. L. Miller, J. E. Johnson, S. Maria, L. Russell, R. Arimoto, C. M. Carrico, M. J. Rood, and J. Anderson (2004), Aerosol optical properties measured on board the Ronald H. Brown during ACE-Asia as a function of aerosol chemical composition and source region, *J. Geophys. Res.*, *109*(D19), D19S01, doi:10.1029/2003JD004010.

Riemer, N., H. Vogel, and B. Vogel (2004), Soot aging time scales in polluted regions during day and night, *Atmos. Chem. Phys.*, *4*(7), 1885-1893.

Roberts, G. C., P. Artaxo, J. Zhou, E. Swietlicki, and M. O. Andreae (2002), Sensitivity of CCN spectra on chemical and physical properties of aerosol: A case study from the Amazon Basin, *J. Geophys. Res.*, *107*(D20), 8070, doi:10.1029/2001JD00583.

Saxena, P., L. M. Hildemann, P. H. McMurry, and J. H. Seinfeld (1995), Organics alter hygroscopic behavior of atmospheric particles, *J. Geophys. Res.*, *100*(D9), 18755-18770.

Seinfeld, J. H., and S. N. Pandis (1998), *Atmospheric Chemistry and Physics: From Air Pollution to Climate Change*, John Wiley & Sons, New York.

Sheridan, P. J., D. J. Delene, and J. A. Ogren (2001), Four years of continuous surface aerosol measurements from the Department of Energy's Atmospheric Radiation Measurement Program Southern Great Plains Cloud and Radiation Testbed site, *J. Geophys. Res.*, *106*(D18), 20735-20747.

Stolzenburg, M., N. Kreisberg, and S. Hering (1998), Atmospheric size distributions measured by differential mobility optical particle size spectrometry, *Aerosol Sci. Technol.*, *29*(5), 402-418.

Svenningsson, B., H.-C. Hansson, B. Martinsson, A. Wiedensohler, E. Swietlicki, S.-I. Cederfelt, M. Wendisch, K. N. Bower, T. W. Choularton, and R. N. Colvile (1997), Cloud droplet nucleation scavenging in relation to the size and hygroscopic behaviour of aerosol particles, *Atmos. Environ.*, *31*(16), 2463-2475.

Swietlicki, E., J. C. Zhou, O. H. Berg, B. G. Martinsson, G. Frank, S.-I. Cederfelt, U. Dusek, A. Berner, W. Birmili, A. Wiedensohler, B. Yuskiewicz, and K. N. Bower (1999), A closure study of sub-micrometer aerosol particle hygroscopic behaviour, *Atmos. Res.*, *50*(3-4), 205-240.

Tang, I. N. (1976), Phase transformation and growth of aerosol particles composed of mixed salts, *J. Aerosol Sci*., *7*(5), 361-371.

Tang, I. N. (1996), Chemical and size effects of hygroscopic aerosols on light scattering coefficients, *J. Geophys. Res.*, *101*(D14), 19245-19250.

Tang, I. N., and H. R. Munkelwitz (1977), Aerosol growth studies III – ammonium bisulfate aerosols in a moist atmosphere, *J. Aerosol Sci*., *8*(5), 321-330.

Tang, I. N., and H. R. Munkelwitz (1994), Water activities, densities, and refractive-indexes of aqueous sulfates and sodium-nitrate droplets of atmospheric importance, *J. Geophys. Res.*, *99*(D9), 18801-18808.

Turner, D. D., R. A. Ferrare, and L.H. Brasseur (2001), Average aerosol extinction and water vapor profiles over the Southern Great Plains, *Geophys. Res. Lett.*, *28*(23), 4441-4444.

Turner, D. D., R. A. Ferrare, L. A. Heilman, W. F. Feltz, and T. Tooman (2002), Automated retrievals of aerosol extinction and backscatter coefficient profiles from a Raman lidar, *J. Atmos. Oceanic Technol.*, *19*(1), 37-50.

Twomey, S. (1977), Influence of pollution on the short-wave albedo of clouds, *J. Atmos. Sci.*, *34*(7), 1149-1152.

VanReken, T. M., T. A. Rissman, G. C. Roberts, V. Varutbangkul, H. H. Jonsson, R. C. Flagan, and J. H. Seinfeld (2003), Toward aerosol/cloud condensation nuclei (CCN) closure during CRYSTAL-FACE, *J. Geophys. Res.*, *108*(D20), 4633, doi:10.1029/2003JD003582.

Wang, S. C., and R. C. Flagan (1990), Scanning electrical mobility spectrometer, *Aerosol Sci. Technol*., *13*(2), 230-240.

Weber, R. J., D. Orsini, Y. Daun, Y.-N. Lee, P. J. Klotz, and F. Brechtel (2001), A particle-into-liquid collector for rapid measurement of aerosol bulk chemical composition, *Aerosol Sci. Technol*., *35*(3), 718-727.

Zhang, X. Q., P. H. McMurry, S. V. Hering, and G. S. Casuccio (1993), Mixing characteristics and water content of submicron aerosols measured in Los Angeles and at the Grand Canyon, *Atmos. Environ. Ser. A*, *27*(10), 1593-1607.

VITA

Roberto Gasparini was born in Houston, Texas, on 25 September 1978. He attended Our Lady of Mount Carmel Elementary School from grades K-8. His passion for science led him to Saint Thomas High School, where he was the valedictorian of the Class of 1996. As a proud member of the Fightin' Texas Aggie Class of 2000, Roberto earned his B.S. in Meteorology in December 1999. He remained at Texas A&M for graduate school, serving as a teaching assistant for one year prior to joining the Aerosol Research Group. From 2000-2001, he participated in the TexAQS 2000/EPA Supersite campaigns in Houston, Texas, and the analysis of the data collected in Houston formed the basis of his initial graduate research. After receiving his M.S. in Atmospheric Sciences in August 2002, Roberto published these results, which appeared in *Atmospheric Environment* in 2004. Wishing to go further, he participated in a project in Oklahoma in May 2003, and the data collected there are used in this dissertation as well as one publication already accepted by *Journal of Geophysical Research-Atmospheres*. A second submission to this journal regarding these data is forthcoming. In addition to these first-author publications, he has been included as a co-author on four other publications, three of which were primarily written by colleagues outside of Texas A&M. He received his Ph.D. in May 2005. Though he was still seeking employment as of this submission, he can be reached through his parents' address:

2908 Cedar Ridge Trail

Friendswood, TX 77546